Check for updates

Photocatalytic and Electrocatalytic Generation of Hydrogen Peroxide: Principles, Catalyst Design and Performance

Yan Guo[1,2], Xili Tong[1] ✉, Nianjun Yang[3,4,5] ✉

HIGHLIGHTS

- Basic principles of photo- and electro-catalytic hydrogen peroxide generation.

- Recent progresses on the design, performance and mechanisms of photo- and electro-catalysts for hydrogen peroxide generation.

- Scientific challenges and prospects of engineering photo- and electro-catalysts for hydrogen peroxide production.

ABSTRACT Hydrogen peroxide (H_2O_2) is a high-demand organic chemical reagent and has been widely used in various modern industrial applications. Currently, the prominent method for the preparation of H_2O_2 is the anthraquinone oxidation. Unfortunately, it is not conducive to economic and sustainable development since it is a complex process and involves unfriendly environment and potential hazards. In this context, numerous approaches have been developed to synthesize H_2O_2. Among them, photo/electro-catalytic ones are considered as two of the most promising manners for on-site synthesis of H_2O_2. These alternatives are sustainable in that only water or O_2 is required. Namely, water oxidation (WOR) or oxygen reduction (ORR) reactions can be further coupled with clean and sustainable energy. For photo/electro-catalytic reactions for H_2O_2 generation, the design of the catalysts is extremely important and has been extensively conducted with an aim to obtain ultimate catalytic performance. This article overviews the basic principles of WOR and ORR, followed by the summary of recent progresses and achievements on the design and performance of various photo/electro-catalysts for H_2O_2 generation. The related mechanisms for these approaches are highlighted from theoretical and experimental aspects. Scientific challenges and opportunities of engineering photo/electro-catalysts for H_2O_2 generation are also outlined and discussed.

KEYWORDS H_2O_2 generation; Photocatalysts; Electrocatalysts; Reaction mechanisms
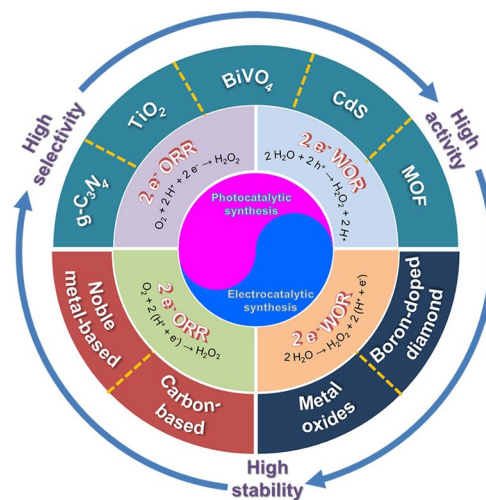
✉ Xili Tong, tongxili@sxicc.ac.cn; Nianjun Yang, nianjun.yang@uni-siegen.de; nianjun.yang@uhasselt.be

1 State Key Laboratory of Coal Conversion, Institute of Coal Chemistry, Chinese Academy of Sciences, Taiyuan 030001, People's Republic of China
2 University of Chinese Academy of Sciences, Beijing 100049, People's Republic of China
3 Institute of Materials Engineering, University of Siegen, 57076 Siegen, Germany
4 Department of Chemistry, Hasselt University, 3590 Diepenbeek, Belgium
5 IMO-IMOMEC, Hasselt University, 3590 Diepenbeek, Belgium

1 Introduction

Hydrogen peroxide (H_2O_2) is a strong oxidant reagent compared with Cl-containing oxidants such as HOCl. This efficient and environmental-friendly chemical has been selected as one of the 100 most important chemical substances in the world [1, 2]. Owing to its strong oxidation capability, H_2O_2 has been widely used in a wide range of industrial and household applications, including wastewater treatment, chemical synthesis, industrial bleaching, energy storage, medical disinfection and a promising energy carrier in fuel cells [3–7]. It has been pointed out that H_2O_2 has advantages of the highest concentration of active oxygen (47.1 wt%) and the cleanest by-product (H_2O) without carbon emission. These features make H_2O_2 a promising fuel alternative to H_2 and O_2 for one-chamber fuel cells without a membrane [8–10]. Although H_2O_2 fuel cells produce a bit lower theoretical output voltage (1.09 V) than H_2/O_2 fuel cells (1.23 V), the energy density of H_2O_2 (2.1 MJ kg^{-1} for 60% aqueous H_2O_2) is comparable to that of compressed hydrogen (3.5 MJ kg^{-1}) [11–15]. In addition, H_2O_2 is a liquid fuel that can be fully soluble in water. It is thus more

secure and facilitated to be transported and stored than the conventional H_2. Accordingly, H_2O_2 has been predicted to be produced on a scale of approximately 5.7 million tons by 2027 in the global market, emphasizing its growing influence in the fields of sustainable energy [16].

The widely used method to synthesize H_2O_2 in the industry is anthraquinone (AQ) oxidation, which accounts for more than 95% of the total production of H_2O_2 [17]. Generally, the AQ oxidation process is a four-step cycle: (i) hydrogenation of AQ using a catalyst, (ii) oxidation of hydrogenated AQ to regenerate AQ and produce H_2O_2, (iii) extraction of H_2O_2 and (iv) purification concentration of H_2O_2. Therefore, this process requires a high energy demandingness and resource consumption and meanwhile produces many harmful by-products in series reactions (Fig. 1a) [18]. In this context, the pursuit of high concentration of H_2O_2 via AQ oxidation technology brings in more environmental pollutants and explosive substances, being threatened to the safety in fuel storage and transportation [19, 20]. To avoid these shortcomings of the AQ process, the direct preparation of H_2O_2 through the reaction from H_2 and O_2 appears more popular. It has been considered as a more energy-efficient
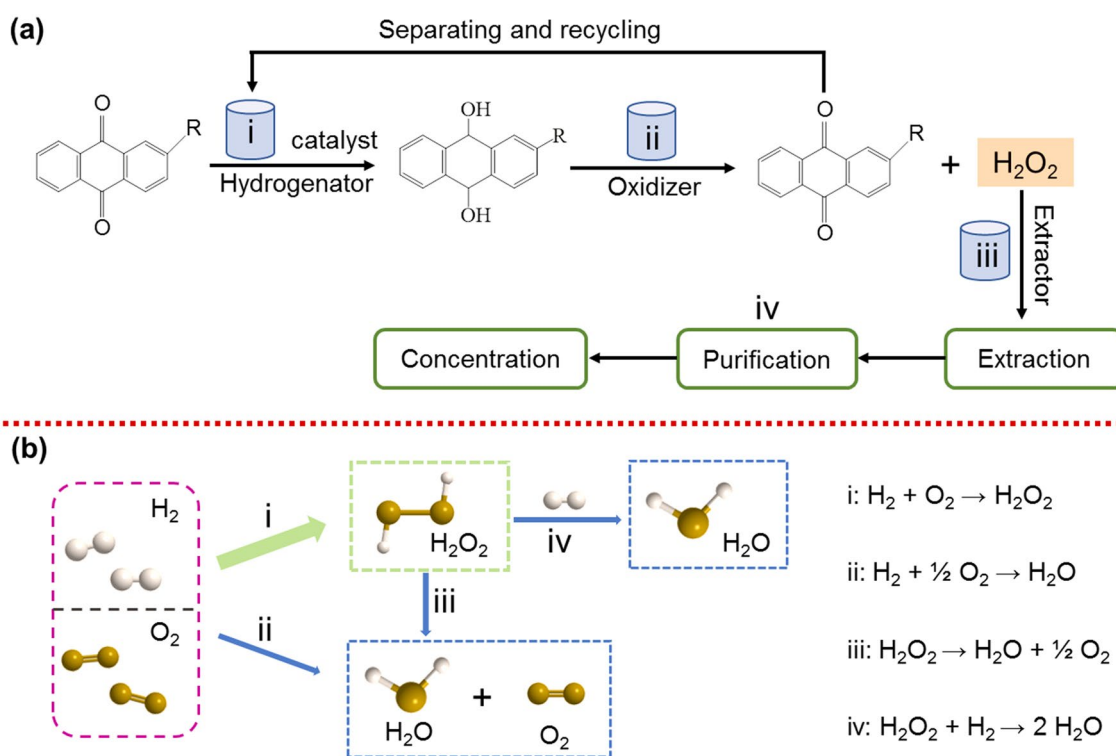

Fig. 1 Schematic illustration of **a** the anthraquinone (AQ) oxidation process and **b** the direct synthesis from H_2 and O_2

and resource-efficient route alternative to the AQ oxidation (Fig. 1b) [21–24]. This partial hydrogenation reaction can be fully performed at low temperatures, if the highly efficient catalysts are designed and applied. It needs to be pointed out that this process usually selects expensive Pd-based materials as catalysts to limit competing side reactions [25, 26]. More seriously, it requires precise control of the ratio of H_2 and O_2 to leave for the explosive range, which unavoidably leads to low practice yields of the direct synthesis [27–29]. Another potential route to synthesize H_2O_2 is through a range of enzymatic catalytic processes in nature. It has been reported that some oxidase enzymes (e.g., glucose oxidase, D-amino acid oxidase and cholesterol oxidase) can selectively catalyze the corresponding native substrates to generate H_2O_2 [30–33]. Unfortunately, the inferior activity with a low value of turnover frequency occurs in these enzymatic catalytic reactions, which has impeded the rapid development of such biosynthesis of H_2O_2 [34, 35]. Consequently, environmental-friendly, efficient, safe and convenient alternative routes still need to be explored for H_2O_2 production.

In recent years, photo/electro-catalytic synthesis of H_2O_2 has attracted extensive attention. Comparison with the aforementioned three routes, these new approaches are more economical and environmental-friendly [36–39]. Belonging to direct synthesis methods, they can be realized using the abundant H_2O and O_2 on the earth as reactants, but are easier to be handled with lower operating risks [40, 41]. In addition, they can take full advantages of clean and renewable energy sources (e.g., solar energy, wind energy) in a sustainable fashion. To obtain efficient photo/electro-catalytic conversion efficiency, high-performance catalyst platforms need to be established. In other words, the design of advanced photo/electro-catalysts plays a vital role in such reaction conversion [42, 43]. From both fundamental and practical viewpoints, the rational design and controllable synthesis of various photo/electro-catalysts are thus of great importance for H_2O_2 synthesis.

In this regard, many efforts have been made in the design and synthesis of effective photo/electro-catalysts for active and selective generation of H_2O_2. It is therefore extremely significant to summarize the progress and state-of-art about design, characterization and application of developed photo/electro-catalysts for active and selective production of H_2O_2. This review article provides a comprehensive account of the development of photo/electro-catalysts toward H_2O_2 generation, covering related synthesis mechanisms, state-of-the-art

catalysts/materials together with their performance evaluation criterion and typical engineering strategies for H_2O_2 formation. The future perspectives of photo/electro-catalyst design for H_2O_2 production are discussed and outlined.

2 Mechanisms of Catalytic H_2O_2 Synthesis

2.1 Photocatalytic Mechanisms of H_2O_2 Synthesis

The best advantage of photocatalytic synthesis is the direct utilization of renewable and sustainable solar energy to synthesize various products or degrade series of pollutes [44–46]. Most of recent photocatalytic synthesis studies focus on photocatalytic reactions on the semiconductors. During a typical photocatalytic process of H_2O_2 synthesis, three consecutive fundamental steps undergo on the photocatalysts [47]. In the first step, a semiconductor photocatalyst absorbs the excitation light, of which energy is greater than the band gap of the used photocatalyst, to create the negatively charged electron (e^-) on its conduction band (CB), accompanying positively charged hole (h^+) on its valence band (VB). In the second step, these photoinduced charge carriers (namely both e^- and h^+) in the interior are separated and diffuse into the surface of the photocatalyst. Finally, they react with H_2O and O_2 to generate H_2O_2 via different redox pathways. Some recombine with each other and do not participate in any chemical reactions.

In the second step of a photocatalytic process of H_2O_2 synthesis, either oxygen reduction reaction (ORR) or water oxidation reaction (WOR) is involved [15]. As for the process of ORR (Fig. 2a), there are two potential mechanisms: indirect two-step single-electron ($O_2 \rightarrow \cdot O_2^- \rightarrow H_2O_2$) and direct one-step two-electron ($O_2 \rightarrow H_2O_2$) pathways. For example, the photons are absorbed by the semiconductor photocatalyst to excite the electrons in its VB to its CB, while holes are remained in its VB at the first step. Subsequently, the holes (h^+) oxidize H_2O to produce O_2 (Eq. 1). In the indirect two-step single-electron pathway, one formed O_2 molecule reacts with one electron (e^-) to form $O_2^{\cdot-}$ in the CB of the photocatalyst (Eq. 2a), which spontaneously combines H^+ to generate a $HO_2^{\cdot-}$ intermediate (Eq. 2b). This radical can also get one electron to produce HO_2^- intermediate via another one-electron reduction reaction pathway (Eq. 2c). Finally, the synthesized HO_2^- species reacts with H^+, leading to H_2O_2 evolution in the form of Eq. 2d. In the
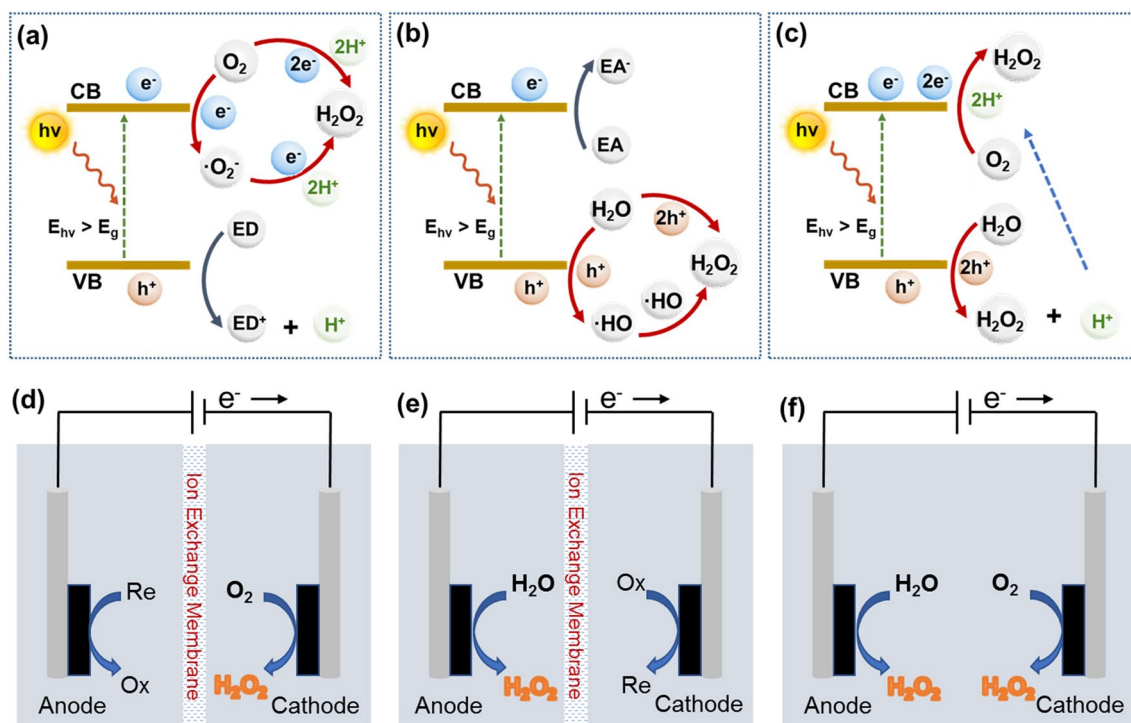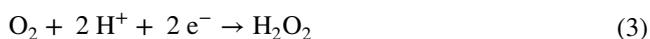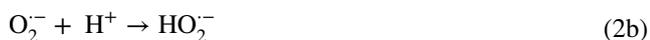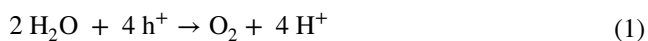
Fig. 2 Simplified schematic of photocatalytic H_2O_2 generation from **a** ORR, **b** WOR and **c** dual-channel pathway. Simplified schematic of electrocatalytic H_2O_2 production from **d** ORR, **e** WOR and **f** dual-channel pathway

direct one-step two-electron pathway, one formed O_2 molecule directly reacts with two electrons (e^-), resulting in the formation of H_2O_2, as demonstrated in Eq. 3.

$$2\,H_2O\,+\,4\,h^+ \rightarrow O_2\,+\,4\,H^+ \tag{1}$$

$$O_2 + e^- \rightarrow O_2^{\cdot-} \tag{2a}$$

$$O_2^{\cdot-} + H^+ \rightarrow HO_2^{\cdot} \tag{2b}$$

$$HO_2^{\cdot} + e^- \rightarrow HO_2^- \tag{2c}$$

$$HO_2^- + H^+ \rightarrow H_2O_2 \tag{2d}$$

$$O_2 + 2\,H^+ + 2\,e^- \rightarrow H_2O_2 \tag{3}$$

The mechanism of H_2O_2 synthesis via the WOR (Fig. 2b) can be divided two pathways: direct one-step ($H_2O \rightarrow H_2O_2$) and indirect two-step ($H_2O \rightarrow {}^{\cdot}OH \rightarrow H_2O_2$) approaches. In the case of direct one-step process, one H_2O molecule is directly oxidized by two holes to generate one H_2O_2 through the one-step reaction (Eq. 4). Regarding indirect two-step WOR, H_2O is firstly be oxidized and the $^{\cdot}OH$ intermediate is

formed (Eq. 5a). These intermediates react with each other to produce H_2O_2 (Eq. 5b).

$$2\,H_2O\,+\,2\,h^+ \rightarrow H_2O_2 +\,2\,H^+ \tag{4}$$

$$H_2O\,+\,h^+ \rightarrow {}^{\cdot}OH\,+\,H^+ \tag{5a}$$

$$2\,{}^{\cdot}OH \rightarrow H_2O_2 \tag{5b}$$

It is acknowledged that the process of photocatalytic H_2O_2 synthesis might simultaneously occur through both the ORR and WOR mechanisms (Fig. 2c). However, these strategies have the unavoidable drawbacks [48, 49]. Firstly, the solubility of O_2 in liquid phase is low, limiting related reaction rates. Secondly, the recombination of electrons and holes is fast, reducing dramatically the efficiency of electron utilization. Thirdly, thermodynamic feasibility of the $4e^-$ pathway is greater than of the $2e^-$ pathway, leading to low selectivity of such processes. Therefore, it is necessary to design advanced photocatalysts to overcome these shortcomings.

The apparent quantum yield (AQY), defined as the ratio of the electron number in generating H_2O_2 molecule and the incident photons at a given wavelength, is an important

indicator to evaluate the photocatalytic efficiency of various photocatalysts. It is frequently calculated using Eq. 6 [20].

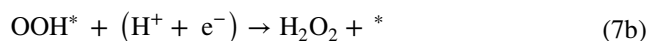$$AQY(\%) = \frac{2n}{N_{aph}} \times 100\% \tag{6}$$

where n is the electron amount of produced H_2O_2, N_{aph} is the number of incident photons shined on the photocatalysts.

In the section of discussion of photocatalysts (Chapter 3), we summarize recent progress and achievements on representative photocatalysts for H_2O_2 synthesis, in terms of their morphology and electronic band structures as well as their corresponding visible light-driven performance (e.g., activity, selectivity and stability) for H_2O_2 production.
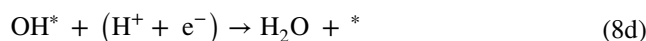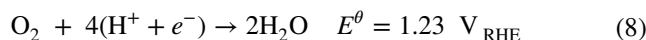
2.2 Electrocatalytic Mechanisms of H_2O_2 Synthesis

Electrocatalytic synthesis of H_2O_2 via the oxygen electrochemistry has been widely considered as an attractive route for on-site production of H_2O_2. Such an approach has effectively addressed the disadvantages of the AQ process and the possibility to be coupled with sustainable energy sources [50, 51]. Note that there are two direct pathways to produce H_2O_2, including two-electron oxygen reduction reaction (2e⁻ ORR, Fig. 2d) and two-electron water oxidation reaction (2e⁻ WOR, Fig. 2e) [52–54]. As for the 2e⁻ ORR process, the reduction of O_2 to H_2O_2 proceeds by a two-step consecutive reaction road. This process can be described as an overall electrochemical reaction (Eq. 7), where E^θ represents the standard thermodynamic equilibrium potential, which is calculated to 0.70 V versus reversible hydrogen electrode (RHE). In more detail, one O_2 molecule diffuses to the active surface of an electrocatalyst and gets adsorbed. If it gains one electron from the electrode and further reacts with one H^+ ion, the OOH* intermediate is generated (Eq. 7a, noted that * represents an unoccupied active site). Since the formed OOH* possesses high chemical reaction activity, it can combine with another H^+ ion and one electron to produce H_2O_2, accompanying with regeneration of the active site (Eq. 7b). Unfortunately, the OOH* intermediate can undergo a four-electron pathway to decompose and form *O and *OH intermediates, which forms H_2O instead of H_2O_2 [55]. The overall electrochemical reaction for the 4e⁻ ORR process is depicted as Eq. 8, where E^θ is 1.23 V_{RHE}. In the reaction mechanism, the as-formed OOH* intermediate in the first step (Eq. 8a) reacts

with one H^+ ion and electron to form O^* (Eq. 8b), which is further combined with another H^+ ion and electron. The formation of OH* intermediate (Eq. 8c) in this step leads to the undesirable 4e⁻ ORR, which forms H_2O, an alternative to H_2O_2 (Eq. 8d). Therefore, the OOH* intermediate plays a vital role in determining the 2e⁻ or 4e⁻ ORR pathways. For example, retaining the O–O bond in OOH*, meaning weaker oxygen binding energy, is favorable to improve the selectivity of H_2O_2 production [54, 55]. On the contrary, the stronger oxygen binding energy facilitates the 4e⁻ ORR pathway, resulting in the electrocatalytic synthesis of H_2O. The 2e⁻ ORR:

$$O_2 + 2(H^+ + e^-) \rightarrow H_2O_2 \quad E^\theta = 0.7 \text{ V}_{RHE} \tag{7}$$

$$* + O_2 + (H^+ + e^-) \rightarrow OOH^* \tag{7a}$$

$$OOH^* + (H^+ + e^-) \rightarrow H_2O_2 + * \tag{7b}$$

The 4e⁻ ORR:

$$O_2 + 4(H^+ + e^-) \rightarrow 2H_2O \quad E^\theta = 1.23 \text{ V}_{RHE} \tag{8}$$

$$* + O_2 + (H^+ + e^-) \rightarrow OOH^* \tag{8a}$$

$$OOH^* + (H^+ + e^-) \rightarrow H_2O + O^* \tag{8b}$$

$$O^* + (H^+ + e^-) \rightarrow OH^* \tag{8c}$$

$$OH^* + (H^+ + e^-) \rightarrow H_2O + * \tag{8d}$$

Similar as photocatalytic process of H_2O_2 synthesis, both ORR and WOR might simultaneously occur in electrocatalytic process (Fig. 2f).

To evaluate the catalytic selectivity in the electrocatalytic H_2O_2 synthesis via the ORR approach, the number of electrons transferred (n) needs to be calculated by use of the rotating ring-disk electrode (RRDE) or rotating disk electrode (RDE) technique. For the RRDE measurements, linear sweep voltammetry (LSV) is generally performed on the disk electrode, while a constant potential (e.g., 1.2 V_{RHE}) is applied on the ring electrode. When H_2O_2 is produced on the disk, it can diffuse to the ring then be detected. Equation 9 has been often employed to calculate the n value, where I_D is the current on the disk electrode, I_R is the current at the ring electrode, and N is the efficiency of H_2O_2

collection. The N value can be obtained using Eq. 10. For the RDE measurements, the Koutecky–Levich (K–L) equation is applied to calculate n (Eq. 11), where I is the measured steady-state current derived from the ORR (mA cm^{-2}), I_K is the kinetic current of the reaction with active substances on the electrode surface, F is the Faraday constant (96,500 C mol^{-1}), A is the geometric area of the work electrode, D_0 is the diffusion coefficient of O_2 in the electrolyte (cm^2 s^{-1}), ω is the angular rotation speed ($\omega = 2\pi N$, N is the linear rotation speed), ν is the kinematic viscosity of the electrolyte (cm^2 s^{-1}), C_{O_2} is the saturated concentration of O_2 in the solution (mol cm^{-3}).

$$n = 4\,\frac{I_D}{I_D + I_R/N} \tag{9}$$
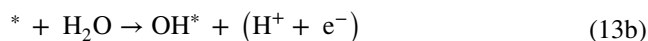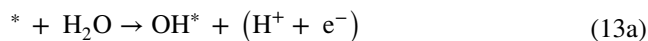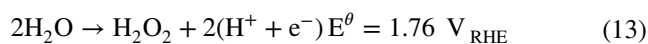
$$N = -\frac{I_R}{I_D} \tag{10}$$

$$\frac{1}{I} = \frac{1}{I_K} + \frac{1}{0.620 n F A D_0^{2/3} \omega^{1/2} \nu^{-1/6} C_{O_2}} \tag{11}$$

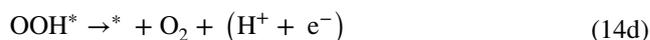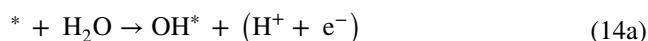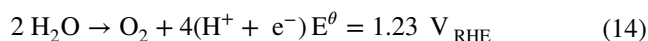Using as-obtained n value, the selectivity of H_2O_2 production can be calculated according to Eq. 12.

$$H_2O_2\,(\%) = \frac{4-n}{2} \tag{12}$$

Another promising route for electrocatalytic synthesis of H_2O_2 is the 2e$^-$ WOR pathway, which can be depicted in an overall electrochemical reaction (Eq. 13) with E^θ of 1.76 V_{RHE}. In this process, one H_2O molecule is firstly electrooxidized by active sites on the electrode to form OH*, providing one electron and H$^+$ ion (Eq. 13a). Another H_2O molecule goes through the same reaction (Eq. 13b). Two OH* then combine with each other, leading to the production of H_2O_2 (Eq. 13c). Similar with the case in ORR, the 2e$^-$ WOR pathway faces the influence from the 4e$^-$ WOR pathway (Eq. 14), where the thermodynamically equilibrium potential (1.2 V_{RHE}) is lower than that in the 2e$^-$ WOR pathway [41, 56]. In more detail, the OH* radicals generated in the first step (Eq. 14a) are further electrooxidized, resulting in the formation of O* intermediate (Eq. 14b). These O* intermediates then lose one electron to form OOH* intermediate (Eq. 14c). Finally, the OOH* intermediate converts into O_2 molecular to complete this 4e$^-$ WOR process (Eq. 14d).

The 2e$^-$ WOR:

$$2H_2O \rightarrow H_2O_2 + 2(H^+ + e^-)\,E^\theta = 1.76\ V_{RHE} \tag{13}$$

$$* + H_2O \rightarrow OH^* + (H^+ + e^-) \tag{13a}$$

$$* + H_2O \rightarrow OH^* + (H^+ + e^-) \tag{13b}$$

$$OH^* + OH^* \rightarrow H_2O_2 \tag{13c}$$

The 4e$^-$ WOR:

$$2\,H_2O \rightarrow O_2 + 4(H^+ + e^-)\,E^\theta = 1.23\ V_{RHE} \tag{14}$$

$$* + H_2O \rightarrow OH^* + (H^+ + e^-) \tag{14a}$$

$$OH^* \rightarrow O^* + (H^+ + e^-) \tag{14b}$$

$$O^* \rightarrow OOH^* + (H^+ + e^-) \tag{14c}$$

$$OOH^* \rightarrow * + O_2 + (H^+ + e^-) \tag{14d}$$

The key factor to dominate the H_2O_2 synthesis via the 2e$^-$ WOR pathway is thus the appropriate interaction between the catalytic surface and O intermediates (e.g., *O, *OH and *OOH) [57]. Specifically, too strong OH binding promotively oxidizes *OH to *O, further to *OOH, thereby prompting the undesirable 4e$^-$ pathway to generate O_2. On the other hand, too weak binding improves the selectivity of 2e$^-$ WOR, but inevitably causes high kinetic barriers to hydrolysis and significantly slows down the reaction rate. It is disappointed that H_2O_2 produced in the 2e$^-$ WOR process is not chemically stable. The undesirable disproportionation (2 $H_2O_2 \rightarrow 2\ H_2O + O_2$) or homolysis ($H_2O_2 \rightarrow 2\ \cdot OH$) spontaneously arises, decreasing the selectivity of H_2O_2 production. Therefore, the electrocatalysts with proper binding energies are highly pursued to boost 2e$^-$ pathway toward H_2O_2 production.

In general, the selectivity of H_2O_2 generation via H_2O electrooxidation is defined using the term of Faradaic Efficiency (%FE) (Eq. 15).

$$\%FE = \frac{Q_{H_2O_2}}{Q_{total}} \tag{15}$$

where $Q_{H_2O_2}$ is the charge that is used to produce H_2O_2, and Q_{total} is the total charge passed during the whole process for water electrooxidation. In the section of the discussion of electrocatalysts (Chapter 4), we will summarize and evaluate research progress on representative electrocatalysts for

synthesizing H_2O_2, in terms of the morphology, structure, composition as well as the corresponding activity, selectivity and stability.

It should be pointed out that the detection of the H_2O_2 concentration in the electrolyte is very important for the practical applications. Such a concentration is generally determined by the following methods, including [58]: (1) titration using potassium permanganate ($KMnO_4$) or cerium sulfate [$Ce(SO_4)_2$], (2) colorimetric change from Fe^{2+} to Fe^{3+}, (3) colorimetric determination using titanium (IV) sulfate and (4) high-performance liquid chromatography (HPLC). To separate the generated H_2O_2 from the electrolyte, the oil–water two-phase systems or distillation can be applied, although few reports have focused on such an issue.

3 Photocatalytic H_2O_2 Synthesis

3.1 Graphitic Carbon Nitride

Graphitic carbon nitride (g-C_3N_4) possesses a graphitic stacking of structure aromatic molecules with an alternating arrangement of earth-abundant carbon and nitrogen elements. Since the pioneering work of g-C_3N_4 for the promotion of photocatalytic hydrogen evolution under visible light irradiation, g-C_3N_4 has received strongly attention [59]. Such a situation is derived from this metal-free polymer photocatalyst features intrinsic advantages, such as its suitable band gap (~ 2.7 eV) for visible light response, facile preparation, relatively higher conductivity, excellent chemical stability in strong acidic and alkali media and special electronic structure [60–64]. In this context, it has been frequently employed for various photocatalytic applications, such as CO_2 reduction, H_2 production, and especially for H_2O_2 production [65–70]. Especially, since the CB potential (−1.3 V) of g-C_3N_4 is more negative than the reduction potential of O_2/H_2O_2 (0.695 V), g-C_3N_4 is thermodynamically promising to reduce O_2 for the H_2O_2 production using visible light [71]. In addition, the VB potential of g-C_3N_4 (1.4 V) is lower enough to effectively prevent the oxidative decomposition of H_2O_2 [64]. For example, Shiraishi's group employed g-C_3N_4 for photocatalytic H_2O_2 production with the selectivity higher than 90%. The generated intermediate generated on the g-C_3N_4 surface 1,4-endoperoxide promotes the two-electron ORR pathway to produce H_2O_2 [68]. However, it must stress that the pristine g-C_3N_4 has many

drawbacks that limit its photocatalytic performance toward the H_2O_2 production, covering its small specific surface area, weak ability to capture visible light and low chemical adsorption capacity of O_2 on its surface [72, 73]. To overcome these shortcomings, ultra-thin g-C_3N_4 nanoplates and hexagonal rosettes of g-C_3N_4 have been prepared, which showed remarkable photocatalytic activity in the H_2O_2 production, stemming from their high surface area, rich active sites and strong light-harvesting capability [74, 75]. Unfortunately, the overall photo-conversion efficiencies of these g-C_3N_4 nano-photocatalysts are still unsatisfactory, due to rapid recombination of photogenerated carriers. Therefore, it is necessary to introduce organic scavengers into these nano-photocatalysts (e.g., ultra-thin g-C_3N_4 nanoplates and hexagonal rosettes of g-C_3N_4) to consume holes in the process of H_2O_2 production [70, 76]. In short, the efficiency for visible-light excitation, the separation of photogenerated carriers and photo-reaction kinetics of g-C_3N_4 photocatalysts must be further improved. In this regard, surface engineer of g-C_3N_4 photocatalysts has been proposed and developed to facilitate its performance with the enhanced the photocatalytic production efficiency of H_2O_2 on g-C_3N_4 photocatalysts. To optimize the photocatalytic H_2O_2 synthesis, the reported strategies cover manufacturing of surface defects, loading precious metal nanoparticles, constructing heterojunction composites, polyoxometalate hybridization and metal/non-metal element doping are performed (Table 1). In the following sessions, the details of these strategies are explained.

3.1.1 Manufacturing Surface Defects

Vacancy defects are known to have the ability to capture photogenerated electrons/holes, thereby effective inhibiting the recombination of photogenerated electrons and holes [77–80]. Meanwhile, they can enhance the adsorption and activation of gas molecules (e.g., O_2), due to their abundant local electrons for the adjustment of the electronic structure, thus facilitating a photocatalytic process [81, 82]. In general, two main types of defects appear in (or on) the g-C_3N_4 photocatalysts: carbon and nitrogen vacancies.

Carbon vacancies The defects derived from carbon element in/on g-C_3N_4 photocatalysts bring in carbon vacancies. They stand at mid-gap states between VB and CB and thus

Table 1 Summary of the g-C$_3$N$_4$ photocatalysts for the H$_2$O$_2$ production

Catalyst	Organic sacrificial agent	Irradiation condition	H$_2$O$_2$ yield	Refs.
g-C$_3$N$_4$	Alcohol	$\lambda > 420$ nm	30 μmol (12 h)	[68]
reduced g-C$_3$N$_4$	–	$\lambda > 420$ nm	170 μmol L^{-1} h^{-1}	[70]
AQ/U-POCN	Isopropanol	$\lambda = 400$–780 nm	75 μM h^{-1}	[63]
m-CNNP	Isopropanol	$\lambda = 400$–700 nm	43.07 μmol g^{-1} h^{-1}	[74]
CM-CN3	Ethanol	$\lambda = 400$–800 nm	150 μmol g^{-1} h^{-1}	[75]
ACNT-5	–	simulated sunlight (AM 1.5 filter)	240.36 μmol h^{-1} g^{-1}	[116]
PH-CN	Ethanol	$\lambda = 400$–800 nm	5.2 mmol L^{-1} (12 h)	[85]
DCN-15A	IPA	$\lambda > 420$ nm	12.1 μmol (2.5 h)	[79]
CN-ND	Ethanol	300 W xenon lamp	200 μM (1 h)	[86]
IO CN-Cv	EtOH	300W xenon lamp	325.74 μM (2 h)	[83]
NDCN	Isopropanol	$\lambda \geq 420$ nm	476 μM g^{-1} h^{-1}	[87]
NVCNS	IPA	100 mW cm^{-2}Xe lamp	4413.1 μmol g^{-1} h^{-1}	[117]
0.01% Au/CN	C$_2$H$_5$OH	$\lambda > 420$ nm	2027 μM (30 h)	[90]
Ag@U-g-C$_3$N$_4$-NS	–	100 mW cm^{-2}	0.75×10^{-6} M min^{-1}	[91]
Cu$_2$(OH)$_2$CO$_3$/g-C$_3$N$_4$	–	simulated solar light source	8.9 mmol L^{-1} (6 h)	[98]
PI$_{5.0}$-NCN	–	300W Xe lamp	120 μmol (120 min)	[97]
Bi$_4$O$_5$Br$_2$/g-C$_3$N$_4$	–	$\lambda > 420$ nm	124 μM (60 min)	[99]
1.0 ZIS/CN	IPA	simulated solar (100 mW cm^{-2})	798 μmol h^{-1} g^{-1}	[118]
CN/rGO@BPQDs-0.04	–	$\lambda = 420$–780 nm	181.69 μmol L^{-1} (180 min)	[119]
3DOM g-C$_3$N$_4$-PW$_{11}$	–	$\lambda > 320$ nm	14.4 μmol (360 min)	[105]
g-C$_3$N$_4$-SiW$_{11}$	Methanol	sunlight irradiation (AM 1.5 filter)	91.4 μmol (360 min)	[106]
g-C$_3$N$_4$-PWO	–	$\lambda \geq 420$ nm	11.8 μmol (240 min)	[107]
g-C$_3$N$_4$-CoWO	–	$\lambda \geq 420$ nm	9.7 μmol h^{-1}	[108]
Br doped g-C$_3$N$_4$	EDTA	$\lambda = 400$–800 nm	1.99 mmol L^{-1} (5 h)	[114]
Cu(2)-SCN	EDTA-2Na	$\lambda = 400$–800 nm	4.8 mmol L^{-1} (18 h)	[109]
K$^+$/Na$^+$-doped g-C$_3$N$_4$	–	$\lambda = 400$–800 nm	4.6 mmol L^{-1} (18 h)	[110]
KNiCN	–	$\lambda \geq 420$ nm	398 μmol g^{-1} h^{-1}	[111]
g-C$_3$N$_4$/BDI	2-PrOH	$\lambda > 420$ nm	41 μmol (48 h)	[120]
OCN	Isopropanol	100 mW cm^{-2}	300 μmol (5 h)	[121]
AQ-augmented C$_3$N$_4$	–	simulated solar light (AM 1.5)	361 μmol g^{-1} h^{-1}	[122]
g-C$_3$N$_4$-CNTs	Formic acid	$\lambda \geq 400$ nm	130.2 μmol (240 min)	[123]
Au/C$_3$N$_4$	–	100 mW cm^{-2}	1320 μmol L^{-1} (4 h)	[89]
SS-CN	–	300 W Xe lamp	566.69 μmol g^{-1} h^{-1}	[124]
PT-g-C$_3$N$_4$	Ethanol	$\lambda > 400$ nm	27.07 μmol L^{-1} (60 min)	[125]
C$_v$-gCN	–	$\lambda > 420$ nm	–	[126]
Ni-CAT-CN	–	$\lambda \geq 420$ nm	1801 μmol h^{-1} g^{-1}	[127]

can capture more visible light [46]. Namely, the optical and electronic structures of g-C$_3$N$_4$ photocatalysts can be optimized. For instance, the introduction of carbon vacancies to the surface of g-C$_3$N$_4$ accompanied the appearance of amino group by simple calcination under argon atmosphere (Fig. 3a). In this case, the generated carbon vacancies (Cv-g-C$_3$N$_4$) reduce the band gap of g-C$_3$N$_4$, thereby expanding the absorption of visible light range and increasing excitable electron longevity [71]. Moreover, carbon vacancies offer more sites to adsorb molecular oxygen, beneficial for the transfer of electrons from g-C$_3$N$_4$ to the surface adsorbed O$_2$. Furthermore, this Cv-g-C$_3$N$_4$ photocatalyst alters the H$_2$O$_2$ generation pathway: from a two-step single-electron indirect reduction pathway to a one-step two-electron direct one. This is attributed to generated amino groups around carbon vacancies (Fig. 3b). The activity of Cv-g-C$_3$N$_4$ for the reduction of O$_2$ to H$_2$O$_2$ is 14-fold higher than that of a pure g-C$_3$N$_4$ photocatalyst under irradiation with visible
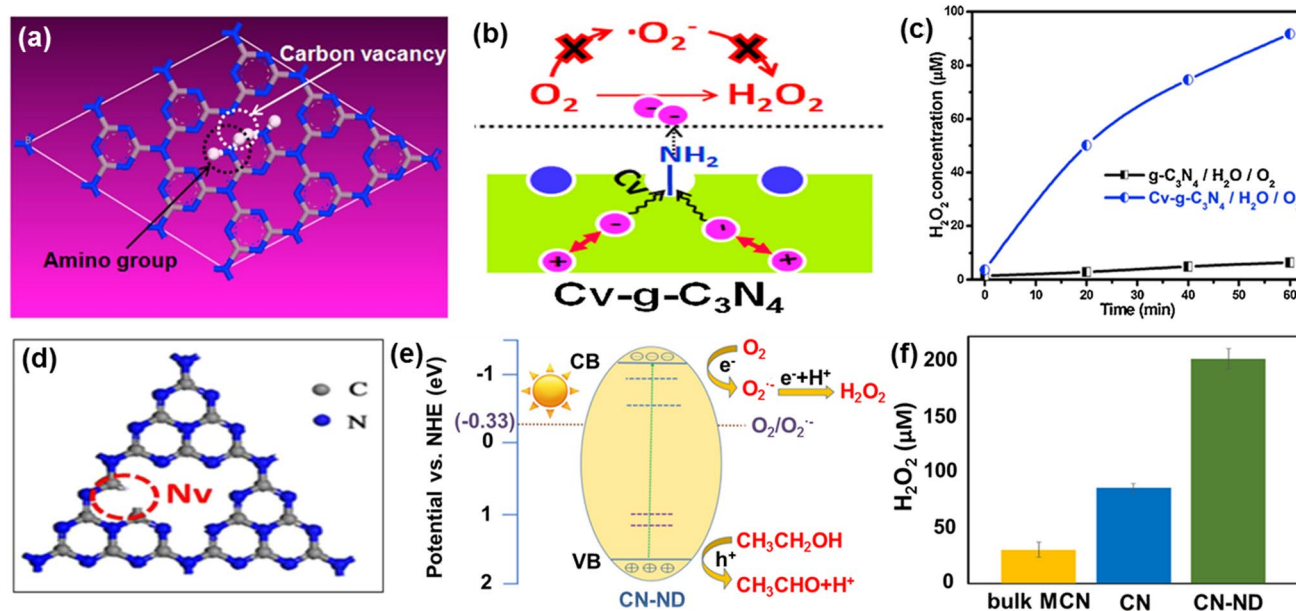
Fig. 3 **a** Schematic illustration of g-C$_3$N$_4$ with carbon vacancy. **b** Mechanism diagram of H$_2$O$_2$ production in Cv-g-C$_3$N$_4$. **c** Concentration of generated H$_2$O$_2$ in g-C$_3$N$_4$ and Cv-g-C$_3$N$_4$ systems. Reproduced with permission from Ref. [71]. Copyright 2016 Elsevier. **d** Schematic illustration of g-C$_3$N$_4$ with nitrogen vacancies (CN-ND). **e** Proposed mechanism for H$_2$O$_2$ generation of CN-ND. **f** H$_2$O$_2$ production of different catalysts. Reproduced with permission from Ref. [86]. Copyright 2021 American Chemical Society

light (Fig. 3c). Carbon vacancies (C$_{vs}$) are then believed to produce more trapping sites, which retards the recombination of photogenerated electrons and holes, eventually resulting in an increased efficiency of the H$_2$O$_2$ generation [83]. Another representative case to strengthen the photocatalytic H$_2$O$_2$ synthesis was achieved via the creation of more vacancies, where an inverse opal (IO) structure was constructed on g-C$_3$N$_4$ accompanying with increased carbon vacancies to improve the separation ability of carriers. This IO g-C$_3$N$_4$ photocatalyst showed an outstanding H$_2$O$_2$ generation yield. For example, 325.74 μM was realized only after 2 h of visible light irradiation. The pathway of the H$_2$O$_2$ production was proposed as following: the electrons on the CB of this photocatalyst are feasible to reduce O$_2$ to form H$_2$O$_2$ because its CB is more negative than that of O$_2$/·O$_2^-$.

Nitrogen vacancies The defects from nitrogen element in/on g-C$_3$N$_4$ photocatalysts are called nitrogen vacancies. Similar to carbon vacancies, they can also facilitate the photocatalytic H$_2$O$_2$ synthesis. For example, nitrogen vacancies in g-C$_3$N$_4$ have been created via the formation of C≡N functional groups by means of thermal reduction treatment [70]. The as-formed nitrogen vacancies narrow down the band gap and make the band edge positively shift,

thus enhancing the visible-light absorption and facilitating photocatalytic H$_2$O$_2$ synthesis [84]. Nitrogen vacancies in carbon nitride also effectively trap photoelectrons, boosting the reduction of N$_2$ to ammonium ions [82]. For the photocatalytic H$_2$O$_2$ synthesis, nitrogen vacancies have been designed and embedded in the g-C$_3$N$_4$ catalyst (PH-CN) using a dielectric barrier discharge (DBD) plasma in H$_2$ atmosphere. Since this photocatalyst improves the separation efficiency of the photogenerated carriers, it displays a H$_2$O$_2$ concentration of 5.2 mmol L^{-1}, 13 times higher than that obtained on a pristine g-C$_3$N$_4$ photocatalyst under the identified conditions [85]. In this case, nitrogen vacancies are assumed not only to serve as active centers for the adsorption of reactive oxygen molecules, but also to alter the electronic band structures of g-C$_3$N$_4$ to harness more visible light in the photocatalytic reaction process. One recently reported the nanostructured g-C$_3$N$_4$ with nitrogen defects was adjusted by cyanuric acid-melamine supramolecular adducts (CN-ND) in the optimum range (Fig. 3d) [86]. Due to the narrowed band gap and the newly formed midgap states, the photocatalytic H$_2$O$_2$ production on CN-ND reached 200 μM under 1 h visible light irradiation, much higher than that obtained bulk g-C$_3$N$_4$ photocatalyst (35 μM)

and the pristine nanostructured g-C$_3$N$_4$ photocatalyst (85 µM) (Fig. 3e, f). Again, such improved performance of photocatalytic H$_2$O$_2$ generation was attributed to these nitrogen vacancies since they promote the visible-light-harvesting capability and retard the recombination rate of photogenerated carriers. Meanwhile, the reaction mechanism of photocatalytic H$_2$O$_2$ production on nitrogen deficiency in carbon nitride has been investigated through coupling experiments with the aid of time-dependent density functional theory (TDDFT) and density functional theory (DFT) calculations [87]. It is disclosed that the introduced bicoordinated nitrogen vacancies play an important role in oxidation, reduction and charge recombination, which are beneficial to the generation of h$^+$, ·O$_2^-$ and ^{1}O$_2$, respectively. Therefore, nitrogen vacancies in carbon nitride can modulate photocatalytic H$_2$O$_2$ generation.

3.1.2 Loading Precious Metal Nanoparticles

The loading of precious metal nanoparticles (NPs) on g-C$_3$N$_4$ forms strong interaction between metallic NPs and g-C$_3$N$_4$, as derived from the delocalization of long electrons in the g-C$_3$N$_4$ matrix. This is one of the most effective approaches to strengthen the photocatalytic activity and selectivity of g-C$_3$N$_4$ since the photogenerated charge separation in such photocatalysts are accelerated, leading to boost photocatalytic reaction in the special pathways [88]. In addition, these photocatalysts suppress the H$_2$O$_2$ decomposition to obtain high yields during photocatalytic H$_2$O$_2$ synthesis. For example, Au NPs deposited on the surface of g-C$_3$N$_4$ by a carbon-layer-stabilized method exhibited a higher photocatalytic yield of H$_2$O$_2$ than the pristine g-C$_3$N$_4$ due to the increased removal of the generated H$_2$O$_2$ from the active reactive sites [89]. In another case, Au NPs were uniformly dispersed on g-C$_3$N$_4$ support (Au/CN) and further utilized to produce H$_2$O$_2$ under visible light irradiation [90]. Its outstanding photocatalytic yield of H$_2$O$_2$ was believed to result from its inertness to catalyze the H$_2$O$_2$ decomposition reaction. The use of 0.01% Au led to the maximum H$_2$O$_2$ production activity (2027 µM) with light irradiation for 30 h, superior to that using other NPs (e.g., Au, Ag, Pd and Pt) on g-C$_3$N$_4$. This high activity of 0.01% Au/CN was attributed to the rapidly reduced recombination of charge carriers. It was derived from the strong interaction between Au and g-C$_3$N$_4$, as testified by obviously quenched PL signal. Photocatalytic H$_2$O$_2$ synthesis for this Au/CN photocatalyst has been further

revealed using *in-situ* electron spin resonance (ESR) technique, indicating so-called direct 2e$^-$ reduction mechanism. With similar aim to extend light absorption region and effectively suppress the recombination of electron–hole pairs for photocatalytic H$_2$O$_2$ synthesis, Ag NPs have also been combined with g-C$_3$N$_4$ [91]. For example, Ag NPs have been loaded on ultrathin g-C$_3$N$_4$ nanosheets (U-g-C$_3$N$_4$-NS) by use of a post gas etching (PGE) technology. These Ag NPs that are uniformly deposited on the surface of single U-g-C$_3$N$_4$-NS layers (Ag@U-g-C$_3$N$_4$-NS) possess significantly stronger adsorption intensity in the 200–2000 nm range than the counterparts in their UV–vis diffuse reflectance spectrum (UV–DRS, Fig. 4a). It was suggested that such enhanced adsorption of Ag@U-g-C$_3$N$_4$-NS was attributed to the special structure of the U-g-C$_3$N$_4$-NS and the localized surface plasmon resonance (LSPR) effect from the Ag NPs. Effective separation of photogenerated carriers helped to adsorb light more efficiently, leading to their enhanced photocatalytic H$_2$O$_2$ activity. An optimal structure of the Ag@U-g-C$_3$N$_4$-NS-1.0 nanocomposite showed excellent photocatalytic activity of H$_2$O$_2$ production with a yield of 1.975×10^{-6} M min^{-1} under visible-light irradiation, even without any sacrificial carbon-containing organic electron donor (Fig. 4b).

3.1.3 Constructing Heterojunction Composites

Using g-C$_3$N$_4$ photocatalysts that contain N and/or C vacancies to prepare H$_2$O$_2$, the organic reagents (such as methanol and ethanol) are frequently added. They usually act as hole scavengers to improve the yield, but contaminate the product of H$_2$O$_2$, and further increase the cost. Note that the potential of VB of g-C$_3$N$_4$ (+1.57 V) is negative than that of ·OH/OH$^-$ (+1.99 V) [92–94], the H$_2$O$_2$ synthesis is thus hard to be realized through photocatalytic H$_2$O oxidation mechanism. Instead, a two-channel H$_2$O$_2$ generation approach (namely O$_2$ reduction and hole oxidation OH$^-$) on g-C$_3$N$_4$ is highly desirable. To overcome these issues, heterogeneous composites of g-C$_3$N$_4$ with other components were constructed. The separation of photogenerated carriers of these composites were enhanced by introduced electron traps, increased potential of VB and created additional active sites. On these composites, the H$_2$O$_2$ generation was achieved via the H$_2$O oxidation pathway. More importantly, this strategy spatially isolates the oxidation and reduction reaction sites, bringing in minimized deactivation of
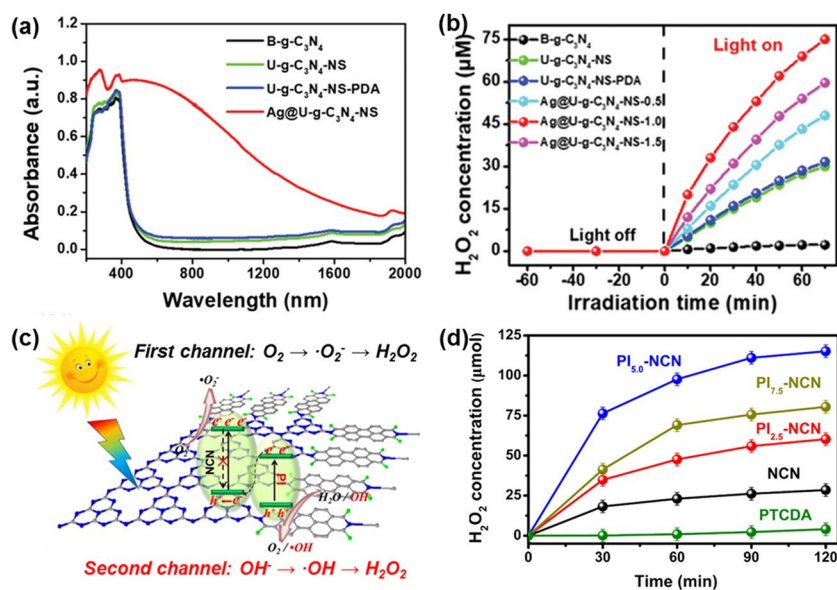
Fig. 4 a UV-DRS absorption spectra of different samples. **b** H_2O_2 concentration of different catalysts. Reproduced with permission from Ref. [91]. Copyright 2019 Wiley–VCH Verlag GmbH & Co. KGaA, Weinheim. **c** Proposed mechanism of different sites on all-solid-state Z-scheme heterojunctions for photocatalytic production of H_2O_2. **d** Concentration of generated H_2O_2 in NCN and PIx-NCN systems. Reproduced with permission from Ref. [97]. Copyright 2017 Elsevier

catalytic ability of these photocatalysts. It has been reported that Z-scheme heterostructures with a wide range of light-trapping properties promoted the separation of photogenerated carriers but without the introduction of hole scavengers and thus rapidly improved the catalytic H_2O_2 production [95, 96]. For example, the combination g-C_3N_4 nanosheets (NCN) with perylene imides (PI) has been reported to form an all-solid-state Z-scheme heterojunction: a g-C_3N_4-based photocatalyst (PI$_x$-NCN), where the excited electrons on the CB of PI are transferred to the VB of NCN, leading to retard recombination of photogenerated carriers (Fig. 4c) [97]. In this case, this PI$_x$-NCN photocatalyst obviously enhanced the charge separation, resulting in an enhanced H_2O_2 yield where more electrons were found to take participate in producing H_2O_2 from O_2 reduction. In addition, since the holes in the VB of PI moiety exhibited more positive potential (2.08 V) than that of NCN (1.63 V), the H_2O_2 generation was assumed to be realized through the direct $2e^-$ WOR approach. In other words, the application of scavengers was avoided here. The optimal PI$_{5.0}$-NCN catalyst showed high activity for the H_2O_2 production: the generation of about 120 μmol H_2O_2 in 120 min under visible-light irradiation (Fig. 4d). Meanwhile, other Z-scheme heterojunction catalysts (e.g., $Cu_2(OH)_2CO_3$/g-C_3N_4 [98] and $Bi_4O_5Br_2$/g-C_3N_4

[99]) have been employed for the two-channel H_2O_2 production under visible-light conditions, thanks to their suitable CB and VB band structures for realizing completed ORR and WOR pathways.

3.1.4 Polyoxometalate Hybridization

Polyoxometalates (POMs) are commonly constructed using a basic unit of oxo-metal polyhedra of MO_x, in which a hole center (O^-) and a trapped electron center (M^{n+}) (n = 5, 6) act as the electron acceptor and donor, respectively [100]. Once POMs are excited by visible light irradiation, they exhibit promising photocatalytic activities and stability. The reason behind is that the reduction of photogenerated-charge recombination is derived from the well-defined HOMO–LUMO band gaps. In this context, POMs have been widely applied in the field of photocatalysis, such as for water oxidation, alcohols oxidation, CO_2 reduction and hydrogen evolution [101–104]. More interestingly, polyoxometalate hybridization strategy has been recently proposed, namely the formation of POM chemical bonds with g-C_3N_4, which was further utilized to improve the photocatalytic H_2O_2 synthesis. For instance, the POM cluster of $[PW_{11}O_{39}]^{7-}$ (PW$_{11}$) has been covalently combined with three dimensionally ordered

macroporous graphitic carbon nitride (3DOM g-C_3N_4), applying for the photocatalytic H_2O_2 synthesis (Fig. 5a) [105]. The hybrid catalyst of 3DOM g-C_3N_4-PW_{11} produced 3.5 μmol H_2O_2 in 60 min irradiated by $λ ≥ 320$ nm light, where no organic electron donor was needed (Fig. 5b). Such a H_2O_2 yield was superior to that of the pure 3DOM g-C_3N_4 catalyst (1.3 μmol), the K-PW_{11} catalyst (<0.1 μmol) and the 3DOM g-C_3N_4-PW_{11}-IMP catalyst (1.5 μmol). It was explained that the covalent bonding of PW_{11} clusters with 3DOM g-C_3N_4 optimizes the VB and the CB of 3DOM g-C_3N_4-PW_{11} when compared with 3DOM g-C_3N_4. Such optimal band structures facilitate both the $2e^-$ WOR pathway and the $2e^-$ ORR pathway for the H_2O_2 production, accompanying with the decreased separation of photogenerated holes and electrons.

On the other hand, 3DOM g-C_3N_4-PW_{11} hybrid catalyst still has some defects. For instance, the number and reactivity of -NH_2 groups of g-C_3N_4 need to be enhanced to further increase the covalent interaction between g-C_3N_4 and POMs. Moreover, the photoreduction ability of POMs needs to be improved to further enhance the selectivity of the $2e^-$ ORR pathway. In this context, the surface of g-C_3N_4 has been modified by its covalent binding with another POM cluster, $[SiW_{11}O_{39}]^{8-}$ (SiW_{11}) via thermal treatment of g-C_3N_4 mixed with urea [106]. The as-prepared g-C_3N_4 catalyst has a larger amount of more highly active-NH_2 groups than

3DOM g-C_3N_4. Via an organic linker bride, the POM SiW_{11} cluster with more negative CB potential than PW_{11} was effectively covalently combined with g-C_3N_4. This g-C_3N_4-SiW_{11} greatly enhanced the adsorption and activation of O_2, thereby promoting the two-electron reduction of O_2 for the H_2O_2 production. It produced 17.8 μmol H_2O_2 in 60 min under simulated sunlight (AM 1.5) irradiation together with the selectivity as high as 80.1% in the presence of methanol. The high selectivity of O_2 reduction to H_2O_2 was attributed to a positive shift of the CB level in g-C_3N_4-SiW_{11}.

The hybrid catalysts of g-C_3N_4 with POM-derived metal oxides were prepared by the thermal decomposition of the mixture of g-C_3N_4 and POM precursors. These POM-derived metal oxides increase the H_2O_2 production by enhancing photoinduced generation of electrons. Using such a calcination method, the g-C_3N_4-PWO [107] and g-C_3N_4-CoWO [108] have been prepared. Take g-C_3N_4-PWO as an example (Fig. 5d), it showed a H_2O_2 yield of 6.3 μmol in 60 min under visible light but in the absence of organic electron donor, outperforming that of the counterparts (Fig. 5e). This is because the incorporation of PWO into the g-C_3N_4 framework results in the negative shift of the CB edge of g-C_3N_4. The H_2O_2 production was achieved formed a two-step single-electron O_2 reduction reaction routine, namely from $1e^-$ reduction pathway (from O_2 to $·O_2^-$),
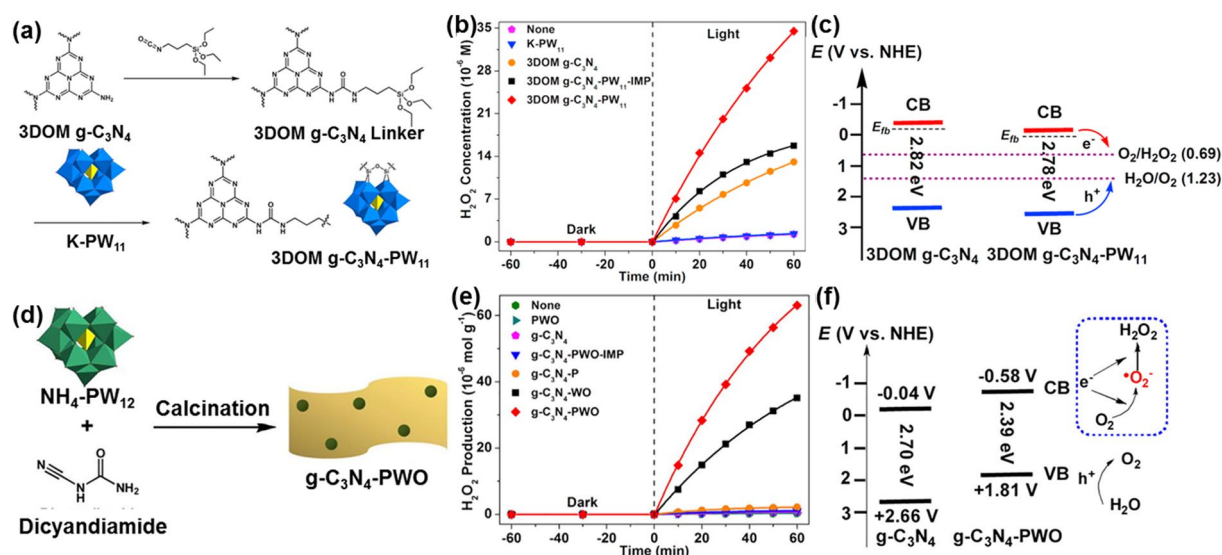
Fig. 5 **a, d** Schematic illustration of the synthetic route to 3DOM g-C_3N_4-PW_{11} and g-C_3N_4-PWO. **b, e** H_2O_2 production over different catalysts in 60 min. **c, f** Scheme of energy levels and charge transfer pathways of 3DOM g-C_3N_4 and 3DOM g-C_3N_4-PW_{11}, g-C_3N_4 and g-C_3N_4-PWO. Reproduced with permission from Refs. [105, 107]. Copyright 2017 Elsevier and 2018 Elsevier

and sequentially followed by another $1e^-$ reduction pathway (from $\cdot O_2^-$ to H_2O_2) (Fig. 5f).

3.1.5 Metal/Non-metal Element Doping

Doping of metal/non-metal element into $g-C_3N_4$ modulates the bandgap of $g-C_3N_4$ and further alters the transfer directions of charge carriers, thereby adjusting electronic, optical and other physical properties of $g-C_3N_4$. Moreover, the heteroelements on $g-C_3N_4$ change the reaction pathways of the H_2O_2 generation. Therefore, doping of metal/non-metal element into $g-C_3N_4$ has been proposed as a potential strategy to improve the performance of photocatalytic H_2O_2 generation. In a typical case, Cu-doped $g-C_3N_4$ microspheres, denoted as Cu-SCN, have been synthesized using a modified template method (Fig. 6a) [109]. The Cu species were inserted into the interstitial position of SCN with a special mesoporous structure, resulting in the formation of the coordinated Cu–N bonds. The Cu-doping not only decreased the bandgap of $g-C_3N_4$ to enhance its capture of visible light, but also retarded the recombination of photogenerated carriers, as testified from lower PL intensity of Cu(2)-SCN than that of GCN. In addition, Cu(2)-SCN showed a weaker PL intensity in O_2 atmosphere when compared with that in Ar (Fig. 6b). The performance of photocatalytic H_2O_2 production using the Cu-doped $g-C_3N_4$ photocatalyst was thus superior to that of the $g-C_3N_4$ photocatalyst. From the X-ray photoelectron spectroscopy (XPS) of Cu-doped $g-C_3N_4$ photocatalyst, Cu^+ was observed in its XPS spectrum of Cu 2p. Such Cu(I)-N site thus served as the adsorption center for molecular O_2 to increase the O_2 adsorption. Moreover, it changes the transfer pathways of photoelectrons from the catalyst to the adsorbed O_2, altering in a two-step single-electron reaction pathway to a one-step two-electron reduction process. In the other study, K^+ and Na^+ ions have been co-doped into $g-C_3N_4$ through a molten salt method [110]. The incorporation of alkali metals in $g-C_3N_4$ tuned the band gap of $g-C_3N_4$, increased its specific surface area and reduced the size of $g-C_3N_4$ layered structure. Therefore, this alkali metals co-doped $g-C_3N_4$ photocatalyst can enhance the visible-light adsorption and promote the separation of photoelectron-hole pairs to boost photocatalytic performance toward H_2O_2 production. In more detail, the VB potential of GCN(20) is $+2.05$ V, more positive than that ($+1.99$ V) of $\cdot OH/OH^-$. This was derived from alkali metal incorporation. In this context, the reaction process of photocatalytic H_2O_2 generation was changed from a single pathway ($O_2 \rightarrow H_2O_2$) to a dual channel pathway ($O_2 \rightarrow H_2O_2$ and $OH^- \rightarrow \cdot OH \rightarrow H_2O_2$), a very attractive method for practical solar-to-chemical applications (Fig. 6c). The MCN(20) produced the H_2O_2 concentration of 4.6 mmol L^{-1}, more than 9 times higher than that produced by GCN (Fig. 6d). Furthermore, a crystalline $g-C_3N_4$ modified with K^+, Ni and N-doped carbon (KNiCN) was fabricated to overcome the inherent structural defects and low carrier separation efficiency [111]. The synergistic effects between K^+, Ni species and N-doped carbon increased the light adsorption, improved charge separation and boosted O_2 adsorption and selectivity for the H_2O_2 generation. A two-electron reduction pathway was suggested (Fig. 6e). This photocatalyst displayed a photocatalytic H_2O_2 yield of as high as 79.6 µM in O_2-saturated pure water (Fig. 6f).

In addition to metal doping of $g-C_3N_4$, halogen doping, another classic non-metal doping has been used to synthesize photocatalysts for photocatalytic H_2O_2 production. In these cases, the incorporation of halogen into $g-C_3N_4$ not only reduces the bandgap (to enhance the visible-light absorption and improve the electrical conductivity), but also boost charge carrier transmission rates (without damaging of main structures of the $g-C_3N_4$ polymer). These features benefit much photocatalytic H_2O_2 synthesis [112, 113]. For example, halogen doped $g-C_3N_4$, prepared by means of a hydrothermal method in saturated NH_4X ($X = Cl$, Br) solution followed with a post-treatment, has more negative CB potential than $g-C_3N_4$ [114]. This catalyst is thus beneficial for the O_2 reduction into H_2O_2. For example, a Br-doped $g-C_3N_4$ photocatalyst showed higher photocatalytic H_2O_2 production capacity (1.99 mmol L^{-1}) in comparison with the counterparts. The incorporation of multiple heteroelements into the $g-C_3N_4$ framework with various configurations was also demonstrated to tune the bandgap of $g-C_3N_4$ [115]. One co-doped $g-C_3N_4$ photocatalyst exhibited an outstanding photocatalytic activity for the H_2O_2 generation, which is 17–25 times higher than that of bare $g-C_3N_4$.

3.2 TiO₂ Photocatalysts

TiO_2 is the most famous photocatalyst since the discovery of its photocatalytic activity by Fujishima and Honda for the first time in 1972 [128]. It possesses many advantages
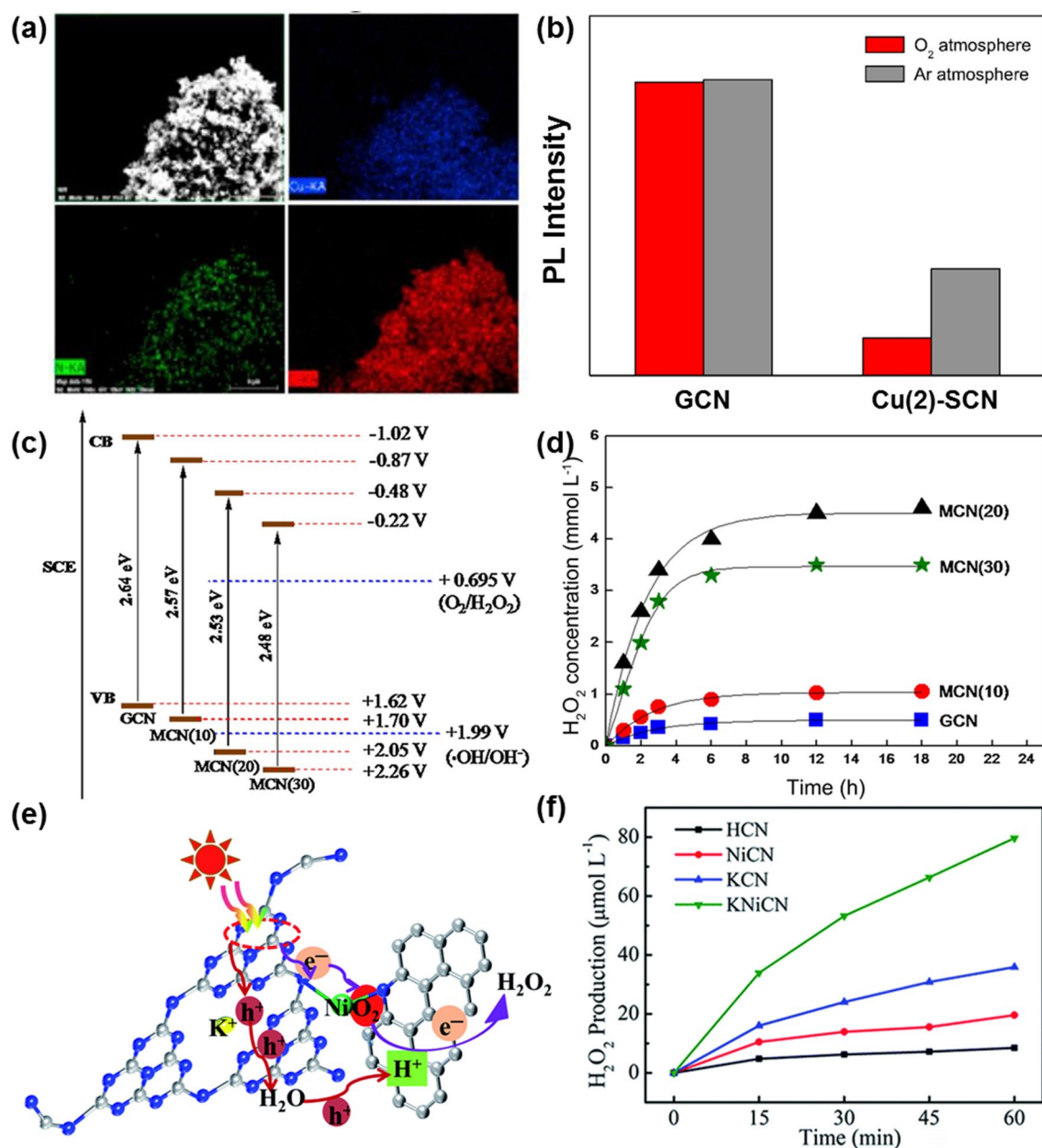
Fig. 6 a Elemental mapping images of Cu(2)-SCN. **b** PL intensities of GCN and Cu(2)-SCN. Reproduced with permission from Ref. [109]. Copyright 2017 Elsevier. **c** Band gap structures of various catalysts. **d** H_2O_2 concentration over catalysts under visible light. Reproduced with permission from Ref. [110]. Copyright 2018 Elsevier. **e** Proposed mechanism of H_2O_2 production over the KNiCN catalyst. **f** Photocatalytic H_2O_2 production on the catalysts in pure water. Reproduced with permission from Ref. [111]. Copyright 2021 Royal Society of Chemistry

for photocatalytic reactions, such as appropriate site for the CB, good physical and electrical properties, stable chemical structures and outstanding biocompatibility [129]. The potential of the CB of TiO_2 (E^θ) is -0.5 V_{NHE}, which is negative enough to drive a $2e^-$ ORR for the H_2O_2 production [16]. The generated photoelectrons in their CBs

reduce O_2 to form H_2O_2, following the reaction of $O_2 + 2$ $H^+ + 2$ $e^- \rightarrow H_2O_2$. While these simultaneously generated holes in their VBs oxidize water to generate O_2 and H^+, following the process of $H_2O + 2$ $h^+ \rightarrow 1/2$ $O_2 + 2$ H^+. The free Gibbs Energy (ΔG) of such a photocatalytic process is 117 kJ mol^{-1}. An uphill reaction indicates thermodynamical

unfavorablity [13, 120]. TiO_2 photocatalysts also have been confirmed to feature low cost, low toxicity, high chemical- and photo-stability during the H_2O_2 production [130–132].

However, the concentration of H_2O_2 produced by pure TiO_2 photocatalyst has been only confined to the micromolar level (< 0.2 mM) [133]. This is because TiO_2 photocatalyst can be excited only by UV light irradiation to generate photocarriers, due to the large band gap of TiO_2 photocatalyst [47]. Besides, the formed H_2O_2 on the TiO_2 surface is not stable enough and is easy to be converted to Ti-OOH complexes when it is in touch with the Ti–OH groups on the TiO_2 surface. Subsequently, Ti-OOH is decomposed, following the reduction reaction of $Ti\text{-}OOH + H^+ + e^- \rightarrow Ti\text{–}OH + OH^-$ [134]. In order to address the drawbacks of these TiO_2 photocatalysts, surface modification strategies on TiO_2 photocatalysts have been validated and applied to facilitate the photocatalytic H_2O_2 production, covering loading precious metal nanoparticles, modifying graphene quantum dots and complexing with cation and anion surfaces (Table 2).

3.2.1 Loading Precious Metal Nanoparticles

The NPs from individual precious metals have been loaded on the TiO_2 surface to enhance the photocatalytic activity of TiO_2 photocatalysts. In 2010, the synthesis of the Au/TiO_2 photocatalyst has been reported using a deposition–precipitation (DP) method [133]. The as-obtained Au/TiO_2 photocatalyst exhibited a high yield in the photocatalytic H_2O_2 production. The reported H_2O_2 concentration reached 10 mM under UV-irradiation. The mechanism of the H_2O_2 formation on this Au/TiO_2 photocatalyst was explained as following (Fig. 7a). The oxidation and reduction sites on the Au/TiO_2 photocatalyst are separated to TiO_2 and Au NPs, respectively. The activity for photocatalytic H_2O_2 formation can be adjusted by k_f (the formation rate constant) and k_d (the decomposition rate constant). In another work, Au NPs with a bimodal size distribution were loaded on rutile TiO_2 (BM-Au/TiO_2), which was further modified with carbonates to obtain BM-Au/TiO_2-CO_3^{2-} (Fig. 7b) [135]. The UV/Vis absorption spectra of BM-Au/TiO_2-CO_3^{2-} indicated that the loading of Au NPs results in strong and extensive absorption in visible light region because of the LSPR of Au NPs. This BM-Au/TiO_2 photocatalyst yielded 640 ± 60 μM H_2O_2 under visible-light irradiation for 1 h when 4% HCOOH was presented as the sacrificial agent. Such a yield was much higher than that of single small Au/TiO_2 photocatalyst (50 μM) and single large Au/TiO_2 photocatalyst (75 μM) (Fig. 7c). The improvement on the H_2O_2 yield on the BM-Au/TiO_2-CO_3^{2-} was believed to be mainly originated from the occurred long-range charge separation by the visible-light-induced, vectorial interfacial electron transfer

Table 2 Summary of TiO_2 photocatalysts for the H_2O_2 production

| Catalyst	Organic sacrificial agent	Irradiation condition	H_2O_2 yield	AQY (%)	Refs.
Co@TiO_2	–	$\lambda = 400$ nm	1.71 mmol dm^{-3}(60 min)	–	[131]
TiO_2	Benzylic alcohol	$\lambda > 280$ nm	40 mM (12 h)	29.1 ($\lambda = 334$ nm)	[148]
Au/SnO_2–TiO_2	Alcohol	UV	~ 15 mM (25 h)	–	[149]
Au/[SnO_2–NR#TiO_2]	Ethanol	$\lambda > 430$ nm	~ 60 μM (6 h)	–	[150]
RuO_2#TiO_2-Au	–	$\lambda > 300$ nm	~ 80 μM (1 h)	–	[151]
Au/TiO_2	C_2H_5OH	$\lambda > 300$ nm	~ 6 mM (24 h)	13 ($\lambda = 355 \pm 23$ nm)	[133]
BM-Au/TiO_2 − CO_3^{2-}	Formic acid	$\lambda > 430$ nm	640 ± 60 μM(1 h)	5.4 ($\lambda = 530$ nm)	[135]
AuAg/TiO_2	Ethanol	$\lambda > 280$ nm	3.4 mM (12 h)	–	[139]
Pd/APTMS/TiO_2	–	simulated sunlight irradiation	150 μM h^{-1}	–	[152]
SN-GQD/TiO_2	2-propanol	$\lambda \geq 300$ nm	451 μM (60 min)	–	[143]
Nf-SNG/TiO_2	2-propanol	$\lambda \geq 300$ nm	745.5 μM (120 min)	–	[144]
HTNT-CD	–	$\lambda > 365$ nm	84.7 μmol (1 h)	5.2 ($\lambda = 365$ nm)	[153]
Cu^{2+}/TiO_2	–	$\lambda = 300$–400 nm	8 μM (5 min)	–	[145]
F-TiO_2	HCOOH	$\lambda = 360$ nm	1–1.3 mM	–	[147]
Zn^{2+}/TiO_2	–	mercury lamp (125 W)	0.22 mM (3 h)	–	[146]
TiO_2-PW_9	Benzyl alcohol	$\lambda = 200$–1100 nm	38.2 μmol (2 h)	–	[154]
rGO/TiO_2/CoPi	2-propanol	$\lambda \geq 320$ nm	80 μM (3 h)	–	[155]
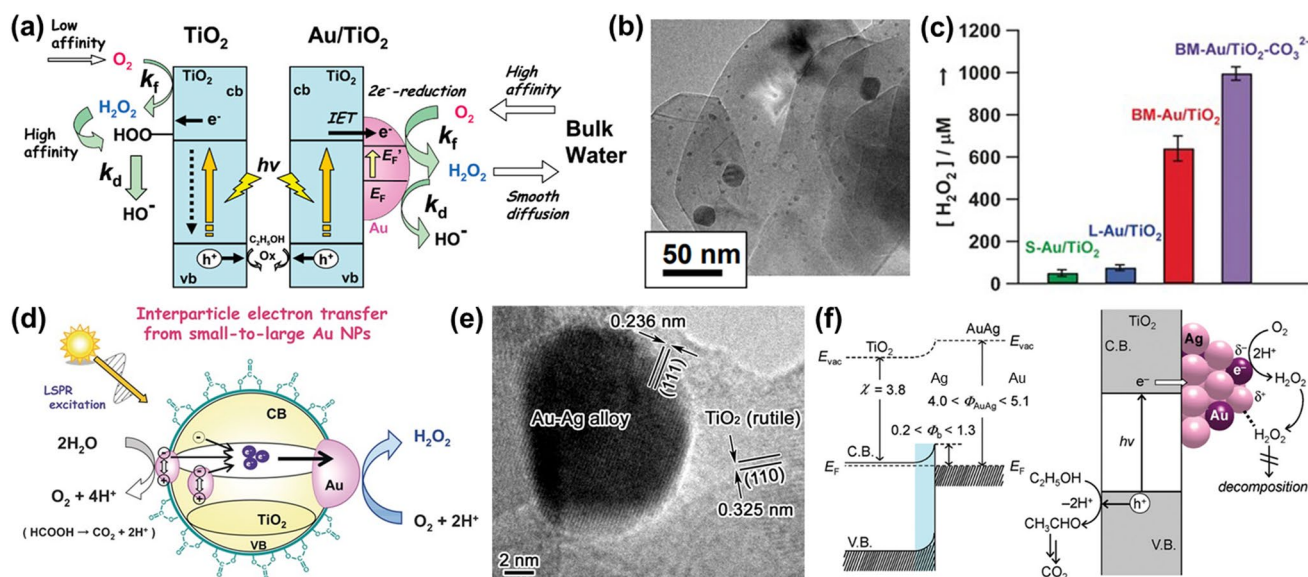
Fig. 7 **a** Mechanism of the H_2O_2 formation over the Au/TiO_2 photocatalyst. Reproduced with permission from Ref. [133]. Copyright 2010 American Chemical Society. **b** TEM image of the BM-Au/TiO_2 photocatalyst. **c** Photocatalytic H_2O_2 production on various photocatalysts. **d** Proposed mechanism of the BM-Au/TiO_2-CO_3^{2-} plasmonic catalyst in the photocatalytic H_2O_2 generation. Reproduced with permission from Ref. [135]. Copyright 2016 Wiley–VCH Verlag GmbH & Co. KGaA, Weinheim. **e** HRTEM image of the $Au_{0.1}Ag_{0.4}$/TiO_2 photocatalyst. **f** Schematic energy-band and mechanism of the H_2O_2 production on the AuAg/TiO_2 photocatalyst. Reproduced with permission from Ref. [139]. Copyright 2012 American Chemical Society

in the way of S–Au→CB-(TiO_2)→L-Au. It is known that the generated H_2O_2 on a pure TiO_2 photocatalyst is easily degraded since it can be reduced by the peroxide species (Ti_s-OOH) on the TiO_2 surface. However, the modification of CO_3^{2-} onto the TiO_2 surface efficiently inhibits such reductive degradation of H_2O_2. The concentration of generated H_2O_2 on this BM-Au/TiO_2-CO_3^{2-} thus reached about 1 mM. The mechanism of the H_2O_2 generation on the BM-Au/TiO_2-CO_3^{2-} photocatalyst includes plasmonic effect and photocatalytic O_2 reduction (Fig. 7d). It has been further reported that the photocatalytic kinetics for the H_2O_2 formation is dependent on temperature and pH value for the deposition of Au NPs on anatase TiO_2 when a heating temperature-varied deposition–precipitation technique was applied [136]. The amount of generated H_2O_2 under the irradiation was increased with a decrease of the temperature and pH in the reaction system. The highest H_2O_2 concentration produced on the Au/anatase TiO_2 photocatalyst was about 17 mM at the temperature of 5 °C in the solution with a pH value of 2. In conclusion, these introduced metal Au NPs on the TiO_2 surface prohibit the H_2O_2 decomposition that is induced by the Ti–OH species. Meanwhile, they capture photogenerated electrons in the CB of TiO_2, leading

to retarded recombination of photogenerated carriers. The output of the H_2O_2 production on these photocatalysts was obviously increased. The H_2O_2 concentration even reached the millimolar level. Nevertheless, the generated H_2O_2 molecules are inclined to be adsorbed on Au NPs due to their strong interactions. Subsequently, spontaneous decomposition of H_2O_2 occurs: $H_2O_2 + e^- \rightarrow \cdot OH + OH^-$ [137, 138].

To promote the H_2O_2 formation and simultaneously inhibit its decomposition on the TiO_2 photocatalysts, the NPs from bimetal alloys have been deposited on the TiO_2 surface to enhance the photocatalytic activity. For example, a bimetal alloy catalyst (AuAg/TiO_2) has been designed and applied for photocatalytic H_2O_2 generation (Fig. 7e) [139]. The H_2O_2 concentration produced by the $Au_{0.1}Ag_{0.4}$/TiO_2 photocatalyst was as high as 3.4 mM, approximately 7 times higher than that produced on a pure TiO_2 photocatalyst. This excellent photocatalytic performance has been attributed to the following two aspects (Fig. 7f). Firstly, the work function of the alloy AuAg is located between Au and Ag. The alloy/TiO_2 photocatalyst produces a barrier, of which energy is larger than that of the Ag/TiO_2 photocatalyst but smaller than that of Au/TiO_2 photocatalyst. Effective separation of hole-electron pairs is thus possible. Secondly, electron transfer

from Ag to Au takes place, because Au atoms have a higher electronegativity than Ag atoms. In other words, the electron density of Au is increased, suppressing the H_2O_2 adsorption on Au atoms. Such statements were further proved using the DFT simulations. The affinity between the H_2O_2 and Au atoms was confirmed to be weakened via the alloy effect. It was taken place that H_2O_2 is inclined to be adsorbed on Ag atoms, thus inhibiting the H_2O_2 decomposition. In another case, the midgap state in the $Ag_2Au_2@TiO_2$ (101) photocatalyst was reveal to own a suitable position for the H_2O_2 production via a photocatalytic reaction, as demonstrated by the DFT analysis. More importantly, the photoresponse of these bimetal alloy photocatalytic systems is rapidly promoted in visible and infrared light region, improving the H_2O_2 yield [140].

3.2.2 Modifying Graphene Quantum Dots

Graphene quantum dots (GQDs) feature advantages of high chemical stability, good biocompatibility, large surface area and high extinction efficiencies (that are derived from the atomically thin sp^2 carbon structure of graphene). GQDs exhibit unique luminescent characteristic. Therefore, GQDs have attracted extensive attention in various photocatalytic applications. Especially, the sensitization of GQDs with other wide band gap photocatalysts (e.g., TiO_2) can extend light-adsorption range from ultraviolet to the visible region [141, 142]. For example, sulfur and nitrogen co-doped graphene quantum dots (SN-GQDs) have been combined with the TiO_2 photocatalyst (SN-GQD/TiO_2) and further applied for photocatalytic H_2O_2 production [143]. As confirmed from related UV–vis diffuse reflectance spectra (DRS), SN-GQD/TiO_2 exhibited obviously enhanced adsorption in visible light region when compared with the pure TiO_2 photocatalyst. On its surface, more than 82.8 µM H_2O_2 was produced under visible light irradiation only for 90 min. Such a yield was about 5.3 and 3.1 times larger than that generated on the GQD/TiO_2 photocatalyst and the N-GQD/TiO_2 suspensions under the same conditions, respectively (Fig. 8a). Theoretical calculation and free energy diagram analysis showed that the H_2O_2 generation on the SN-GQD/TiO_2 photocatalyst followed a proton-coupled electron transfer (PCET) mechanism. Namely, high selectivity of the H_2O_2 generation on the SN-GQD/TiO_2 photocatalyst was realized via a $2e^-$ ORR pathway (Fig. 8b, c). A Nafion layer was further introduced into the SN-GQD/TiO_2 (Nf-SNG/TiO_2) to facilitate the H_2O_2 generation [144]. The GQDs coupled with a Nafion layer were found not only to improve the
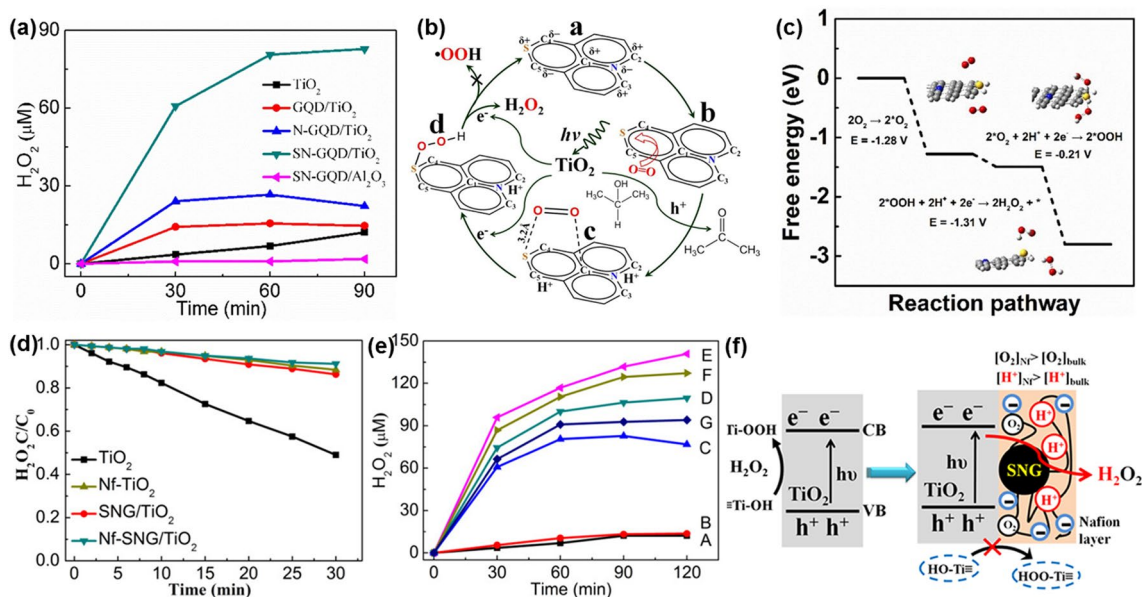
Fig. 8 **a** Photocatalytic H_2O_2 generation on the catalysts. **b** Proposed mechanism of photocatalytic H_2O_2 formation over the SN-GQD/TiO_2 photocatalyst. **c** Free energy diagrams of reaction pathways. Reproduced with permission from Ref. [143]. Copyright 2018 Elsevier. **d** Photocatalytic decomposition and **e** production of H_2O_2 on different catalysts under visible light. **f** Photocatalytic reaction mechanism for H_2O_2 formation on the Nf-SNG/TiO_2 photocatalyst. Reproduced with permission from Ref. [144]. Copyright 2019 American Chemical Society

visible light adsorption, but also to significantly hinder the H_2O_2 decomposition (Fig. 8d). The yield of photocatalytic H_2O_2 production on the Nf-SNG/TiO$_2$ photocatalyst with 3.5% Nafion content was 141 µM after 120 min visible light irradiation than that obtained on the counterparts (Fig. 8e). Related photocatalytic reaction mechanism of the H_2O_2 formation on Nf-SNG/TiO$_2$ was testified to follow a two-electron-dominated ORR pathway (Fig. 8f). It was impacted by GQDs sensitization, different from photocatalytic H_2O_2 production on the pure TiO$_2$ photocatalyst.

3.2.3 Complexing with Cation and Anion Surfaces

The surface states are important during photocatalytic H_2O_2 generation, since photocatalytic reactions are surface-controlled processes. Therefore, various surface modification approaches have been developed to modulate photocatalytic activities of TiO$_2$ photocatalysts. Among them, complexing cations or anions onto the TiO$_2$ surface has been wildly accepted as the simplest one to effectively boost the photocatalytic H_2O_2 production. For example, the inner spherical surface of the metal cations can modulate interfacial electron transfer via suppressing the surface trapping sites for photogenerated carriers during the photocatalytic process. Taking the modification of TiO$_2$ by Cu^{2+} ion as an example, it has been revealed that complexing with a small amount of Cu^{2+} onto the TiO$_2$ surface significantly promoted the photocatalytic activity of H_2O_2 production [145]. A 20-fold increment in the amount of generated H_2O_2 was achieved under UV irradiation in comparison with that on the TiO$_2$ photocatalyst without Cu^{2+} modification. When the concentration of Cu^{2+} was in the range of 30–40 µM, the performance for photocatalytic H_2O_2 generation remained stable. Such enhanced activity of photocatalytic H_2O_2 production was proposed to be dependent on the optimization of the TiO$_2$ surface state through Cu^{2+} modification, eventually promoting the H_2O_2 formation on the TiO$_2$ surface via a $2e^-$ ORR pathway. In another case, Zn^{2+} ions were complexed onto the TiO$_2$ photocatalyst [146]. This Zn^{2+} modified TiO$_2$ photocatalyst exhibited obviously improved performance of photocatalytic H_2O_2 generation. Since Zn^{2+} ions block the $\equiv$Ti–OH sites, the complexation of peroxide/superoxide species on the TiO$_2$ surface is thus much limited, resulting in reduced H_2O_2 decomposition.

In addition to cations, complexing with anions onto the TiO$_2$ photocatalyst has been also applied for the photocatalytic H_2O_2 production. For instance, the fluorinated TiO$_2$ photocatalyst exhibited a boosted reaction toward photocatalytic H_2O_2 generation. Stemming from surface state modulation via F$^-$ modification, this fluorinated TiO$_2$ photocatalyst suppresses the Ti-OOH formation. It produced H_2O_2 with a concentration of 1.3 mM under UV light irradiation, one of the best activities among the reported TiO$_2$ photocatalysts for the H_2O_2 generation [147].

3.3 BiVO$_4$ Photocatalysts

In addition to TiO$_2$ photocatalysts, some more complex inorganic oxides have also been employed for photocatalytic H_2O_2 generation. Among them, bismuth vanadate (BiVO$_4$) is one classic representative of bimetallic oxide photocatalyst [156–159]. Again, it is well known a pure TiO$_2$ photocatalyst has a wide bandgap and thus can be excited only under UV light irradiation, resulting in insufficient activity for photocatalytic H_2O_2 generation in sunlight [160, 161]. Distinguished from a TiO$_2$ photocatalyst, BiVO$_4$ has its appropriate band structure and is thus active in the visible light region. In other words, it can promote the H_2O_2 production via a $2e^-$ ORR pathway under the visible-light irradiation [162]. Unfortunately, pure BiVO$_4$ is not conducive to the efficient photocatalytic H_2O_2 production, due to its lack of active sites for the $2e^-$ ORR. In this context, nano-Au cocatalyst was introduced onto the BiVO$_4$ surface. Stemming from the strong interaction between Au and BiVO$_4$, the activation of the special d-band electrons promoted the selectivity of the $2e^-$ ORR pathway to efficiently generate H_2O_2 under visible light irradiation (Fig. 9a) [163]. This is because of the edge in the CB of BiVO$_4$ was disclosed to be 0.02 V, more positive than that (−0.13 V) of one-electron reduction of O_2 and more negative than that (0.68 V) of two-electron reduction of O_2 (Fig. 9b). The inhibition of single electron reduction over the Au/BiVO$_4$ surface was further identified by electron spin resonance (ESR) spectra, where Au$_{0.2}$/BiVO$_4$ exhibits almost no signal, while Au$_{0.2}$/TiO$_2$ displays distinctive signals (Fig. 9c). The latter was ascribed to the DMPO $-$ ·OOH spin adduct formation.

Nevertheless, the activity of the BiVO$_4$ photocatalyst toward photocatalytic H_2O_2 production still remains unsatisfactory. This is mainly attributed to the formed built-in field between Au and BiVO$_4$, which inhibits the transfer of photogenerated electrons as well as accumulates
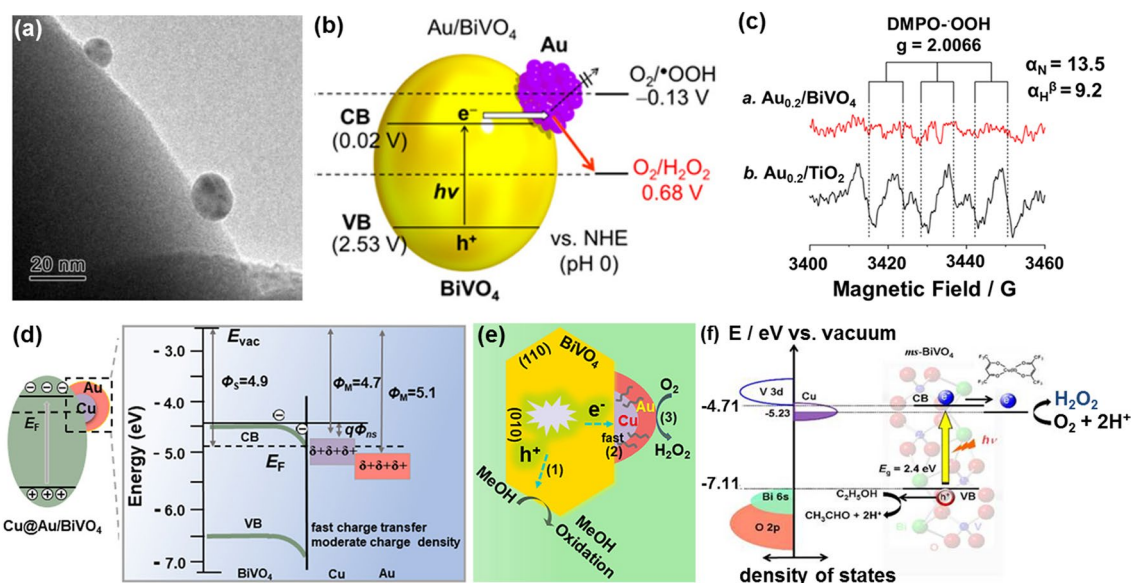
Fig. 9 **a** TEM image of an $Au_{0.2}$/BiVO$_4$ photocatalyst. **b** Energy diagram of the Au/BiVO$_4$ photocatalyst and reduction potential of O$_2$. **c** ESR spectra of an $Au_{0.2}$/BiVO$_4$ photocatalyst and an $Au_{0.2}$/TiO$_2$ photocatalyst in an EtOH/water/O$_2$ system with DMPO. Reproduced with permission from Ref. [163]. Copyright 2016 American Chemical Society. **d** Energy diagram of a Cu@Au/BiVO$_4$ photocatalyst. **e** Mechanism of H$_2$O$_2$ generation on a Cu@Au/BiVO$_4$ photocatalyst. Reproduced with permission from Ref. [166]. Copyright 2021 American Chemical Society. **f** Energy diagram and the reaction mechanism of a Cu(hfacac)$_2$/ms-BiVO$_4$ photocatalyst. Reproduced with permission from Ref. [167]. Copyright 2020 American Chemical Society

negative charges of Au to deteriorate the 2e$^-$ ORR pathway [164, 165]. In order to overcome this impediment, one Cu@Au/BiVO$_4$ photocatalyst was designed and obtained using combined photodeposition and galvanic displacement methods [166]. The Cu species was found to facilitate the transfer of photogenerated electrons from BiVO$_4$ to Au. The accumulation of negative charges on Au was then reduced, resulting in the enhanced activity for the photocatalytic H$_2$O$_2$ production (Fig. 9d, e). Specifically, the ohmic contact was expected to be produced between Cu and BiVO$_4$ since their work functions (Φ) are different: Φ_{Cu}= 4.7 eV and Φ_{BiVO_4}= 4.9 eV. Transferring of the photogenerated electrons is thus beneficial. The photogenerated electrons that are transferred from Cu to Au eventually boost the two-electron O$_2$ reduction pathway, namely the H$_2$O$_2$ formation. On the other hand, photogenerated charges have been accumulated on the nano-Au cocatalyst in the Cu@Au/BiVO$_4$ photocatalyst, leading to the generation of stronger adsorption of O$_2$ and HOO* on the Au surface of Cu@Au/BiVO$_4$. Consequently, O$_2$ reduction to form H$_2$O$_2$ is accelerated. For a bis(hexafluoroacetylacetonato) Cu(II) adsorbed monoclinic scheelite (ms)-BiVO$_4$ photocatalyst (Cu-(hfacac)$_2$/

ms-BiVO$_4$), it exhibited an outstanding activity of photocatalytic H$_2$O$_2$ generation [167]. An external quantum yield of 0.47% was reported under visible light irradiation (λ_{ex}= 470 nm). Such performance was attributed to the enhanced charge separation by the interfacial electron transfer from ms-BiVO$_4$ to the surface complex and the O$_2$-enriching effect near the surface of ms-BiVO$_4$, as well as outstanding electrocatalysis for a 2e$^-$ ORR pathway (Fig. 9f).

3.4 CdS Photocatalysts

CdS has exhibited promising photocatalytic activities in various reactions under visible light irradiation, since the potential of its VB is positive enough to drive water oxidation and meanwhile the potential of its CB is more negative to promote O$_2$ reduction. CdS thus has great potential to be applied as a catalyst for photocatalytic H$_2$O$_2$ production [168–170]. Unfortunately, CdS exhibits relatively low photocatalytic capability toward H$_2$O$_2$ generation, originating from its weak adsorption capacity for reactants and its poor photostability. More seriously,

its easy aggregation can cause the severe recombination of photogenerated carriers [171].

To improve the performance of CdS for photocatalytic H_2O_2 production, many efforts have been made and several strategies have been proposed. One strategy is to complex organic polymers onto CdS. For example, the hybrids of CdS and reduced graphene oxide (CdS-RGO) prepared through a hydrothermal process significantly boosted the kinetics of photocatalytic H_2O_2 generation when compared with pure CdS photocatalyst (Fig. 10a) [172]. The CdS-RGO photocatalyst with a 20 wt% RGO content (CdS-G2) produced the H_2O_2 concentration of as high as 128 μM under sunlight irradiation for 12 h. Such enhancement was mainly attributed to accelerated separation of photogenerated carriers due to the enhanced electron transfer from the photoexcited CdS to RGO, the increment of visible light absorption and more active reaction sites (as demonstrated by their PL spectra (Fig. 10b)). The mechanism of photocatalytic H_2O_2 production on the CdS-RGO photocatalyst was also discussed (Fig. 10c). In the first step, electron–hole pairs are generated on the CdS-RGO photocatalyst upon its excitation by light irradiation. Water molecules are then oxidized by photogenerated holes, leading to the production of H_2O_2 and protons. Simultaneously, O_2 is reduced to form H_2O_2, following a $2e^-$ ORR pathway (step 1–4). These photogenerated electrons have been demonstrated to play a vital role in the process of photocatalytic H_2O_2 generation. The H_2O_2 yield from a $2e^-$ ORR pathway is the decisive factor when compared with that from the $2e^-$ WOR pathway in the whole photocatalytic process.

Noble metals have also been complexed onto CdS to improve the photocatalytic performance of CdS catalysts. For example, the CdS-Pt and CdS-Au nanorods exhibited enhanced photocatalytic activity to produce H_2O_2 when compared with a pure CdS photocatalyst [173]. The Au tip with a smaller size was found to be more efficient as reactive site to form H_2O_2 than a Pt tip. This was attributed to different surface reactivity and selectivity related to the metal tip composition. On these CdS-metal photocatalysts, the H_2O_2 production through ORR pathway has been confirmed, instead of the WOR pathway. A CdS/sulfur-doped carbon nanocomposite, synthesized by thermal annealing of Cd(EDDA) MOF, exhibited outstanding activity toward photocatalytic H_2O_2 production [174]. This is due to the
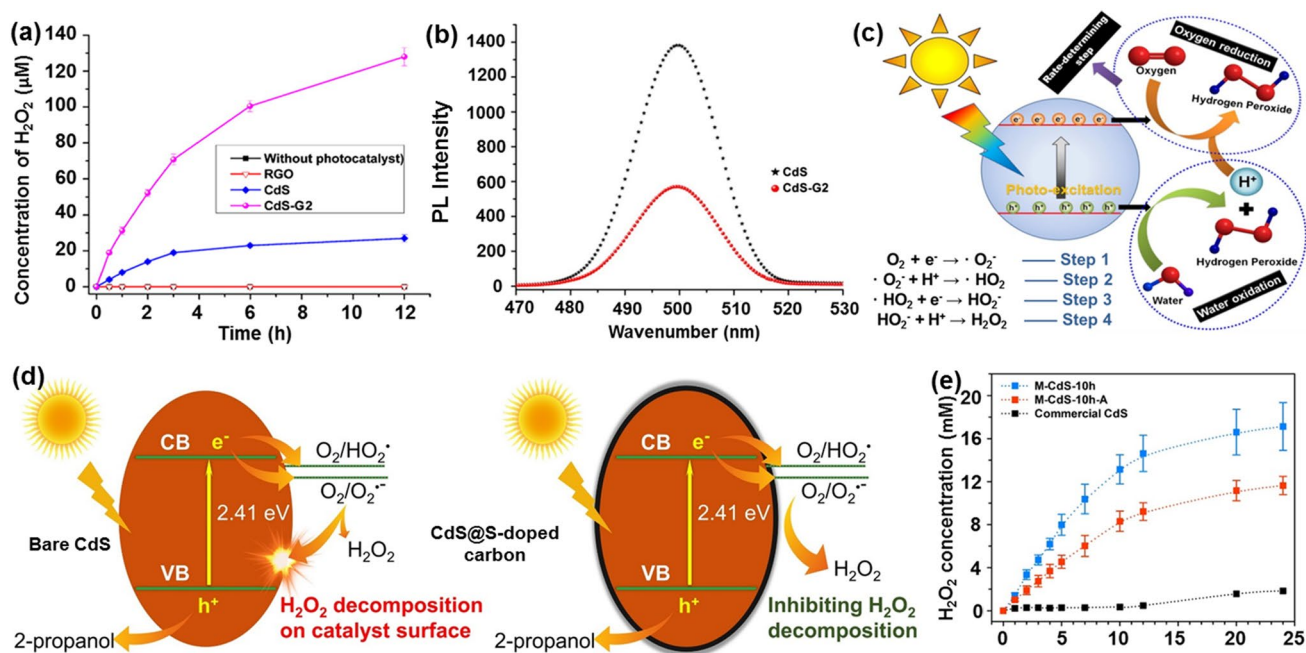
Fig. 10 **a** H_2O_2 concentration produced on different catalysts. **b** PL spectra of the CdS and CdS-G2 photocatalysts. **c** Mechanism for H_2O_2 production on the CdS-G hybrid photocatalyst under sunlight illumination. Reproduced with permission from Ref. [172]. Copyright 2016 Elsevier. Schematic illustration of H_2O_2 formation over a CdS photocatalyst and a CdS@S-doped carbon photocatalyst. **e** H_2O_2 concentration for 24 h with 20% of 2-propanol. Reproduced with permission from Ref. [174]. Copyright 2020 Elsevier

presence of sulfur-doped carbon, which can effectively hinder the H_2O_2 decomposition, as experimentally and theoretically testified (Fig. 10d). The H_2O_2 concentration generated on a nanocomposite based photocatalyst (M-CdS-10 h) reached 17.1 mM under visible light irradiation when 2-propanol was used as a sacrificial agent (Fig. 10e).

3.5 Metal–organic Frameworks Photocatalysts

Metal–organic frameworks (MOFs) own unique porous structures and strong metal–ligand interactions [175]. Similar to semiconductors, MOFs can produce electron–hole pairs upon light irradiation. They thus exhibit great potential in photocatalysis [176–179]. The Ni/MIL-125-NH$_2$, obtained via depositing NiO on the MIL-125-NH$_2$ was the

first MOF photocatalyst used in the photocatalytic H_2O_2 synthesis [180]. The mechanism of the H_2O_2 production on the Ni/MIL-125-NH$_2$ (Fig. 11a) was described as following. Nano NiO effectively inhibits the H_2O_2 decomposition through a $2e^-$ ORR pathway under visible light irradiation when benzylalcohol is accompanied as an electron donor. Specifically, MIL-125-NH$_2$ produces $Ti_8O_8(OH)_4^{\cdot-}$ and a hole upon its excitation by light irradiation. Once the hole is trapped by triethanolamine (TEOA), O_2 is reduced to $O_2^{\cdot-}$ by $Ti_8O_8(OH)_4^{\cdot-}$, followed by rapid H_2O_2 formation via the $O_2^{\cdot-}$ disproportionation reaction in the presence of NiO. Unfortunately, in this case the product was a mixture of H_2O_2 and benzaldehyde dissolved in acetonitrile. In other words, further energy-consumption for product separation and purification is required. Later, a two-phase system containing
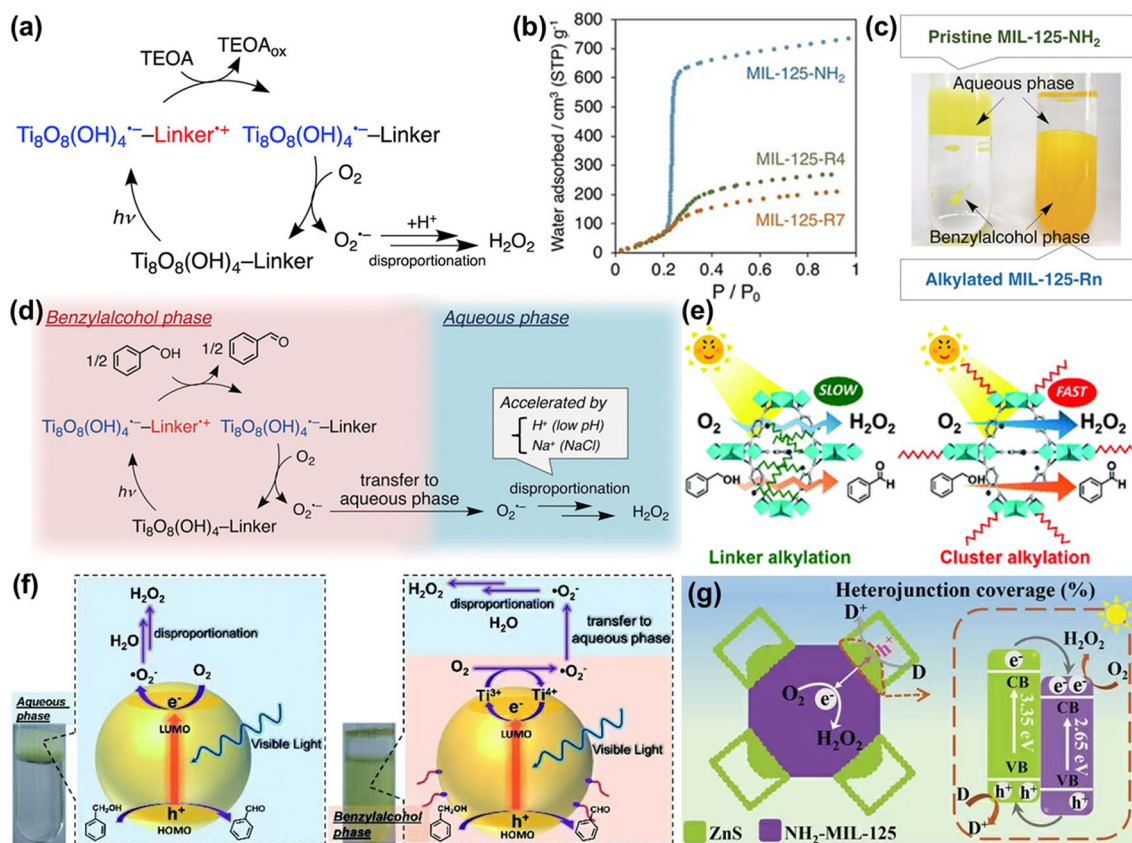

Fig. 11 **a** Photocatalytic mechanism of H_2O_2 formation on the MIL-125-NH$_2$ photocatalyst. Reproduced with permission from Ref. [180]. Copyright 2018 ROYAL SOCIETY OF CHEMISTRY. **b** Water adsorption isotherms for various catalysts. **c** Digital photographs utilizing the two-phase system. **d** Mechanism illustration of H_2O_2 generation by the two-phase system. Reproduced with permission from Ref. [181]. Copyright 2019 Wiley–VCH Verlag GmbH & Co. KGaA, Weinheim. **e** Photocatalytic processes of MIL-125-R7 and OPA/MIL-125-NH$_2$ photocatalysts. Reproduced with permission from Ref. [182]. Copyright 2019 ROYAL SOCIETY OF CHEMISTRY. **f** Mechanism of photocatalytic H_2O_2 production using the Zr$_{100}$-MOF and OPA/Zr$_{92.5}$Ti$_{7.5}$-MOF photocatalyst. Reproduced with permission from Ref. [183]. Copyright 2020 ROYAL SOCIETY OF CHEMISTRY. **g** Photocatalytic O_2 reduction to H_2O_2 over a NH$_2$-MIL-125@ZnS heterojunction. Reproduced with permission from Ref. [187]. Copyright 2021 Wiley–VCH GmbH

benzylalcohol/water (BA/water), was employed to separate these products [181]. The hydrophilic MIL-125-NH$_2$ was conversed to hydrophobic MIL-125-Rn (n = 1, 4 and 7) through the growth of the alkyl chains on the catalyst surface, as clarified using water adsorption isotherms and water contact angles measurements (Fig. 11b). A pristine MIL-125-NH$_2$ was proved to exist in the water phase during the photocatalytic H$_2$O$_2$ process, while alkylated MIL-125-Rn is located in the BA phase (Fig. 11c). During the photocatalytic H$_2$O$_2$ process (Fig. 11d), O$_2$ is firstly reduced to O$_2^{\cdot-}$ on the hydrophobic MOFs in the BA phase. Subsequently, O$_2^{\cdot-}$ is transferred to the water phase where H$_2$O$_2$ is rapidly produced through a disproportionation reaction in the presence of H$^+$ or Na$^+$. Although this two-phase system inhibited the further reaction of MOFs with H$_2$O$_2$, its photocatalytic activity of the two-phase system was not satisfying. This is because the grafting of the alkyl chains blocks the pores of the MIL-125-R7, thus greatly reducing its photocatalytic activity. In this regard, a hydrophobic MOF, namely OPA/MIL-125-NH$_2$, was developed. In this case, MIL-125-NH$_2$ retained most of its pores using octadecylphosphonic acid (OPA) treatment [182]. Its surface area was 1242 m^2 g^{-1}, comparable to that (1500 m^2 g^{-1}) of MIL-125-NH$_2$. Under visible light irradiation for 3 h, the concentration of generated H$_2$O$_2$ on this OPA/MIL-125-NH$_2$ photocatalyst was approximately 3 times larger than that of MIL-125-R7. The enhanced activity was attributed to the rapid diffusion of O$_2^{\cdot-}$ through the unblocked pores of the OPA/MIL-125-NH$_2$ photocatalyst, which prevents the H$_2$O$_2$ decomposition (Fig. 11e). A hydrophobic titanium doped zirconium-based MOF (OPA/Zr$_{100-x}$Ti$_x$-MOF) also exhibited a high rate of H$_2$O$_2$ production (9.7 mmol L^{-1} h^{-1}), where the Ti species played a role in effectively promoting electron transfer from photoexcited linkers of the MOF to Ti, inhibiting the recombination of photogenerated electron–hole pairs in the hydrophobic MOF matrix (Fig. 11f) [183].

The construction of the heterojunction by combining MOFs with other semiconductors also effectively strengthens H$_2$O$_2$ production since the separation of photogenerated electron–hole pairs can be promoted [184–186]. For example, on the MOF@MS heterostructure (NH$_2$-MIL-125@ZnS) the photocatalytic synthesis of H$_2$O$_2$ was reported via a 2e$^-$ ORR pathway (Fig. 11g) [187]. This heterostructure presents a spatially separated architecture, where ZnS nanocages are selectively adhered on the four corners of a cake-like NH$_2$-MIL-125

body. The coverage of heterojunction was controlled by altering the diameter of ZIF-8/ZnS. In this way, the regulation of the absorption of light, the generation of electron–hole pairs, the charge separation and accessibility were doable, finally leading to adjusted performance of photocatalytic H$_2$O$_2$ production. During the photocatalytic process, photogenerated electrons transfer from ZnS to NH$_2$-MIL-125, while holes migrate from NH$_2$-MIL-125 to ZnS, resulting in excellent performance. When the heterojunction coverage is ≈45.1%, the NH$_2$-MIL-125@ZnS photocatalyst displays a H$_2$O$_2$ yield of as high as 120 mM g^{-1} h^{-1}.

4 Electrocatalytic H$_2$O$_2$ Synthesis

4.1 Electrocatalytic H$_2$O$_2$ Synthesis through a 2e$^-$ ORR Pathway

2e$^-$ ORR has been considered as one of the most vital routes in electrocatalytic H$_2$O$_2$ synthesis [188, 189]. However, its selectivity is limited by the competition from the 4e$^-$ reduction pathway, namely the reduction of O$_2$ to generate H$_2$O. The fact behind is that O$_2$ has a more negative standard potential to form H$_2$O than that for the H$_2$O$_2$ generation [52, 190, 191]. Further electro-reduction of H$_2$O$_2$ to H$_2$O is thus thermodynamically favorable, which severely hinders the yield of H$_2$O$_2$ from a 2e$^-$ ORR pathway. In addition, the spontaneous H$_2$O$_2$ disproportionation to produce H$_2$O and O$_2$ prohibits the 2e$^-$ ORR pathway, lowering the selectivity of H$_2$O$_2$ production. Therefore, it is prerequisite to design electrocatalysts to promote the preferential H$_2$O$_2$ formation as well as to facilitate rapid diffusion of H$_2$O$_2$ away from the reactive interface. The reported electrocatalysts using the 2e$^-$ ORR pathway for the H$_2$O$_2$ production can be divided into two categories: noble-metal-based and carbon-based electrocatalysts. In the following session, these reported electrocatalysts are systematically classified and their performance toward the H$_2$O$_2$ is detailed (Table 3).

4.1.1 Noble Metal-based Electrocatalysts

According to Sabatier's principle, the binding energy between an OOH* radical and an electrocatalyst should be neither too strong nor too weak for efficient H$_2$O$_2$ production,

Table 3 Summary of electrocatalytic H_2O_2 production via a $2e^-$ ORR pathway

Catalyst	Electrolyte	Onset potential (V_{RHE})	Applied potential (V_{RHE})	Selectivity (%)	n	Refs.
Noble metal-based catalysts						
C(Pt)/C-3/4 h	1 M $HClO_4$	~0.7 (-0.05 mA cm^{-2})	0.1	41	3.2	[200]
Pt-SA/rGO	0.1 M KOH	0.964	0.3–0.8	~95	2–2.3	[195]
NC-Ag/NHCS	0.1 M $HClO_4$	0.82 (0.1 mA cm^{-2})	0.2–0.7	89–91	~2	[249]
Pd$^{\delta+}$-OCNT	0.1 M $HClO_4$	0.70	0.3–0.7	95–98	–	[201]
Pt/HSC	0.1 M $HClO_4$	0.71	0.1–0.7	96	2.1	[197]
Au-Pt-Ni NRs	0.1 M KOH	–	0.45–0.55	95	2.11 (0.5 V)	[250]
Carbon-based catalysts						
o-GOMC-1	0.1 M KOH	0.81	–	>90	–	[218]
HPC-H24	pH 1	–	-0.1–(-0.5)	80.9–95.0	2.10–2.38	[215]
MesoC/ MicroC	0.1 M KOH	~0.7	–	>70	~2	[217]
G-M1	0.1 M KOH	0.86	0.358	82.07	2.35	[219]
O-CNTs	0.1 M KOH	0.7 (1 mA cm^{-2})	0.4–0.65	~90	–	[22]
OCNS$_{900}$	0.1 M KOH	0.825	0.75–0.55	90 (0.7 V)	2.2–2.3	[251]
aCB	0.1 M KOH	0.821 V	0.4–0.7	>94	–	[222]
CB600	0.1 M Na_2SO_4	-0.15 $V_{Ag/AgCl}$	-0.35–(-0.6)	52.6–56.1	–	[223]
rGO$_{-KOH}$	0.1 M KOH	–	–	~100	–	[224]
GNP$_{C=O,1}$	0.5 M H_2SO_4	0.826 (0.15 mA cm^{-2})	0.75	97.8	~2	[225]
OMPC4	0.1 M KOH	–	0.42	87	2.2	[220]
HMCSs	0.1 M KOH	0.82	0.4–0.7	>95	–	[252]
g-N-CNHs	0.10 M PBS	0.53	0.45	90	2.1	[232]
	0.1 M H_2SO_4	0.40	0.3	98	2.4	
	0.1 M NaOH	0.71	0.65	63	3.2	
CG400	0.1 M KOH	0.72 (30 µA cm^{-2})	–	93	~2.1	[227]
oxo-G/$NH_3 \cdot H_2O$	0.1 M KOH	–	–	>82	–	[229]
G-COF-950	0.1 M KOH	~0.74 (0.1 mA cm^{-2})	-0.1–0.5	70–75	2.5–2.6	[228]
MNC-50	0.5 M H_2SO_4	–	0.1–0.3	>90	–	[237]
NCMK3IL50_800T	0.5 M H_2SO_4	–	0.1–0.3	95–98	2.1	[238]
N, S-MC-1	0.5 M H_2SO_4	0.318 V_{SHE}	0.06 V_{SHE}	76	2.5	[230]
N-doped porous carbon	0.5 M H_2SO_4	0.49 (0.01 mA cm^{-2})	0.35	98.5	–	[253]
	0.1 M KOH	0.84		83	–	
HNCS	0.1 M KOH	–	0.7	~91.9%	–	[254]
HPCS-S	0.1 M KOH	0.77 (0.1 mA cm^{-2})	0.3–0.7	70	2.7	[240]
BN-C1	0.1 M KOH	0.80 (0.5 mA cm^{-2})	–	90	–	[241]
EDTAFeNa-KB-HT1	0.1 M KOH	0.857	0.60–0.75	80–100	2.0–2.4	[242]
Co–N-C	0.5 M H_2SO_4	0.83 (0.01 mA cm^{-2})	0.1	80	~2.4	[247]
Mn–O/N@NCs-50	0.1 M $HClO_4$	–	0.5	87	2.5	[243]
Co$_1$-NG(O)	0.1 M KOH	~0.8	–	~82	–	[248]

Table 3 (continued)

Catalyst	Electrolyte	Onset potential (V_{RHE})	Applied potential (V_{RHE})	Selectivity (%)	n	Refs.
Co–N–C	0.1 M $HClO_4$	0.74	–	~87	–	[244]
Mn–N–C		0.63	–	~50	–	
Fe–N–C		0.81	–	~30	–	
Co-N_2-C/HO	0.1 M KOH	0.801 (0.15 mA cm^{-2})	0.7	91.3	2.3	[255]
CDs (Glucose in 1L)	0.1 M KOH	0.68	0.7–0.3	95	2.05	[256]
CMK3-20 s	0.1 M KOH	0.79	0.25–0.75	88–91	–	[212]
	0.1 M K_2SO_4	0.46	0.15–0.4	51–75	–	

since an OOH* radical is the only intermediate in the process of a 2e$^-$ ORR pathway [41]. Meanwhile, the integrity of an O–O bond must be well maintained during the conversion process since the splitting of O–O bond is conductive to form water. It has to highlight here that the manners of oxygen adsorption on a catalyst mainly follow three modes (Fig. 12a), namely Pauling model ("end-on"), Griffiths model and Bridge model ("side-on") [55, 192]. Only Pauling model is beneficial for the H_2O_2 generation via two-electron reduction of O_2. This is due to its low influence on the O–O bond splitting. Differently, other two models induce the O–O bond splitting and facilitate the 4e$^-$ ORR pathway. Note that it is more thermodynamically inclined to the pathway of the 4e$^-$ ORR to form H_2O in comparison with H_2O_2 generation via the 2e$^-$ ORR pathway. To address this issue, the key is to design and synthesize advanced catalysts with high activity for O_2 reduction, while well remaining O–O bond during the 2e$^-$ ORR process. In the next section, the electrocatalysts on the selective reduction of O_2 to H_2O_2 are reviewed in combination with some typical examples.

Single noble metal materials have been applied for electrocatalytic H_2O_2 synthesis. For example, DFT calculations have been firstly used to reveal the relationship between the ORR activity and various metallic catalysts. The Sabatier volcano plots were then established (Fig. 12b), namely the electrocatalytic ORR activity of different metals and metal-nitrogen/carbon (M–N/C) [193]. Taking the volcano curves of single metals (the left-hand side of the volcano diagram) as the example, the limiting potential of a 4e$^-$ ORR process is more positive than that of a 2e$^-$ ORR process, thermodynamically indicating that the 4e$^-$ reduction reaction is more likely to occur to obtain H_2O than the 2e$^-$ reduction reaction to generate H_2O_2. While on the right-hand side of the volcano plots, the limiting potential of 2e$^-$ and 4e$^-$ ORR processes are located at the same position, which illustrates that they simultaneously take place to produce H_2O_2 and H_2O, respectively. In more detail, as the cases that the strong interaction occurs between metals and O_2 molecules, the selectivity of 2e$^-$ ORR can be improved once the metal surface is modified, or its structure is regulated. Taking Pt metal as an example, O_2 is adsorbed on the Pt surface mainly through a "side-on" mechanism, instead of the "end-on" mechanism. The H_2O_2 production on Pt catalysts is thus not conducive to be promoted [194]. In literature, the effects of the size and morphology of metal catalysts have been extensively investigated to explore the activity for electrocatalytic H_2O_2 production, namely via altering the O_2 adsorption mode on the Pt electrocatalysts [195–197]. Note that the choice of suitable supports also modulates the selectivity of the Pt electrocatalysts toward electrocatalytic H_2O_2 production [198, 199]. For example, an amorphous carbon layer coated Pt catalyst was prepared by use of a chemical vapor deposition method with acetylene as the precursor [200]. This amorphous carbon layer presumably produces steric hindrance on the Pt surface, which induces O_2 to be adsorbed through the end-on configuration, instead of side on configuration over the pristine Pt/C electrocatalyst (Fig. 12c). The 2e$^-$ ORR pathway happened dominantly on the C(Pt)/C-3 h and C(Pt)/C-4 h electrocatalysts. Their H_2O_2 selectivity reached 41% at a potential of 0.1 V_{RHE}. Similarly, sulfur-doped carbon using zeolite-templated was used to support catalyst, where this carbon material supported and dispersed 5 wt% Pt atoms [197]. This Pt atomic electrocatalyst followed a 2e$^-$ ORR pathway. Its H_2O_2 selectivity was as high as 96%. Modified Pd species have been also designed and obtained to assess selective ORR [201,
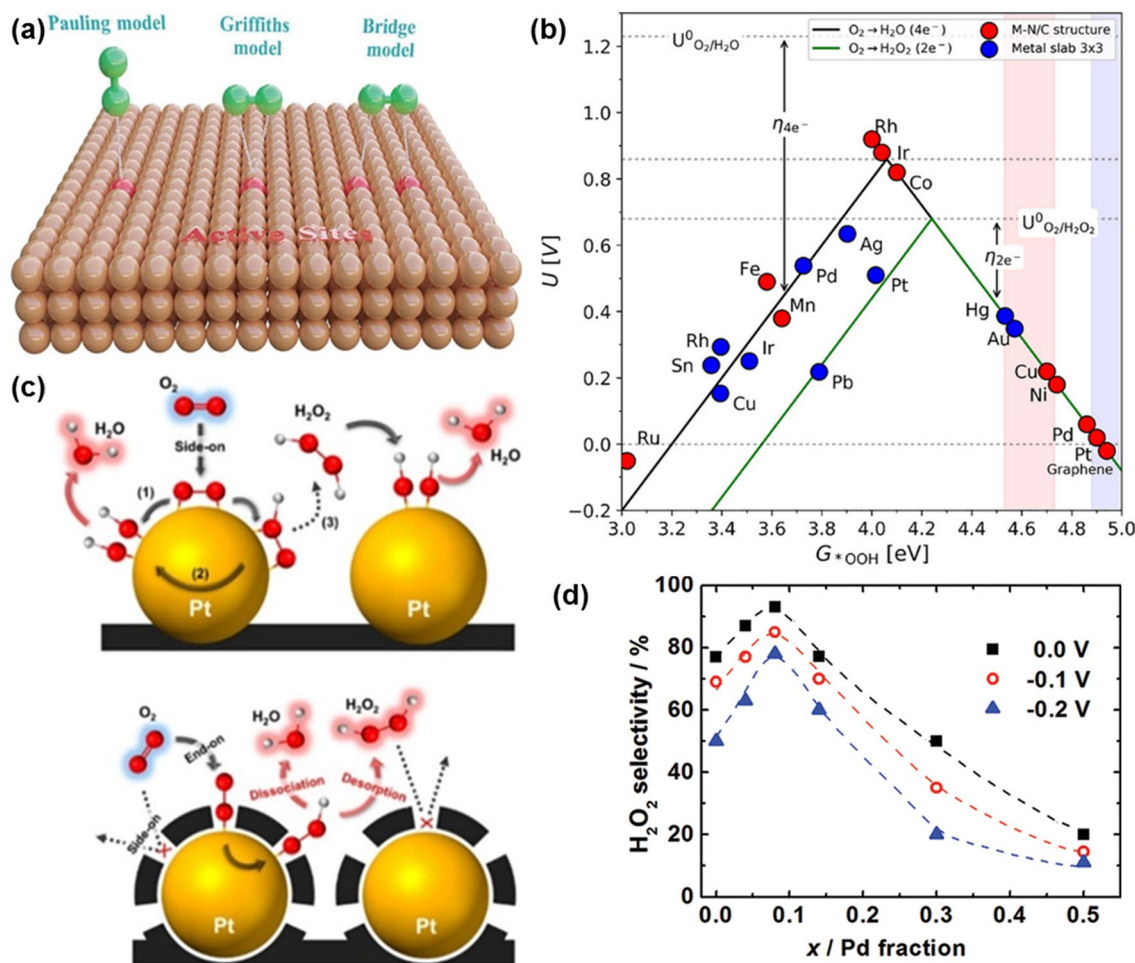
Fig. 12 a Three typical modes for O_2 adsorption. Reproduced with permission from Ref. [192]. Copyright 2021 Elsevier. **b** Sabatier volcano plots for electrochemical ORR for pure metal slabs and M–N/C. Reproduced with permission from Ref. [193]. Copyright 2018 American Chemical Society. **c** Proposed ORR pathways on the pristine Pt/C and carbon-coated Pt electrocatalysts. Reproduced with permission from Ref. [200]. Copyright 2014 American Chemical Society. **d** H_2O_2 selectivity of the $Au_{1-x}Pd_x$ electrocatalyst with different palladium contents at potentials of 0, -0.1 and -0.2 V. Reproduced with permission from Ref. [208]. Copyright 2011 American Chemical Society

202]. For instance, using a nano-Pd electrocatalyst, obtained through *in-situ* electrochemical deposition from Pd ions, high selectivity for the 2e$^-$ ORR pathway to form H_2O_2 was achieved. Even when Pd is derived from the lowest precursor concentration, related nano-Pd electrocatalyst exhibited high selectivity, which was surpassed 95% [203].

In contrast, the noble metals (e.g., Au) that possess weak adsorption capability toward O_2 molecules have been applied to reduce O_2 for efficient, selective and stable H_2O_2 production [204–206]. Unfortunately, the adsorption of O_2 molecules on the crystal plane of noble metals is different. Namely, the ORR pathway on different metal facets is different. For example, the too weak bond between an Au

(111) surface and O_2 molecules makes it difficult to form the OOH* intermediate [207]. The H_2O_2 production on the Au (111) surface via the 2e$^-$ ORR pathway exhibits a low efficiency and high energy consumption is associated. In this regard, the crystal plane of noble metals is applied as the reactive interface, since its binding energy with O_2 molecule in a high index crystal plane is stronger than that occurred in an (111) facet. For example, an Au (211) facet effectively promotes the activity of a 2e$^-$ ORR pathway for the H_2O_2 production.

Although the H_2O_2 selectivity of single metal electrocatalysts can be effectively adjusted via various means as discussed above, simultaneous improvement of the

activity and selectivity for the 2e⁻ ORR pathway on single metal electrocatalysts is still challenging. This is mainly originated from the fact those with weaker interactions with O_2 often need high overpotential to boost the 2e⁻ ORR, while those owning stronger interactions with O_2 are prone to bring the direct the 4e⁻ ORR. Combining such metals (namely those weakly interact with O_2 and those strongly interact with O_2) to form metal alloys is thus a potential strategy to facilitate both activity and selectivity of metal electrocatalysts toward the H_2O_2 generation. For example, the $Au_{1-x}Pd_x$ nanoalloys supported on Vulcan XC-72 exhibited the superior selectivity toward the H_2O_2 production (nearly 95%) when the Pd content in the alloy arrived at 8%, surpassing that using single Au and Pd metal electrocatalysts (Fig. 12d) [208]. The Pd monomer surrounded by Au atoms on the Au–Pd nanoalloy surface was suggested to promote the H_2O_2 formation via an "end-on" O_2 adsorption model. When the percentage of Pd was increased to 15%, the selectivity of the H_2O_2 generation was decreased. This is because the presence of continuous Pd atoms (e.g., two adjacent Pd atoms) altered the O_2 adsorption model and facilitated the H_2O formation. In a theoretical work, the tactics was provided based on DFT calculations to screen for metal alloy electrocatalysts that feature excellent activity toward electrocatalytic H_2O_2 production [5]. These metal alloys are prepared by surrounding individual elements (e.g., Pt, Ir, Pd, Rh and Ru) that are active for the ORR by inert metallic elements (e.g., Hg and Au). Since the active elements exhibit strong adsorption toward O_2 molecule, these metal alloys can effectively reduce O_2 to OOH*. On the other side, they do not break the O–O bond, because of their difficulty in dissociating OOH* in combination with the neighboring inert sites. In short, the activity and selectivity of metal alloy catalysts toward the 2e⁻ ORR can be regulated by using the advantages of the isolated active sites. Theoretical models have even predicted that the isolated active site of the Pt-Hg alloy can effectively activate O_2 molecules and boost the H_2O_2 synthesis. Experimentally, several Hg-based bimetallic alloys have shown high activity and selectivity for the H_2O_2 production [209]. Among them, the Pd-Hg alloy exhibited the highest current for the H_2O_2 production at the same overpotential, as predicted from the DFT calculations. In more detail, the activities of Pt-Hg, Ag and Ag-Hg alloys are one order of magnitude higher than that of individual Au electrocatalyst, while the activity of a Pd-Hg alloy is two orders of magnitude higher than that of

individual Au electrocatalyst. The AuPd alloy nanoparticles have been used to disclose the relationship between the activity of electrocatalytic H_2O_2 production and molar ratio of Au to Pd. Modulating the composition of alloy catalysts is thus recognized as a new way to promote the 2e⁻ ORR for electrocatalytic H_2O_2 production [210].

4.1.2 Carbon-based Electrocatalysts

It is clear that the noble metals and their alloys feature high activity and selectivity for electrocatalytic H_2O_2 synthesis via the 2e⁻ ORR pathway. Unfortunately, they are expensive and scarce, hindering their large-scale applications. Many advanced electrocatalysts with reduced costs have been thus explored for electrocatalytic H_2O_2 synthesis. Carbon-based electrocatalysts have been considered to be one of the most promising substitutes of noble metal-based catalysts. This is due to their unique surface and structural properties, abundant availability and low cost for their synthesis [211–214]. Note that the pristine carbon materials only exhibit low catalytic activity for the 2e⁻ ORR, thus the reconstruction of carbon materials or their surface modification (Fig. 13) have been developed to optimize their electronic properties for electrocatalytic H_2O_2 generation [18]. The widely reported approaches include manufacturing porous structures and defects, heteroatom doping and surface (oxygen) functionalization are provided.

Among diverse carbon materials, porous and defective carbon materials are highly suitable for the 2e⁻ ORR. This is due to their unique advantages, such as their high surface areas, tunable porosities and high electronic conductivities.
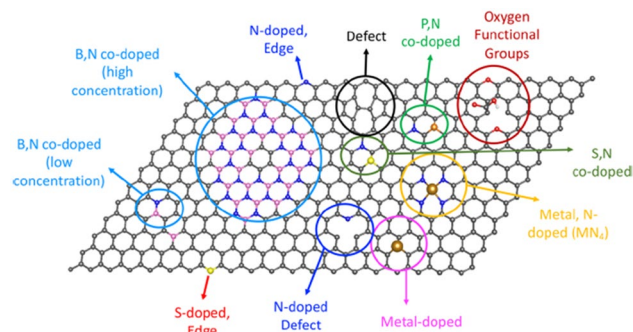

Fig. 13 Schematic demonstration of tuning electronic structures of carbon electrocatalysts for electrocatalytic H_2O_2 production via the 2e⁻ ORR pathway. Reproduced with permission from Ref. [18]. Copyright 2020 American Chemical Society

It has been widely recognized that carbon electrocatalysts with a porous structure can provide abundant active sites and shorten diffusion distance for the reactive species, producing positive contributions for their electrocatalytic H_2O_2 generation. For example, various hierarchically porous carbon (HPC), produced by hydrothermal treatment and subsequent carbonization, have been applied for selective H_2O_2 formation (Fig. 14a) [215]. The HPC-H24 (hydrothermal treatment for 24 h and carbonization under H_2) exhibited the most positive peak potential and the highest selectivity for the $2e^-$ ORR, namely the best performance of selective H_2O_2 formation. The remarkable electrocatalytic performance of HPC-H24 was assumed to be originated from high contents of active sites (e.g., sp^3-C bonds, vacancy defects and edge defects), more exposed and accessible active sites and fast mass transport of H_2O_2 inside a porous structure. On the

contrary, it was acknowledged that edge-rich graphene presented the typical $4e^-$ ORR mechanism [216]. Later, two different types of porous carbon, namely microporous carbon (denoted as MicroC) and mesoporous carbon (denoted as MesoC) have been developed toward the H_2O_2 production in alkaline conditions (Fig. 14b) [217]. From the broad π^* resonance of near-edge X-ray absorption fine structure (NEXAFS) spectra, the conclusion that both MicroC and MesoC have a larger number of sp^2 carbon defective sites than HOPG has been drawn. Electrochemical experiments suggested that both MicroC and MesoC had superior activity and selectivity for the $2e^-$ ORR, where the onset potential was very close to the thermodynamic equilibrium potential (0.7 V_{RHE}), and the selectivity of the H_2O_2 production even outperformed 70% in some cases (Fig. 14c). In addition, DFT calculations have illustrated the sp^2-type defects are

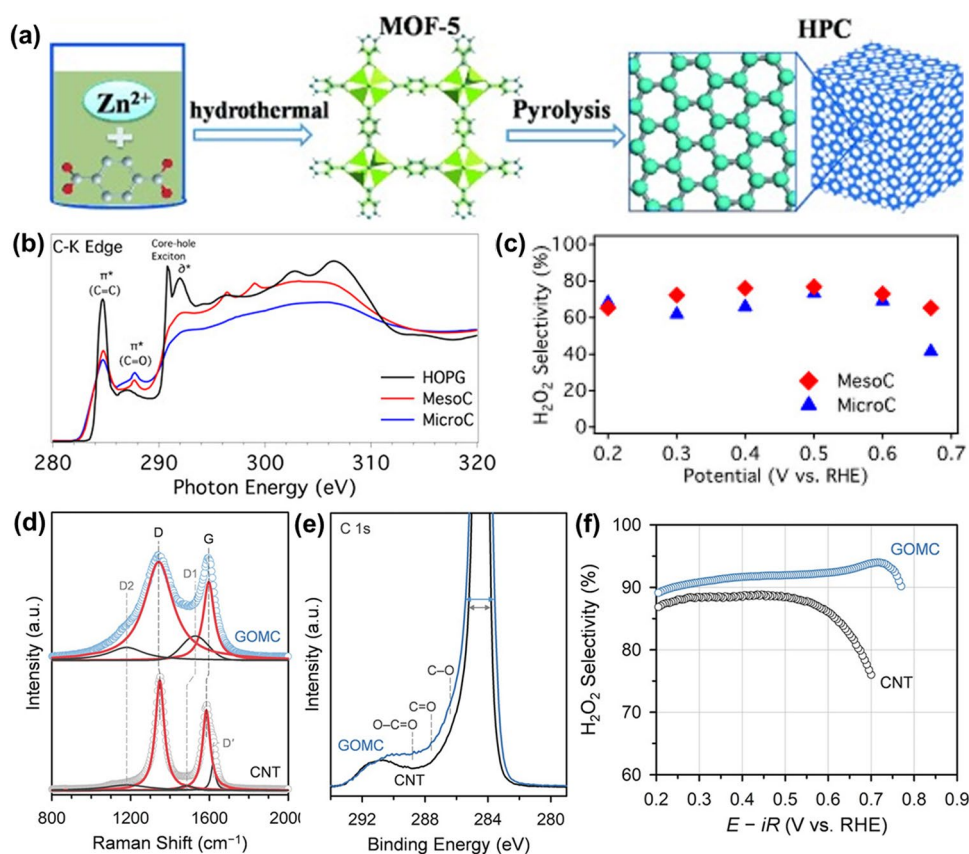**Fig. 14 a** Schematic illustration of the synthetic route to HPC. Reproduced with permission from Ref. [215]. Copyright 2015 Wiley–VCH Verlag GmbH & Co. KGaA, Weinheim. **b** NEXAFS spectra of the C-K edge in HOPG, MesoC and MicroC. **c** H_2O_2 selectivity of the MesoC and MicroC electrocatalysts. Reproduced with permission from Ref. [217]. Copyright 2018 American Chemical Society. **d** Raman spectra, **e** C 1s XPS spectra and **f** H_2O_2 selectivity of GOMC and CNT. Reproduced with permission from Ref. [218]. Copyright 2019 Wiley–VCH Verlag GmbH & Co. KGaA, Weinheim

the active sites for O_2 reduction, which is beneficial for the H_2O_2 generation. Similar optimization of defects and pore size in carbon materials have been reported for electrocatalytic H_2O_2 production. For example, the graphitic carbon with rich edge sites has been applied as an electrocatalyst to promote the H_2O_2 synthesis. Its activity was about 28 times higher than that of a basal plane-rich carbon nanotube (CNT) [218]. This enhanced activity was explained by the fact that graphitic ordered mesoporous carbon (GOMC) has a larger portion of defective carbon and reaction sites (sp^2-C) when compared with CNT. Such a statement was solidly supported from the experimental results by means of Raman spectroscopy (Fig. 14d) and XPS (Fig. 14e) characterization. Compared with CNTs, the GOMC showed the H_2O_2 selectivity higher than 90% via the 2e⁻ ORR pathway and excellent stability (e.g., 90% of the initial current is retained) (Fig. 14f).

It has been reported that oxygen-containing groups play an important role on the activity and selectivity of carbon catalysts toward the 2e⁻ ORR [219–225]. For instance, oxygen-doped microporous polypyrene carbons (OMPC) exhibited the enhanced activity and selectivity for electrocatalytic H_2O_2 generation [220]. In basic electrolyte, the OMPC4 (oxygen content is 6.52 at%) showed obviously stronger ability to H_2O_2 production from the I_{ring} than MPC, as well as the higher limited oxygen reduction current (I_{disk}) (Fig. 15a). Meanwhile, the selectivity of the H_2O_2 production on OMPC-4 was remarkably increased (e.g., from 40 to 87% at 0.42 V_{RHE}) and the calculated electron transfer number (n) was close to 2 through oxygen doping on OMPC (Fig. 15b). In addition, the selectivity of MPC with the different oxygen content is displayed in Fig. 15c, where OMPC-4 exhibited the highest value. In another case, oxygenated carbon (namely activated carbon black, denoted as aCB) electrocatalyst showed higher ORR activity meaning the stronger capacity of H_2O_2 generation than CB (Fig. 15d) [222]. The selectivity above 94% was obtained on the aCB catalyst in the potential range from 0.4 to 0.7 V as depicted in Fig. 15e. The DFT calculations further disclosed the activity difference of these oxygen-containing groups toward the H_2O_2 production (Fig. 15f) is originated from the fact that C–O–C and -CHO are the most active sites toward the H_2O_2 synthesis compared to other functional groups.

In addition to structured carbon materials, heteroatom (e.g., N, S, B) doped carbon materials have been widely studied for the electrocatalytic H_2O_2 production via the 2e⁻ ORR pathway [226–230]. Many studies have confirmed that N-doping of a carbon material can effectively promote the catalytic performance for the ORR, because the higher electronegativity of N atoms than carbon atoms can activate π electrons in carbon system. The charge redistribution is then induced or the electronic properties of carbon materials are changed, leading to varied adsorption capacity of carbon catalysts toward O_2 and generated intermediates [55, 231, 232]. It must be pointed out that common N-doped carbon catalysts are conducive to the 4e⁻ ORR pathway to produce water [233–235]. It is thus extremely important to bridge the relationship of a nano-structured carbon catalyst and the content of doped N inside with the ORR selectivity. For example, a simple hard-templating strategy was adopted to obtain mesoporous nitrogen-doped carbon (meso-BMP-800) catalyst and its nitrogen content was 14.2 wt% (as determined from XPS analysis) or 17.17 wt% (as evaluated from elemental analysis) [236]. On this electrocatalyst, selective H_2O_2 production was enhanced (Fig. 16a)**. This 2e⁻ ORR process has been experimentally and theoretically doable. In such situations, the strategy of N-doping of carbon materials helped to achieve high conductivities of carbon materials and their high selectivity for electrocatalytic H_2O_2 production. It is so-called a pure two-electron mechanism. However, the regulatory mechanism of the structure of a carbon catalyst on its reactivity is still unclear. In this context, the effect of porous structures of carbon catalysts on their catalytic properties toward the H_2O_2 production has been explored [237]. Mesoporous nitrogen-doped carbon (MNC) exhibited higher H_2O_2 selectivity (> 90%, Fig. 16b) than activated nitrogen-doped carbon (ANC). Enhanced mass transport into a mesoporous structure of this catalyst was suggested to be responsible for such high H_2O_2 selectivity of MNC (Fig. 16c). Later, systematic studies have been explored to reveal the correlations between the performance of electrocatalytic H_2O_2 production on carbon catalysts and their structural characters and surface physicochemical properties [238]. The selectivity of the H_2O_2 production on N-doped carbon catalysts is more dependent on the nitrogen doping effect rather than zeta potentials and defect sites of used carbon catalysts. In other words, the tuning of N-doping in carbon materials is very important and even more critical than structuring of carbon materials to obtain the high performance for electrocatalytic H_2O_2 production. In addition to N-doped carbon materials, B/S-doped ones were synthesized for electrocatalytic H_2O_2 generation.
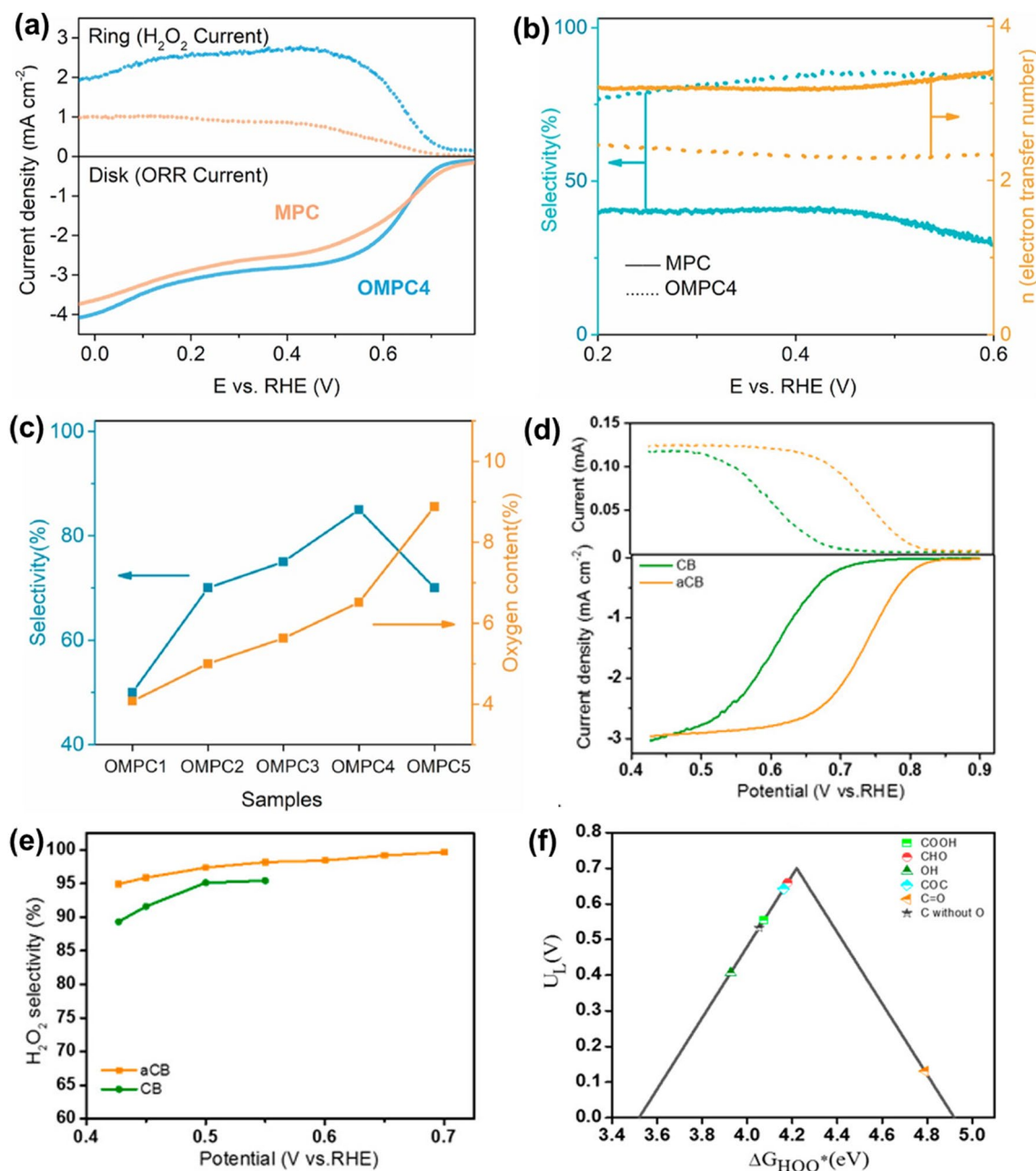
Fig. 15 **a** ORR performance, **b** selectivity and electron transfer number of OMPC4 and MPC in O_2-saturated 0.1 M KOH. **c** Relationship between the selectivity and oxygen content of various OMPC-samples. Reproduced with permission from Ref. [220]. Copyright 2020 Elsevier. **d** ORR performance and **e** selectivity of aCB and CB in 0.1 M O_2-saturated KOH. **f** Activity volcano plot of the 2e⁻ ORR. Reproduced with permission from Ref. [222]. Copyright 2018 American Chemical Society

For example, B-doped mesoporous carbon materials have been synthesized via a convenient hydrothermal method, where F127 and boric acid were the template and boron source, respectively [239]. The obtained B-MC-F2 exhibited enhanced performance for electrocatalytic H_2O_2 formation

in alkaline solution. In another case, a hollow, porous and S-doped carbon spheres presented higher activity and selectivity (> 70%) via the 2e⁻ ORR pathway than carbon spheres without S-doping. The introduced S–S bond is believed to feature low overpotential for the 2e⁻ ORR, leading to high
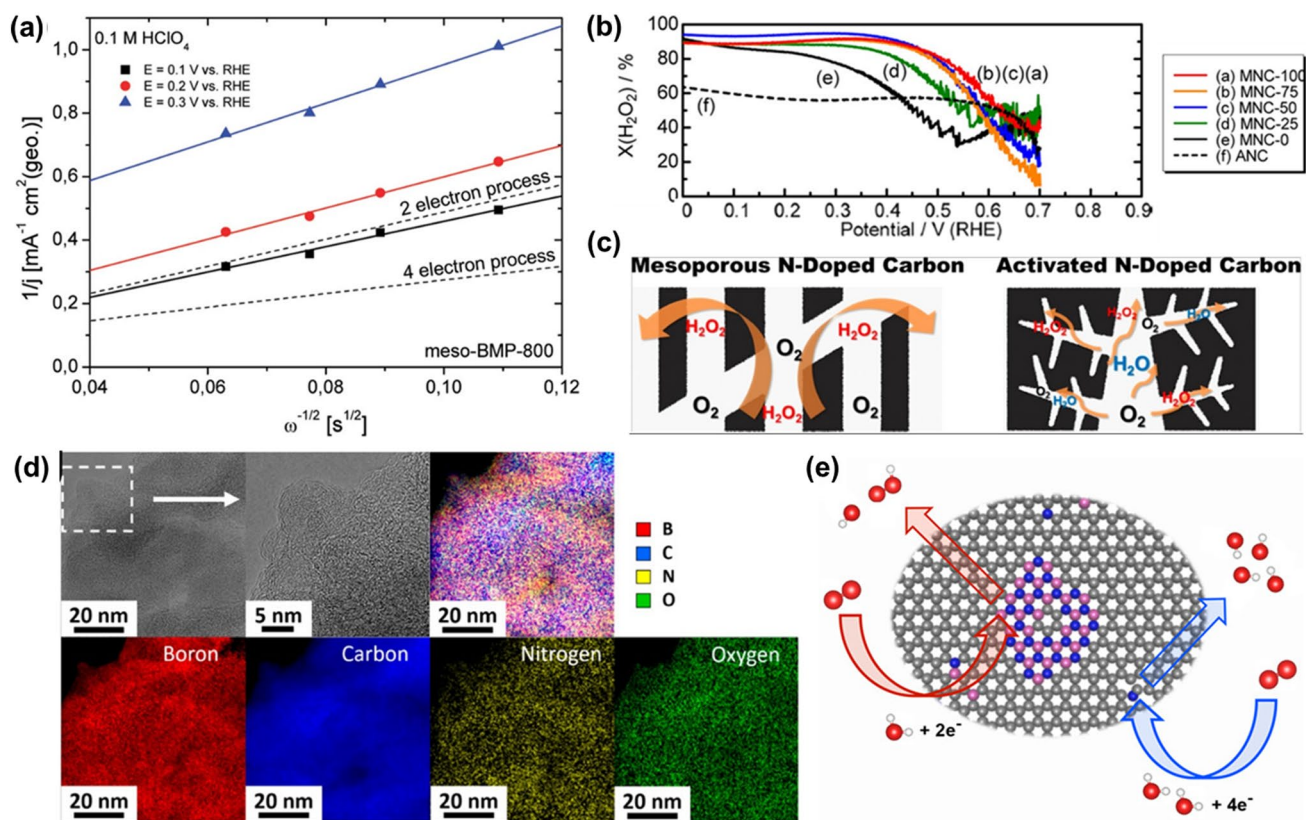
Fig. 16 **a** The number of electrons transferred based on the Koutecky–Levich plot. Reproduced with permission from Ref. [236]. Copyright 2012 American Chemical Society. **b** RRDE voltammograms toward ORR over the MNCs and ANC. **c** Schematic illustration of the ORR on different N-doped carbon. Reproduced with permission from Ref. [237]. Copyright 2014 American Chemical Society. **d** HRTEM and elemental mapping images of BN-C1. **e** Schematic illustration of the types of doping motifs and ORR mechanisms on these active sites in the B,N co-doped electrocatalysts (C: gray, N: blue, B: red; O: white). Reproduced with permission from Ref. [241]. Copyright 2018 American Chemical Society

activity for electrocatalytic H_2O_2 production [240]. In addition to the monoatomic-doped carbon materials, multiple heteroatoms co-doped carbon materials have been utilized for electrocatalytic H_2O_2 generation. For example, B,N codoped (BN-C) carbon materials prepared through a simple heat-treatment (Fig. 16d) showed higher activity and selectivity for the H_2O_2 production via the 2e$^-$ ORR pathway than the N-doped carbon materials [241]. Once again, there are various facts (e.g., heteroatom doping) affect the 2e$^-$ and 4e$^-$ pathways on carbon materials (Fig. 16e). However, the H_2O_2 formation on B,N-doped carbon materials was preferentially driven by 2e$^-$ ORR pathway, resulting from unique catalytic behavior at the interface of h-BN domains and the host graphene lattice.

As an interesting type of electrocatalysts, N-doped carbon materials with atomically dispersed transition metals (M–N-C) have been paid close attention in recent years for various

catalytic applications, especially as unique catalytic systems for the selective H_2O_2 production via the 2e$^-$ ORR pathway [242–245]. For example, the relation between physicochemical properties of transition metal (e.g., Mn, Fe, Co, Ni and Cu) single-atom anchored in N-doped graphene and their performance of electrocatalytic H_2O_2 production has been systematically explored by the means of theoretical calculations and experimental tools [246]. The DFT calculations indicated that the intermediates of $^*OOH$, $^*O$ and $^*OH$ that are adsorbed on the top site of the metal (M) atoms are the most stable configurations. According to related activity-volcano plot (Fig. 17a), Ni and Cu single-atom catalysts (SACs) tend to follow the 2e$^-$ ORR pathway during O_2 reduction, suggesting their high selectivity toward the H_2O_2 generation. On the other side, a large barrier exists between the reduction of $^*OOH$ and the activation of O_2 molecule. A large overpotential for the ORR is thus indispensable, suggesting low activity of these SACs
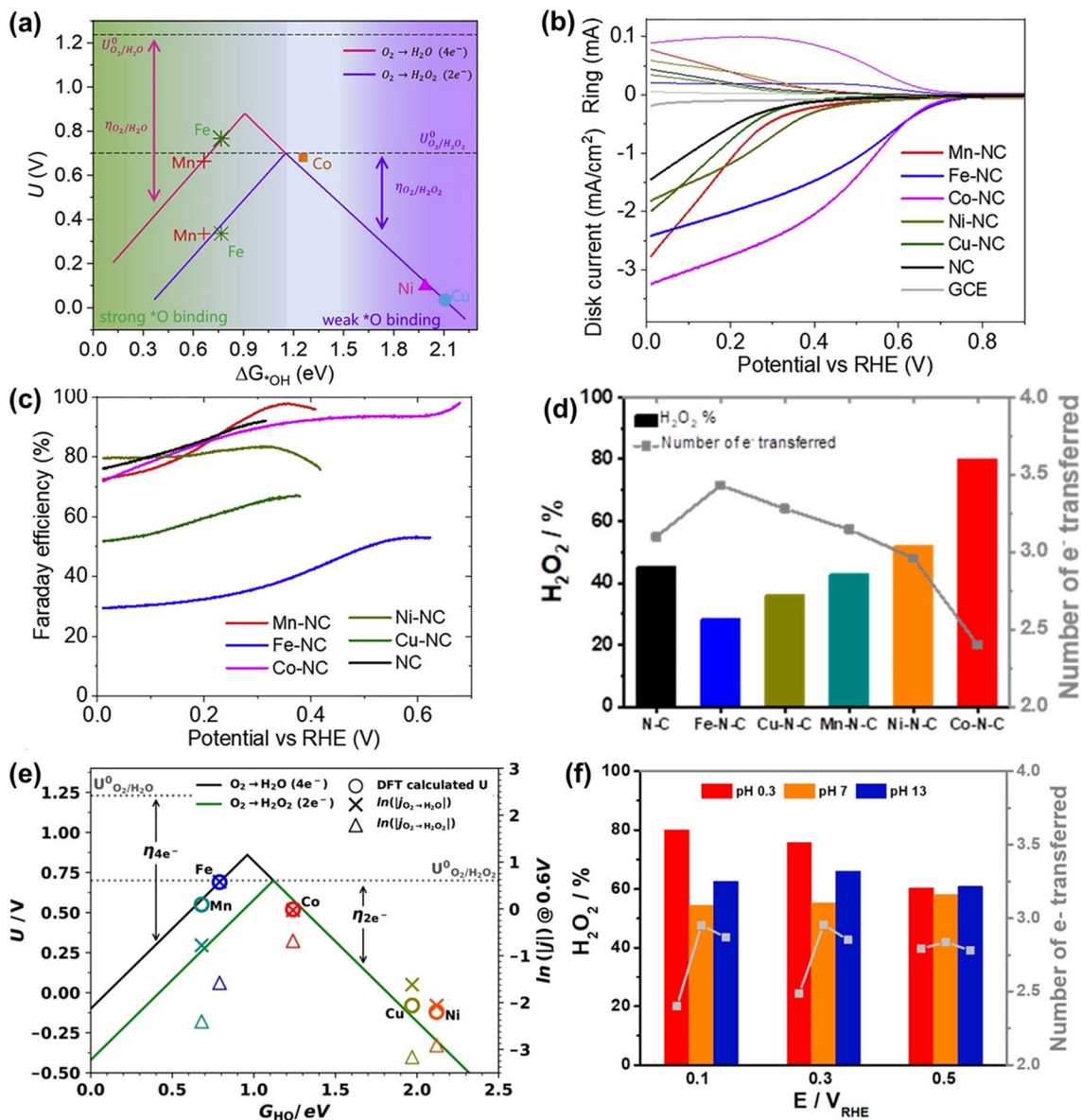
Fig. 17 **a** Activity-volcano plot of ORR through 2e$^-$ or 4e$^-$ route. **b** Linear sweep voltammograms (LSVs) of various catalysts in O$_2$-saturated 0.1 M HClO$_4$. **c** Faradic efficiencies of the H$_2$O$_2$ formation at different potentials. Reproduced with permission from Ref. [246]. Copyright 2019 Elsevier. **d** H$_2$O$_2$ selectivity and the number of electrons transferred (n) at +0.1 V$_{RHE}$. **e** Activity-volcano plot for the ORR. **f** H$_2$O$_2$ selectivity and the number of electrons transferred (n) at different potentials. Reproduced with permission from Ref. [247]. Copyright 2019 American Chemical Society

for electrocatalytic H$_2$O$_2$ production. Differently, the 4e$^-$ ORR pathway becomes more favorable on the Mn and Fe SACs during the ORR, resulting in poor selectivity for electrocatalytic H$_2$O$_2$ production. Remarkably, only Co SACs exhibit optimal d-band centers near the apex of the volcano plots, indicated the appropriate adsorption for the intermediates to facilitate the 2e$^-$ ORR pathway. Its high activity and selectivity for the

2e$^-$ ORR were confirmed by electrochemical ORR tests, where this Co-NC catalyst showed high activity and selectivity for the H$_2$O$_2$ production in acidic media (Fig. 17b, c). Similarly, the activity and selectivity of M–N–C (M=Mn, Fe, Co, Ni and Cu) SACs for electrocatalytic H$_2$O$_2$ production have been investigated [247]. Among these catalysts, the Co–N–C catalyst exhibited the highest ORR selectivity (80%) at 0.1 V$_{RHE}$ in 0.5 M

H_2SO_4 than that of Fe–N–C (28%), Cu–N–C (36%), Mn–N–C (43%), N–C (45%) and Ni–N–C (52%) catalysts under the same conditions. Such high performance was assigned to the fact that the binding free energy of Co–N–C is close to that at the top of the H_2O_2 production in the volcano plot (Fig. 17e). The number of electrons transferred of a Co–N–C catalyst was much closer to 2 (Fig. 17d). This result indicates that the Co–N–C catalyst is more favorable for 2e⁻ ORR pathway to produce H_2O_2 (Fig. 17f). The H_2O_2 selectivity of a Co–N–C catalyst is increased with the potential decreased in acidic solutions, while remained well in the whole potential range under neutral and alkaline electrolyte. One optimal Co–N_4 moiety incorporated in N-doped graphene exhibited excellent H_2O_2 productivity and durability [248]. In the volcano plot of ORR activity, none of M-N_4/graphene catalysts are located at the peak position ($\Delta G_{OOH*} = 4.2$ eV) for the H_2O_2 production. As for the Co-N_4, its ΔG_{OOH*} can be modulated once functional groups are attached. For example, when one O* is adsorbed near the Co-N_4 moiety (denoted as Co–N_4(O)), the ΔG_{OOH*} value increases from 3.9 to 4.1 eV, very close to the optimal ΔG value for the H_2O_2 production. This phenomenon can be clarified according to the difference in the charge states of cobalt atoms. Specifically, the charge states of cobalt atoms in the Co–N_4(O) and Co–N_4(2O) moieties are 0.05 e⁻ and 0.10 e⁻ more positive than Co–N_4. Therefore, a reasonable design strategy of electrocatalytic H_2O_2 synthesis is to slightly enlarge ΔG_{OOH*} value of the Co–N_4/graphene electrocatalyst by constructing electron-rich oxygen species near the Co–N_4 moiety. In this way, the charge states of cobalt atoms are thus gently increased. With aid of this strategy, the Co₁-NG(O) SAC were prepared. Among them, the Co₁-NG(O) catalyst showed excellent activity and high selectivity for electrocatalytic H_2O_2 generation.

4.2 Electrocatalytic H_2O_2 Synthesis Through a 2e⁻ WOR Pathway

In addition to the 2e⁻ ORR pathway, the 2e⁻ WOR has been considered as another promising approach toward electrocatalytic H_2O_2 production. It is worth mentioning that in a 2e⁻ WOR process only H_2O is involved as the reactant for the electrocatalytic H_2O_2 production. Such systems are thus more convenient to be operated than those using the 2e⁻ ORR pathway. However, the H_2O_2 generation via the 2e⁻ WOR pathway usually displays relatively low Faradaic efficiency. This is because the competitive 4e⁻ WOR

(namely O_2 evolution process) is thermodynamically more favorable than the 2e⁻ WOR (namely the H_2O_2 formation) accompanying with the autocatalytic decomposition from H_2O_2 into O_2. In this regard, there are limited studies on this infant field.

4.2.1 Metal Oxides

Noble metal oxides (e.g., RuO_2 and IrO_2) have been frequently applied for various catalytic applications, due to their high catalytic activities and long-term stability at high potentials [257, 258]. However, their prices are high to limit the large-scale applications [259]. Many alternative noble-free metal oxides thus became more popular in the H_2O_2 production via the 2e⁻ WOR pathway (Table 4). For example, the free energies of OH* and O* were identified as key parameters to confirm selectivity and activity of different electrocatalysts toward the 2e⁻ WOR [260]. The metal oxide catalysts that simultaneously meet two conditions for OH* and O* binding energies ($\Delta G_O \gtrsim 3.5$ eV and $\Delta G_{OH} \lesssim 2.4$ eV) are favorable for selective H_2O_2 production [261]. In the summarized relationship between the selectivity of 2e⁻ WOR and the binding energies of O/OH for a number of different metal oxides (Fig. 18a), metal oxides (e.g., WO_3, $BiVO_4$, MnO_2 and SnO_2) are located in the region for weak O adsorption energies (green region). They thus promote the 2e⁻ WOR to form H_2O_2. In verse, metal oxides (e.g., IrO_2, RhO_2 and PtO_2) that feature strong O adsorption energies (blue region) are favorable to generate O_2 as the major product. This study provides a good theoretical guide to rationally design metal oxide catalysts in the process of 2e⁻ WOR to promote the H_2O_2 production. Meanwhile, the activity trends of various metal oxides (e.g., WO_3, ZnO, $CaSnO_3$, $BiVO_4$, SnO_2 and TiO_2) for the H_2O_2 production via the WOR pathway were summarized as the activity volcano plots. They were based on the relationship between limiting potentials and the free energy of OH* (Fig. 18b) [54]. It was proved again that the catalysts possessing suitable ΔG_{OH*} value (e.g., from 1.6 to 2.4 eV) and low overpotential for the 2e⁻ WOR exhibits high selectivity and activity toward the H_2O_2 production.

In 2012, a MnO_x electrocatalyst was applied for the H_2O_2 formation via the 2e⁻ WOR pathway [50]. In this system, 77% of the H_2O_2 production was achieved. Unfortunately, the activity and yield of H_2O_2 were too low. This

Table 4 Summary of electrocatalytic H_2O_2 production via a 2e$^-$ WOR pathway

| Catalyst	Electrolyte	Faraday efficiency (%)	Onset potential (V_{RHE})	Refs
MnO_x	1 M BAS	77	1.91 (1.0 mA cm^{-2})	[50]
ZnO	2 M KHCO$_3$	81 at peak potential	1.80 (0.1 mA cm^{-2})	[268]
C, N codoped TiO$_2$	0.05 M Na$_2$SO$_4$	8 (2.9 $V_{Ag/AgCl}$)	2.66 $V_{Ag/AgCl}$ (0.1 mA cm^{-2})	[270]
BiVO$_4$/FTO	2.0 M KHCO$_3$	35	~2.50 (0.1 mA cm^{-2})	[271]
CaSnO$_3$	2 M KHCO$_3$	76 (3.2 V_{RHE})	1.99 (0.2 mA cm^{-2})	[267]
SnO$_2$	2 M KHCO$_3$	32 (3.2 V_{RHE})	2.13 (0.2 mA cm^{-2})	
4:1 (Ti,Mn)O$_x$	0.5 M pH = 7 phosphate buffer	98 (0.1 mA cm^{-2})	1.89 (0.2 mA cm^{-2})	[269]
Gd-Doped BiVO$_4$ (6% Gd:BVO)	2 M KHCO$_3$	78 (~ 3.2 V_{RHE})	2.15	[264]
Bi$_2$WO$_6$:5%Mo	2 M KHCO$_3$	79 (3.2 V_{RHE})	–	[265]
Nanoneedles BiVO$_4$	1 M KHCO$_3$	–	2.25 (2.5 mA cm^{-2})	[263]
Al$_2$O$_3$(CVD5)/BiVO$_4$/FTO	0.5 M KHCO$_3$	97 (I = 2 mA)	–	[272]
BiVO$_4$	1 M NaHCO$_3$	70 (3.1 V_{RHE})	~1.90 (0.2 mA cm^{-2})	[262]
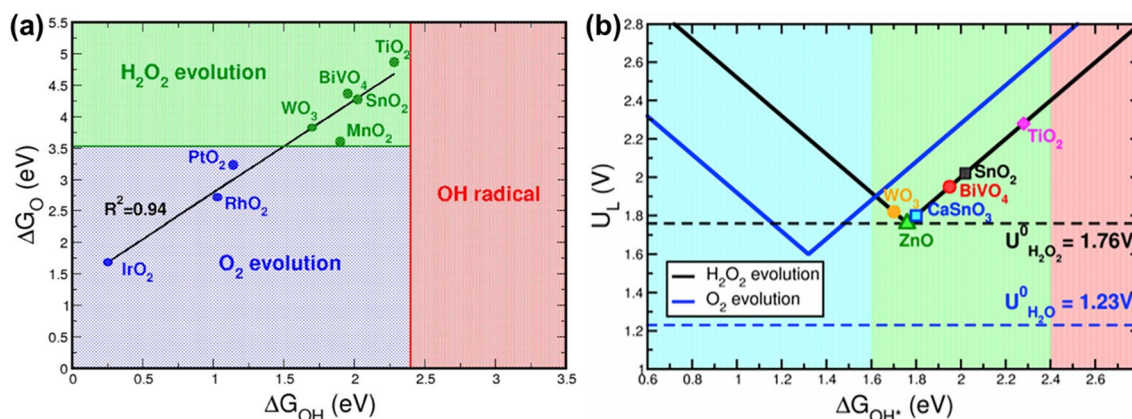
Fig. 18 a Phase diagram represented by the binding energies of O* and OH*. Reproduced with permission from Ref. [261]. Copyright 2017 American Chemical Society. **b** Activity volcano plots for the 2e$^-$ and 4e$^-$ WOR. Reproduced with permission from Ref. [54]. Copyright 2020 Elsevier

low efficiency was attributed to the competing process of the 4e$^-$ ORR and/or continuous loss of H_2O_2 from the disproportionation. Three BiVO$_4$ catalysts with different morphologies containing different surface ratios of (−121) and (040) facets (so-called seed, nanoneedles and truncated BiVO$_4$) have been applied for electrocatalytic H_2O_2 production [263]. The high-index plane (−121) was disclosed to be favorable for the H_2O_2 formation in 1 M KHCO$_3$ electrolyte rather than the O$_2$ formation. Unfortunately, BiVO$_4$ has poor stability in H_2O_2 synthesis [264]. The Bi$_2$WO$_6$ catalysts were then selected as alternatives to BiVO$_4$ for the H_2O_2 generation via the 2e$^-$ WOR pathway [265]. Among a series of Bi-based oxides (Fig. 19a), Bi$_2$O$_3$, BiVO$_4$ and

Bi$_2$WO$_6$ displayed preference for electrocatalytic H_2O_2 production. On the Bi$_2$WO$_6$ electrocatalyst, the best performance for H_2O_2 generation was achieved. The current density on the Bi$_2$WO$_6$ electrocatalyst was further increased by means of optimizing the morphology and Mo doping of the Bi$_2$WO$_6$ electrocatalyst. The faradaic efficiency of a FTO/Bi$_2$WO$_6$:5%Mo electrocatalyst was 79% at 3.2 V_{RHE} and its maximum yield rate of electrocatalytic H_2O_2 generation rate was as high as 300 µmol h^{-1} cm^{-2} at 3.4 V_{RHE} (Fig. 19b). The durability test of this electrocatalyst is very stable for such electrocatalytic H_2O_2 production (Fig. 19c).

Other metal oxides such as CaSnO$_3$ and ZnO have been also used for the H_2O_2 production via the 2e$^-$ WOR
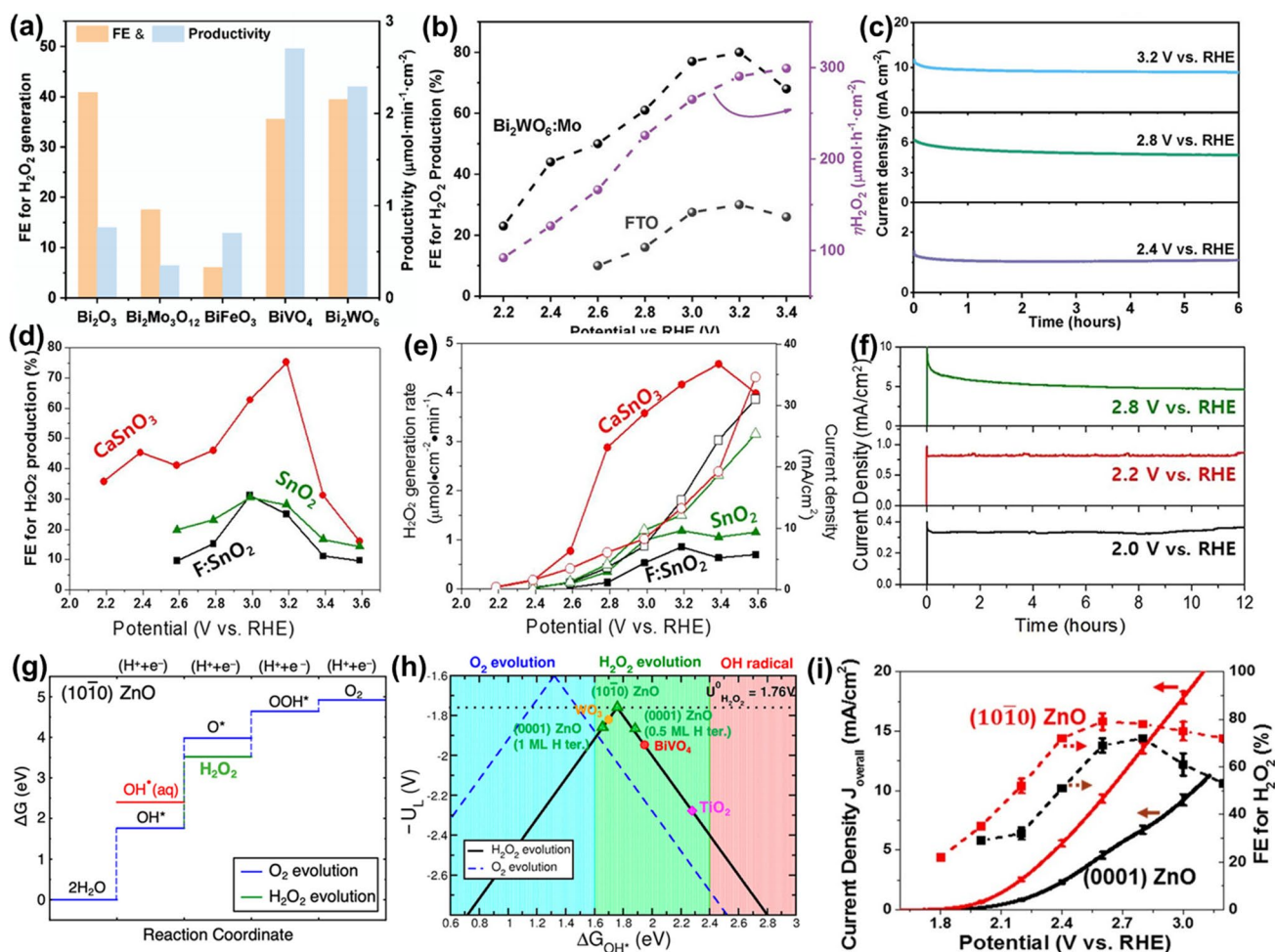
Fig. 19 a Faradaic efficiencies (FEs) and productivity of Bi-based oxides at 2.6 V_{RHE}. **b** FE and H_2O_2 generation rate of a FTO/Bi_2WO_6:5%Mo electrocatalyst at various potentials. **c** Stability measurement of a FTO/Bi_2WO_6:5%Mo electrocatalyst under different potentials. Reproduced with permission from Ref. [265]. Copyright 2020 Wiley–VCH GmbH. **d** FE, H_2O_2 generation rates and **e** the densities of different catalysts at different potentials. **f** Durability test of $CaSnO_3$ catalyst under various potentials. Reproduced with permission from Ref. [267]. Copyright 2019 American Chemical Society. **g** Free energy diagram of the WOR for the most active (10 $\bar{1}$ 0) ZnO catalyst. **h** Volcano plots of 4e⁻ WOR to O_2 and 2e⁻ WOR to H_2O_2 as a function of OH* binding free energies (ΔG_{OH*}). **i** Overall current density and FE for H_2O_2. Reproduced with permission from Ref. [268]. Copyright 2019 American Chemical Society

pathway [266–268]. For example, $CaSnO_3$ nanoparticles, prepared via the colloidal synthesis method, have been employed to evaluate H_2O_2 production in 2 M $KHCO_3$ electrolyte [267]. Its Faraday efficiency (FE) was 76% at 3.2 V_{RHE}, higher than that of F:SnO_2 and SnO_2 (Fig. 19d). The H_2O_2 generation rates are outstanding at applied potentials (Fig. 19e). Meanwhile, it exhibited excellent stability during this 2e⁻ WOR process at 2.0 V_{RHE} within 12 h. Slight decrease occurred when a potential of at 2.2 or 2.8 V_{RHE} is applied (Fig. 19f). In another case, metal oxide of ZnO was identified as an ideal catalyst for electrocatalytic H_2O_2 synthesis. The (10

$\bar{1}$ 0) facet on the ZnO catalyst is more favorable than the (0001) facet, as demonstrated by the DFT calculations (Fig. 19g, h) [268]. Experimental results further indicated that ZnO nanoparticles with a high fraction of (10 $\bar{1}$ 0) facets own outstanding performance for catalytic H_2O_2 generation: the overpotential of 40 mV at a current density of 0.1 mA cm⁻² and an FE of 81% during this 2e⁻ WOR process (Fig. 19i). Mn-alloyed TiO_2 coatings, prepared by atomic layer deposition, also exhibited the high performance of electrocatalytic H_2O_2 generation via a 2e⁻ WOR pathway: e.g., an FE of higher than > 90%

at the overpotential smaller than 150 mV [269]. It has to highlight here that the principles in designing the electrocatalysts with high performance toward the $2e^-$ WOR is still unclear at this stage. More explorations on reaction mechanism for WOR need be provided in future.

4.2.2 Boron-Doped Diamond

As discussed, various noble metal oxides have shown the capability to generate H_2O_2 through a $2e^-$ WOR pathway. However, these noble metals are expensive and rare. Up to date, the efficiency of the H_2O_2 production via $2e^-$ WOR is low. On the other side, noble metal-free oxides are not adapted to be operated at the high current densities and high potentials that are frequently required for the large-scale applications. Among the materials that can endure the corrosion in such a harsh conditions for water oxidation, some molecular metal porphyrins (e.g., AlTMPyP, SiTPyP, ZnTMPyP, SnTMPyP) [273–276] and carbon fibers [57, 277] are promising and thus have been tried for H_2O_2 production via the $2e^-$ WOR pathway, but their performance was still poor.

Boron-doped diamond (BDD), as a unique kind of carbon material with excellent physical–chemical stability [278], has been employed for the H_2O_2 generation via the $2e^-$ WOR pathway. Since the H_2O_2 production through $2e^-$ WOR on the BDD electrode was reported for the first time in 2003 [279, 280], the catalytic performance of electrochemical H_2O_2 formation using synthetic BDD films that were coated on a titanium substrate has stimulated extensive attention [281]. The BDD exhibited a H_2O_2 yield of as high as 29.0 mmol dm^{-3} at 3.47 V_{RHE}. The H_2O_2 production rate was 19.7 μmol min^{-1} cm^{-2}. However, the FE was only 28% at 3.17 V_{RHE} and total current densities surpassed 120 mA cm^{-2}, suggesting a high energy consumption process. To promote the electrocatalytic H_2O_2 generation on BDD via the $2e^-$ WOR pathway as well as to decrease the overpotential at a high applied current density, BBD films were optimized by tailoring their boron content, thickness and crystal size [282]. On the BDD-4 (with the B doping level of 12,600 ppm, film thickness of 2 μm), the biggest FE of 87% was reached and the H_2O_2 production rate was 76.4 μmol cm^{-2} min^{-1}. This BDD-4 was also superb durable (e.g., electrocatalytic H_2O_2 production for 10 h at a constant

current density of 200 mA cm^{-2}). An electrogenerated chemiluminescence (ECL) system was developed via *in-situ* coreactant production at a BDD electrode [283], where peroxydicarbonate ($C_2O_6^{2-}$) was produced by the oxidation of carbonate (CO_3^{2-}), subsequently reacted with water in basic media to form H_2O_2. Based on experimental and no-economic examination, the efficiency of anodic H_2O_2 production on a BDD electrode was explored in an electrochemical H_2/H_2O_2 process using sodium carbonate as an electrolyte [284]. The calculated FE of producing H_2O_2 was to up to 31.7% at 2.90 V (*vs.* SHE) and the corresponding production rate reached 3.93 μmol min^{-1} cm^{-2}. This study provided guidance to further implement selective oxidation of water to H_2O_2 on a BDD electrode.

Note that great progress has been made in the H_2O_2 preparation using photo- and photoelectro-catalytic approaches for wastewater treatment at a pilot scale, even an industrial scale. This is because the efficient H_2O_2 production is necessary to guarantee Fenton's reaction [285, 286]. For example, a carbon-PTFE electro-oxidative system promoted the oxidative power of Fenton and Fenton-like processes based on the enhanced H_2O_2 generation with a higher current efficiency [287]. Solar photoelectro-fenton (SPEF) with a BDD anode and a cathode of the (Co, S, P)-decorated multiwalled carbon nanotubes showed the excellent performance for bronopol removal due to the high efficiency of H_2O_2 production via the $2e^-$ WOR on a BDD [288].

5 Conclusions and Perspectives

This article provides an overview of current advances on photo/electro-catalytic H_2O_2 production using different pathways. Different photo/electro-catalysts have been detailed. Compared with traditional preparation methods, such as AQ oxidation, based on fossil resources, the direct preparation of H_2O_2 through photo/electro-catalytic processes appears to be more promising in that these processes are simple to be operated, green and safe, sustainable and clean, especially when solar or wind energy is integrated. The used catalyst is the prerequisite and technical core to determine the efficiency of such catalytic H_2O_2 generation among these technologies, especially in the application beyond the laboratory. In more detail, many advanced photo/electro-catalysts must be constructed

under theoretic guidance, including the strategies of their synthesis, design of their components/structures. Once their photo/electro-chemical properties are explored and discussed, their catalytic H_2O_2 production is possible to be boosted. However, the mechanism comprehension of various catalysts for their photo/electro-chemical H_2O_2 production is still in the preliminary stage of research, and there is still much room for further improvement.

In the field of the photocatalytic synthesis of H_2O_2 by means of either the $2e^-$ ORR pathway or the $2e^-$ WOR process, it is concluded that an ideal catalyst needs simultaneously satisfy good photoresponse (e.g., an appropriate band gap), superior separation capacity of photogenerated carriers (namely electrons and holes), as well as high catalytic ability for the H_2O_2 yield. However, the reported photocatalysts up to date still suffer from relatively low activity or selectivity of H_2O_2, which remains a great challenge for practical applications. Future studies should propose the innovative ideas for applying cooperative modulation of light adsorption, photogenerated charge separation and catalytic reaction actives in photocatalysts to enhance catalytic H_2O_2 production. In these regards, supramolecular semiconductors, including MOFs, covalent organic frameworks (COFs) and conjugated polymers can be added as the co-catalysts to improve the H_2O_2 yield. This is because the energy band structures of these supramolecular semiconductors can be optimized. In other words, their light absorption, charge separation and redox capability can be tuned during the photocatalytic H_2O_2 production. Another promising strategy is to combine inorganic semiconductors with biomolecules to strengthen the response to the solar light and the selectivity of electrocatalytic H_2O_2 production. It must be pointed out that although standard photocatalysts (e.g., g-C_3N_4 and TiO_2 materials) have achieved selective H_2O_2 synthesis under visible light irradiation, organic sacrificial agents are usually used to improve the separation of photogenerated electrons and holes in these cases. Such an approach inevitably leads to the contamination of H_2O_2. Additional cost is then required to separate and obtain pure H_2O_2. Consequently, the strategies based on electrochemical assistance, oil–water phase solution and all-solid-state Z-scheme photocatalytic systems appear to effectively facilitate the photogenerated charge separation. Note that the output of H_2O_2 produced by the currently reported catalysts is only at the mM or μM level, too far for large-scale and industrial applications. Porous photocatalysts

and/or new photocatalytic reaction systems with enhanced mass transfer rates are needed to boost the formed H_2O_2 removal from the active sites and to avoid the H_2O_2 decomposition. A deep understanding of the photocatalytic mechanism will open up new opportunities for the design of high efficiency photocatalysts. Various high-quality and *in-situ* characterization technologies (e.g., *in-situ* HRTEM, IR, XANES) are helpful to disclose the distinct dynamic behavior and reaction mechanism of different photocatalytic H_2O_2 formation systems. In short, exploring effective strategies to promote the ability to harvest wide solar spectrum, improving the lifetime of photogenerated electrons and holes and propelling the $2e^-$ ORR or water oxidation via the design of advanced photocatalysts have been becoming a hot issue for photocatalytic H_2O_2 production.

Like photocatalytic H_2O_2 synthesis, electrocatalytic H_2O_2 synthesis includes two pathways: $2e^-$ ORR and $2e^-$ WOR processes, accompanying with significant achievements acquired in the past few years. Various electrocatalysts with high selectivity (or Faraday efficiencies) and stability have been developed. However, more efforts are still needed to explore and disclose the mechanisms behind. Take the $2e^-$ ORR process as an example, previous reports have revealed that noble metal-based electrocatalysts (e.g., Pt- and Pd-based electrocatalysts) exhibited decent performance for electrocatalytic H_2O_2 production. Unfortunately, owing to their high costs and scarce reserves, it is unrealistic to use them for industrial H_2O_2 production. To address this issue, noble-based alloys, noble catalysts with core–shell structures, and porous or single atomic noble metal catalysts are highly desirable for high-performance H_2O_2 production. Alternatively, carbon-based materials are recognized as potential ones to noble catalysts for the large-scale H_2O_2 generation. Note that pristine carbon is generally inert for H_2O_2 generation due to its lack of active sites. Its catalytic performance can be integrated and improved by the modification of surface carbon atoms such as the manufacture of porous structures and defects, the introduction of heteroatom doping and oxygen functionalization. Nevertheless, most carbon electrocatalysts are only applicable for the H_2O_2 production under alkaline conditions. Their further research is thus needed to improve catalytic performance in acidic media. Moreover, the hurdle of their instability that is caused by the H_2O_2 decomposition as well as their low selectivity over a wide potential range inhibits the practical applications of carbon electrocatalysts.

Some new electrochemical and photochemical electrode systems need to be designed and developed. For example, BDD, a robust sp^3 hybridized carbon material, has exhibited extremely high durability for the H_2O_2 production in harsh conditions. It is thus highly promising for industrial H_2O_2 production once the manufacturing cost of BDD films is dramatically reduced. Moreover, the structure–activity relationship of these electrode systems, especially when they are at nanoscales, is critical for the H_2O_2 production. Only on their optimized interfaces, the highly efficient H_2O_2 synthesis can be realized. To reduce the H_2O_2 decomposition, it is better to construct porous structures or multi-site active centers inside carbon electrocatalysts, which can prohibit the formed H_2O_2 from further reaction. One more promising strategy is to couple external means (e.g., ultrasound and microwave) with electrochemical approaches to firm up the H_2O_2 desorption from the electrocatalysts. To increase the selectivity of the H_2O_2 production, the sizes and exposed planes of the used electrocatalysts should be further optimized. The employment of the $2e^-$ WOR process should be paid more attention as a more effective pathway for the H_2O_2 production where no gas phase is involved. As confirmed from theoretical calculations and experimental operations, metal oxides (e.g., $BiVO_4$, SnO_2 and ZnO) tend to generate H_2O_2 via the $2e^-$ WOR approach, while others (e.g., IrO_2, PtO_2 and RhO_2) are more favorable for the $4e^-$ WOR approach to produce O_2. In this context, it is highly necessary to further study the mechanisms of the H_2O_2 formation via the $2e^-$ WOR approach. Once advanced metal oxide catalysts are found, electrocatalytic H_2O_2 production on these metal oxide electrocatalysts can be further enhanced. It is worth mentioning that BDD presented good ability to produce H_2O_2 at high potentials. However, it only exhibited low Faraday efficiency. To utilize diamond for industrial H_2O_2 production at high current densities, it is urgently needed to improve its catalytic ability by the formation of its nanostructures or the introduction other catalytic centers (e.g., defects, dopants, other catalysts).

To sum up, recent advances in the design and synthesis of photo/electro-catalysts have improved their activity, selectivity and stability for photo/electro-catalytic H_2O_2 production in past years. To further improve performance of photo/electro-catalytic H_2O_2 production, the design of advanced catalysts with various functions is still highly necessary. For photocatalysts, two-channel reaction pathways for generating H_2O_2 with high efficiency are highly pursued. As for electrocatalysts, their high activity with low cost and strong durability is the key factor moving forward. From a practical application perspective, further understanding the reaction kinetics using theoretical and experimental (especially *in situ* and operando techniques) as well as the design of new reactors for the H_2O_2 production at an industrial scale must be conducted in future.

References

1. R.J. Lewis, G.J. Hutchings, Recent advances in the direct synthesis of H_2O_2. ChemCatChem **11**, 298–308 (2019). https://doi.org/10.1002/cctc.201801435

2. J. Gao, B. Liu, Progress of electrochemical hydrogen peroxide synthesis over single atom catalysts. ACS Mater. Lett. **2**, 1008–1024 (2020). https://doi.org/10.1021/acsmaterialslett.0c00189

3. A. Torres-Pinto, M.J. Sampaio, C.G. Silva, J.L. Faria, A.M.T. Silva, Recent strategies for hydrogen peroxide production by metal-free carbon nitride photocatalysts. Catalysts **9**, 990 (2019). https://doi.org/10.3390/catal9120990

4. S.C. Perry, D. Pangotra, L. Vieira, L.-I. Csepei, V. Sieber et al., Electrochemical synthesis of hydrogen peroxide from water and oxygen. Nat. Rev. Chem. **3**, 442–458 (2019). https://doi.org/10.1038/s41570-019-0110-6

5. S. Siahrostami, A. Verdaguer-Casadevall, M. Karamad, D. Deiana, P. Malacrida et al., Enabling direct H_2O_2 production through rational electrocatalyst design. Nat. Mater. **12**, 1137–1143 (2013). https://doi.org/10.1038/NMAT3795

6. J. Chen, Q. Ma, X. Zheng, Y. Fang, J. Wang et al., Kinetically restrained oxygen reduction to hydrogen peroxide with nearly 100% selectivity. Nat. Commun. **13**, 2808 (2022). https://doi.org/10.1038/s41467-022-30411-7

7. J. Wu, Y. Han, Y. Bai, X. Wang, Y. Zhou et al., The electron transport regulation in carbon dots/In_2O_3 electrocatalyst enable 100% selectivity for oxygen reduction to hydrogen peroxide. Adv. Funct. Mater. **32**, 2203647 (2022). https://doi.org/10.1002/adfm.202203647

8. J.M. Campos-Martin, G. Blanco-Brieva, J.L.G. Fierro, Hydrogen peroxide synthesis: an outlook beyond the anthraquinone process. Angew. Chem. Int. Ed. **45**, 6962–6984 (2006). https://doi.org/10.1002/anie.200503779

9. S.-I. Yamazaki, Z. Siroma, H. Senoh, T. Loroi, N. Fujiwara et al., A fuel cell with selective electrocatalysts using hydrogen peroxide as both an electron acceptor and a fuel. J. Power Sources **178**, 20–25 (2008). https://doi.org/10.1016/j.jpowsour.2007.12.013

10. S.A.M. Shaegh, N. Nam-Trung, S.M.M. Ehteshami, S.H. Chan, A membraneless hydrogen peroxide fuel cell using prussian blue as cathode material. Energy Environ. Sci. **5**, 8225–8228 (2012). https://doi.org/10.1039/c2ee21806b

11. Y. Liu, P. Vijayakumar, Q. Liu, T. Sakthivel, F. Chen et al., Shining light on anion-mixed nanocatalysts for efficient water electrolysis: fundamentals, progress, and perspectives. Nano-Micro Lett. **14**, 43 (2022). https://doi.org/10.1007/s40820-021-00785-2

12. S. Kato, J. Jung, T. Suenobu, S. Fukuzumi, Production of hydrogen peroxide as a sustainable solar fuel from water and dioxygen. Energy Environ. Sci. **6**, 3756–3764 (2013). https://doi.org/10.1039/c3ee42815j

13. Y. Kofuji, Y. Isobe, Y. Shiraishi, H. Sakamoto, S. Tanaka et al., Carbon nitride-aromatic diimide-graphene nanohybrids: metal-free photocatalysts for solar-to-hydrogen peroxide energy conversion with 0.2% efficiency. J. Am. Chem. Soc. **138**, 10019–10025 (2016). https://doi.org/10.1021/jacs.6b05806

14. S. Gogoi, N. Karak, Solar-driven hydrogen peroxide production using polymer-supported carbon dots as heterogeneous catalyst. Nano-Micro Lett. **9**, 40 (2017). https://doi.org/10.1007/s40820-017-0143-7

15. K. Mase, M. Yoneda, Y. Yamada, S. Fukuzumi, Seawater usable for production and consumption of hydrogen peroxide as a solar fuel. Nat. Commun. **7**, 11470 (2016). https://doi.org/10.1038/ncomms11470

16. X. Zeng, Y. Liu, X. Hu, X. Zhang, Photoredox catalysis over semiconductors for light-driven hydrogen peroxide production. Green Chem. **23**, 1466–1494 (2021). https://doi.org/10.1039/d0gc04236f

17. Z. Yao, J. Zhao, R.J. Bunting, C. Zhao, P. Hu et al., Quantitative insights into the reaction mechanism for the direct synthesis of H_2O_2 over transition metals: coverage-dependent microkinetic modeling. ACS Catal. **11**, 1202–1221 (2021). https://doi.org/10.1021/acscatal.0c04125

18. S. Siahrostami, S.J. Villegas, A.H.B. Mostaghimi, S. Back, A.B. Farimani et al., A review on challenges and successes in atomic-scale design of catalysts for electrochemical synthesis of hydrogen heroxide. ACS Catal. **10**, 7495–7511 (2020). https://doi.org/10.1021/acscatal.0c01641

19. G.-H. Han, S.-H. Lee, S.-Y. Hwang, K.-Y. Lee, Advanced development strategy of nano catalyst and DFT calculations for direct synthesis of hydrogen peroxide. Adv. Energy Mater. **11**, 2003121 (2021). https://doi.org/10.1002/aenm.202003121

20. Y. Sun, L. Han, P. Strasser, A comparative perspective of electrochemical and photochemical approaches for catalytic H_2O_2 production. Chem. Soc. Rev. **49**, 6605–6631 (2020). https://doi.org/10.1039/d0cs00458h

21. C. Xia, Y. Xia, P. Zhu, L. Fan, H. Wang, Direct electrosynthesis of pure aqueous H_2O_2 solutions up to 20% by weight using a solid electrolyte. Science **366**, 226 (2019). https://doi.org/10.1126/science.aay1844

22. Z. Lu, G. Chen, S. Siahrostami, Z. Chen, K. Liu et al., High-efficiency oxygen reduction to hydrogen peroxide catalysed by oxidized carbon materials. Nat. Catal. **1**, 156–162 (2018). https://doi.org/10.1038/s41929-017-0017-x

23. S.J. Freakley, Q. He, J.H. Harrhy, L. Lu, D.A. Crole et al., Palladium-tin catalysts for the direct synthesis of H_2O_2 with high selectivity. Science **351**, 965–968 (2016). https://doi.org/10.1126/science.aad5705

24. J.K. Edwards, S.J. Freakley, A.F. Carley, C.J. Kiely, G.J. Hutchings, Strategies for designing supported gold-palladium bimetallic catalysts for the direct synthesis of hydrogen peroxide. Acc. Chem. Res. **47**, 845–854 (2014). https://doi.org/10.1021/ar400177c

25. J. Garcia-Serna, T. Moreno, P. Biasi, M.J. Cocero, J.-P. Mikkola et al., Engineering in direct synthesis of hydrogen peroxide: targets, reactors and guidelines for operational conditions. Green Chem. **16**, 2320–2343 (2014). https://doi.org/10.1039/c3gc41600c

26. R.B. Rankin, J. Greeley, Trends in selective hydrogen peroxide production on transition metal surfaces from first principles. ACS Catal. **2**, 2664–2672 (2012). https://doi.org/10.1021/cs3003337

27. J.K. Edwards, B. Solsona, A.F. Carley, A.A. Herzing, C.J. Kiely et al., Switching off hydrogen peroxide hydrogenation in the direct synthesis process. Science **323**, 1037–1041 (2009). https://doi.org/10.1126/science.1168980

28. K. Dong, Y. Lei, H. Zhao, J. Liang, P. Ding et al., Noble-metal-free electrocatalysts toward H_2O_2 production. J. Mater. Chem. A **8**, 23123–23141 (2020). https://doi.org/10.1039/d0ta08894c

29. H. Lu, X. Li, S.A. Monny, Z. Wang, L. Wang, Photoelectrocatalytic hydrogen peroxide production based on transition-metal-oxide semiconductors. Chin. J. Catal. **43**, 1204–1215 (2022). https://doi.org/10.1016/S1872-2067(21)64028-7

30. L.-H. Fu, C. Qi, J. Lin, P. Huang, Catalytic chemistry of glucose oxidase in cancer diagnosis and treatment. Chem. Soc. Rev. **47**, 6454–6472 (2018). https://doi.org/10.1039/c7cs00891k

31. W. Luo, C. Zhu, S. Su, D. Li, Y. He et al., Self-catalyzed, self-limiting growth of glucose oxidase-mimicking gold

nanoparticles. ACS Nano **4**, 7451–7458 (2010). https://doi.org/10.1021/nn102592h

32. J. Fang, T. Sawa, T. Akaike, H. Maeda, Tumor-targeted delivery of polyethylene glycol-conjugated D-amino acid oxidase for antitumor therapy via enzymatic generation of hydrogen peroxide. Cancer Res. **62**, 3138–3143 (2002)

33. A. Parra, E. Casero, F. Pariente, L. Vazquez, E. Lorenzo, Cholesterol oxidase modified gold electrodes as bioanalytical devices. Sens. Actuators B **124**, 30–37 (2007). https://doi.org/10.1016/j.snb.2006.11.051

34. S.C. Perry, S.M. Gateman, J. Sifakis, L. Pollegioni, J. Mauzeroll, Enhancement of the enzymatic biosensor response through targeted electrode surface roughness. J. Electrochem. Soc. **165**, G3074–G3079 (2018). https://doi.org/10.1149/2.0121812jes

35. D. Polcari, S.C. Perry, L. Pollegioni, M. Geissler, J. Mauzeroll et al., Localized detection of D-serine by using an enzymatic amperometric biosensor and scanning electrochemical microscopy. ChemElectroChem **4**, 920–926 (2017). https://doi.org/10.1002/celc.201600766

36. L. Wang, J. Zhang, Y. Zhang, H. Yu, Y. Qu et al., Inorganic metal-oxide photocatalyst for H_2O_2 production. Small **18**, 2104561 (2022). https://doi.org/10.1002/smll.202104561

37. S. Fukuzumi, Y.-M. Lee, W. Nam, Solar-driven production of hydrogen peroxide from water and dioxygen. Chem. Eur. J. **24**, 5016 (2018). https://doi.org/10.1002/chem.201704512

38. Y. Pang, H. Xie, Y. Sun, M.-M. Titirici, G.-L. Chai, Electrochemical oxygen reduction for H_2O_2 production: catalysts, pH effects and mechanisms. J. Mater. Chem. A **8**, 24996–25016 (2020). https://doi.org/10.1039/d0ta09122g

39. X. Yang, Y. Zeng, W. Alnoush, Y. Hou, D. Higgins et al., Tuning two-electron oxygen-reduction pathways for H_2O_2 electrosynthesis via engineering atomically dispersed single metal site catalysts. Adv. Mater. **34**, 2107954 (2022). https://doi.org/10.1002/adma.202107954

40. H.-I. Kim, O.S. Kwon, S. Kim, W. Choi, J.-H. Kim, Harnessing low energy photons (635 nm) for the production of H_2O_2 using upconversion nanohybrid photocatalysts. Energy Environ. Sci. **9**, 1063–1073 (2016). https://doi.org/10.1039/c5ee03115j

41. Y. Jiang, P. Ni, C. Chen, Y. Lu, P. Yang et al., Selective electrochemical H_2O_2 production through two-electron oxygen electrochemistry. Adv. Energy Mater. **8**, 1801909 (2018). https://doi.org/10.1002/aenm.201801909

42. Y.-J. Ko, K. Choi, B. Yang, W.H. Lee, J.-Y. Kim et al., A catalyst design for selective electrochemical reactions: direct production of hydrogen peroxide in advanced electrochemical oxidation. J. Mater. Chem. A **8**, 9859–9870 (2020). https://doi.org/10.1039/d0ta01869d

43. L.E.B. Lucchetti, M.O. Almeida, J.M. de Almeida, P.A.S. Autreto, K.M. Honorio et al., Density functional theory studies of oxygen reduction reaction for hydrogen peroxide generation on graphene-based catalysts. J. Electroanal. Chem. **895**, 115429 (2021). https://doi.org/10.1016/j.jelechem.2021.115429

44. L. Cheng, Q. Xiang, Y. Liao, H. Zhang, CdS-based photocatalysts. Energy Environ. Sci. **11**, 1362–1391 (2018). https://doi.org/10.1039/c7ee03640j

45. J. Fu, J. Yu, C. Jiang, B. Cheng, g-C_3N_4-Based heterostructured photocatalysts. Adv. Energy Mater. **8**, 1701503 (2018). https://doi.org/10.1002/aenm.201701503

46. J. Xiong, J. Di, J. Xia, W. Zhu, H. Li, Surface defect engineering in 2D nanomaterials for photocatalysis. Adv. Funct. Mater. **28**, 1801983 (2018). https://doi.org/10.1002/adfm.201801983

47. H. Hou, X. Zeng, X. Zhang, Production of hydrogen peroxide by photocatalytic processes. Angew. Chem. Int. Ed. **59**, 17356–17376 (2020). https://doi.org/10.1002/anie.201911609

48. Z. Liu, X. Sheng, D. Wang, X. Feng, Efficient hydrogen peroxide generation utilizing photocatalytic oxygen reduction at a triphase interface. Iscience **17**, 67 (2019). https://doi.org/10.1016/j.isci.2019.06.023

49. F. Xue, Y. Si, M. Wang, M. Liu, L. Guo, Toward efficient photocatalytic pure water splitting for simultaneous H_2 and H_2O_2 production. Nano Energy **62**, 823–831 (2019). https://doi.org/10.1016/j.nanoen.2019.05.086

50. A. Izgorodin, E. Izgorodina, D.R. MacFarlane, Low overpotential water oxidation to hydrogen peroxide on a MnO_x catalyst. Energy Environ. Sci. **5**, 9496–9501 (2012). https://doi.org/10.1039/c2ee21832a

51. X.J. Shi, Y.R. Zhang, S. Siahrostami, X.L. Zheng, Light-driven $BiVO_4$-C fuel cell with simultaneous production of H_2O_2. Adv. Energy Mater. **8**, 1801158 (2018). https://doi.org/10.1002/aenm.201801158

52. S. Back, J. Na, Z.W. Ulissi, Efficient discovery of active, selective, and stable catalysts for electrochemical H_2O_2 synthesis through active motif screening. ACS Catal. **11**, 2483–2491 (2021). https://doi.org/10.1021/acscatal.0c05494

53. J. Zhang, H. Zhang, M.-J. Cheng, Q. Lu, Tailoring the electrochemical production of H_2O_2: strategies for the rational design of high-performance electrocatalysts. Small **16**, 1902845 (2020). https://doi.org/10.1002/smll.201902845

54. X. Shi, S. Back, T.M. Gill, S. Siahrostami, X. Zheng, Electrochemical synthesis of H_2O_2 by two-electron water oxidation reaction. Chem **7**, 38–63 (2021). https://doi.org/10.1016/j.chempr.2020.09.013

55. K. Wang, J. Huang, H. Chen, Y. Wang, S. Song, Recent advances in electrochemical 2e oxygen reduction reaction for on-site hydrogen peroxide production and beyond. Chem. Commun. **56**, 12109–12121 (2020). https://doi.org/10.1039/d0cc05156j

56. S. Mavrikis, S.C. Perry, P.K. Leung, L. Wang, C.P. de Leon, Recent advances in electrochemical water oxidation to produce hydrogen peroxide: a mechanistic perspective. ACS Sustainable Chem. Eng. **9**, 76–91 (2021). https://doi.org/10.1021/acssuschemeng.0c07263

57. C. Xia, S. Back, S. Ringe, K. Jiang, F. Chen et al., Confined local oxygen gas promotes electrochemical water oxidation

to hydrogen peroxide. Nat. Catal. **3**, 125–134 (2020). https://doi.org/10.1038/s41929-019-0402-8

58. Y. Xue, Y. Wang, Z. Pan, K. Sayama, Electrochemical and photoelectrochemical water oxidation for hydrogen peroxide production. Angew. Chem. Int. Ed. **60**, 10469–10480 (2021). https://doi.org/10.1002/anie.202011215

59. X. Wang, K. Maeda, A. Thomas, K. Takanabe, G. Xin et al., A metal-free polymeric photocatalyst for hydrogen production from water under visible light. Nat. Mater. **8**, 76–80 (2009). https://doi.org/10.1038/NMAT2317

60. X. Wang, K. Maeda, X. Chen, K. Takanabe, K. Domen et al., Polymer semiconductors for artificial photosynthesis: hydrogen evolution by mesoporous graphitic carbon nitride with visible light. J. Am. Chem. Soc. **131**, 1680 (2009). https://doi.org/10.1021/ja809307s

61. M. Wang, P. Ju, J. Li, Y. Zhao, X. Han et al., Facile synthesis of MoS_2/g-C_3N_4/GO ternary heterojunction with enhanced photocatalytic activity for water splitting. ACS Sustainable Chem. Eng. **5**, 7878–7886 (2017). https://doi.org/10.1021/acssuschemeng.7b01386

62. L. Jiang, X. Yuan, Y. Pan, J. Liang, G. Zeng et al., Doping of graphitic carbon nitride for photocatalysis: a reveiw. Appl. Catal. B **217**, 388–406 (2017). https://doi.org/10.1016/j.apcatb.2017.06.003

63. Y.-X. Ye, C. Wen, J. Pan, J.-W. Wang, Y.-J. Tong et al., Visible-light driven efficient overall H_2O_2 production on modified graphitic carbon nitride under ambient conditions. Appl. Catal. B **285**, 119726 (2021). https://doi.org/10.1016/j.apcatb.2020.119726

64. G. Dong, L. Zhang, Synthesis and enhanced Cr(VI) photoreduction property of formate anion containing graphitic carbon nitride. J. Phys. Chem. C **117**, 4062–4068 (2013). https://doi.org/10.1021/jp3115226

65. S. Cao, J. Low, J. Yu, M. Jaroniec, Polymeric photocatalysts based on graphitic carbon nitride. Adv. Mater. **27**, 2150–2176 (2015). https://doi.org/10.1002/adma.201500033

66. S. Yang, Y. Gong, J. Zhang, L. Zhan, L. Ma et al., Exfoliated graphitic carbon nitride nanosheets as efficient catalysts for hydrogen evolution under visible light. Adv. Mater. **25**, 2452–2456 (2013). https://doi.org/10.1002/adma.201204453

67. H. Piao, G. Choi, X. Jin, S.-J. Hwang, Y.J. Song et al., Monolayer graphitic carbon nitride as metal-free catalyst with enhanced performance in photo- and electro-catalysis. Nano-Micro Lett. **14**, 55 (2022). https://doi.org/10.1007/s40820-022-00794-9

68. Y. Shiraishi, S. Kanazawa, Y. Sugano, D. Tsukamoto et al., Highly selective production of hydrogen peroxide on graphitic carbon nitride (g-C_3N_4) photocatalyst activated by visible light. ACS Catal. **4**, 774–780 (2014). https://doi.org/10.1021/cs401208c

69. Y. Shiraishi, Y. Kofuji, H. Sakamoto, S. Tanaka, S. Ichikawa et al., Effects of surface defects on photocatalytic H_2O_2 production by mesoporous graphitic carbon nitride under visible light irradiation. ACS Catal. **5**, 3058–3066 (2015). https://doi.org/10.1021/acscatal.5b00408

70. Z. Zhu, H. Pan, M. Murugananthan, J. Gong, Y. Zhang, Visible light-driven photocatalytically active g-C_3N_4 material for enhanced generation of H_2O_2. Appl. Catal. B **232**, 19–25 (2018). https://doi.org/10.1016/j.apcatb.2018.03.035

71. S. Li, G. Dong, R. Hailili, L. Yang, Y. Li et al., Effective photocatalytic H_2O_2 production under visible light irradiation at g-C_3N_4 modulated by carbon vacancies. Appl. Catal. B **190**, 26–35 (2016). https://doi.org/10.1016/j.apcatb.2016.03.004

72. Y. You, S. Wang, K. Xiao, T. Ma, Y. Zhang et al., Z-Scheme g-C_3N_4/Bi_4NbO_8Cl heterojunction for enhanced photocatalytic hydrogen production. ACS Sustainable Chem. Eng. **6**, 16219–16227 (2018). https://doi.org/10.1021/acssuschemeng.8b03075

73. R. Hao, G. Wang, C. Jiang, H. Tang, Q. Xu, In-situ hydrothermal synthesis of g-C_3N_4/TiO_2 heterojunction photocatalysts with high specific surface area for Rhodamine B degradation. Appl. Surf. Sci. **411**, 400–410 (2017). https://doi.org/10.1016/j.apsusc.2017.03.197

74. W. Liu, C. Song, M. Kou, Y. Wang, Y. Deng et al., Fabrication of ultra-thin g-C_3N_4 nanoplates for efficient visible-light photocatalytic H_2O_2 production via two-electron oxygen reduction. Chem. Eng. J. **425**, 130615 (2021). https://doi.org/10.1016/j.cej.2021.130615

75. T. Mahvelati-Shamsabadi, H. Fattahimoghaddam, B.-K. Lee, S. Bae, J. Ryu, Synthesis of hexagonal rosettes of g-C_3N_4 with boosted charge transfer for the enhanced visible-light photocatalytic hydrogen evolution and hydrogen peroxide production. J. Colloid Interface Sci. **597**, 345–360 (2021). https://doi.org/10.1016/j.jcis.2021.04.019

76. G. Dong, W. Ho, Y. Li, L. Zhang, Facile synthesis of porous graphene-like carbon nitride ($C_6N_9H_3$) with excellent photocatalytic activity for NO removal. Appl. Catal. B **174**, 477–485 (2015). https://doi.org/10.1016/j.apcatb.2015.03.035

77. Y. Lv, Y. Liu, Y. Zhu, Y. Zhu, Surface oxygen vacancy induced photocatalytic performance enhancement of a $BiPO_4$ nanorod. J. Mater. Chem. A **2**, 1174–1182 (2014). https://doi.org/10.1039/c3ta13841k

78. D. Chen, Z. Wang, T. Ren, H. Ding, W. Yao et al., Influence of defects on the photocatalytic activity of ZnO. J. Phys. Chem. C **118**, 15300–15307 (2014). https://doi.org/10.1021/jp5033349

79. L. Shi, L. Yang, W. Zhou, Y. Liu, L. Yin et al., Photoassisted construction of holey defective g-C_3N_4 photocatalysts for efficient visible-light-driven H_2O_2 production. Small **14**, 1703142 (2018). https://doi.org/10.1002/smll.201703142

80. H. Zhao, Q. Jin, M.A. Khan, S. Larter, S. Siahrostami et al., Rational design of carbon nitride for remarkable photocatalytic H_2O_2 production. Chem. Catalysis **2**, 1720–1733 (2022). https://doi.org/10.1016/j.checat.2022.04.015

81. H. Li, J. Shang, Z. Ai, L. Zhang, Efficient visible light nitrogen fixation with BiOBr nanosheets of oxygen vacancies on the exposed 001 facets. J. Am. Chem. Soc. **137**, 6393–6399 (2015). https://doi.org/10.1021/jacs.5b03105

82. G. Dong, W. Ho, C. Wang, Selective photocatalytic N_2 fixation dependent on g-C_3N_4 induced by nitrogen vacancies. J.

Mater. Chem. A **3**, 23435–23441 (2015). https://doi.org/10.1039/c5ta06540b

83. J. Lei, B. Chen, W. Lv, L. Zhou, L. Wang et al., Robust photocatalytic H_2O_2 production over inverse opal g-C_3N_4 with carbon vacancy under visible light. ACS Sustainable Chem. Eng. **7**, 16467–16473 (2019). https://doi.org/10.1021/acssuschemeng.9b03678

84. P. Niu, G. Liu, H.-M. Cheng, Nitrogen vacancy-promoted photocatalytic activity of graphitic carbon nitride. J. Phys. Chem. C **116**, 11013–11018 (2012). https://doi.org/10.1021/jp301026y

85. X. Qu, S. Hu, P. Li, Z. Li, H. Wang et al., The effect of embedding N vacancies into g-C_3N_4 on the photocatalytic H_2O_2 production ability via H_2 plasma treatment. Diamond Relat. Mater. **86**, 159–166 (2018). https://doi.org/10.1016/j.diamond.2018.04.027

86. H. Fattahimoghaddam, T. Mahvelati-Shamsabadi, B.-K. Lee, Enhancement in photocatalytic H_2O_2 production over g-C_3N_4 nanostructures: a collaborative approach of nitrogen deficiency and supramolecular precursors. ACS Sustainable Chem. Eng. **9**, 4520–4530 (2021). https://doi.org/10.1021/acssuschemeng.0c08884

87. J. Luo, Y. Liu, C. Fan, L. Tang, S. Yang et al., Direct attack and indirect transfer mechanisms dominated by reactive oxygen species for photocatalytic H_2O_2 production on g-C_3N_4 possessing nitrogen vacancies. ACS Catal. **11**, 11440–11450 (2021). https://doi.org/10.1021/acscatal.1c03103

88. X. Meng, L. Liu, S. Ouyang, H. Xu, D. Wang et al., Nanometals for solar-to-chemical energy conversion: from semiconductor-based photocatalysis to plasmon-mediated photocatalysis and photo-thermocatalysis. Adv. Mater. **28**, 6781–6803 (2016). https://doi.org/10.1002/adma.201600305

89. X. Chang, J. Yang, D. Han, B. Zhang, X. Xiang et al., Enhancing light-driven production of hydrogen peroxide by anchoring Au onto C_3N_4 catalysts. Catalysts **8**, 147 (2018). https://doi.org/10.3390/catal8040147

90. G. Zuo, S. Liu, L. Wang, H. Song, P. Zong et al., Finely dispersed Au nanoparticles on graphitic carbon nitride as highly active photocatalyst for hydrogen peroxide production. Catal. Commun. **123**, 69–72 (2019). https://doi.org/10.1016/j.catcom.2019.02.011

91. J. Cai, J. Huang, S. Wang, J. Iocozzia, Z. Sun et al., Crafting mussel-inspired metal nanoparticle-decorated ultrathin graphitic carbon nitride for the degradation of chemical pollutants and production of chemical resources. Adv. Mater. **31**, 1806314 (2019). https://doi.org/10.1002/adma.201806314

92. Y. Wang, X. Wang, M. Antonietti, Polymeric graphitic carbon nitride as a heterogeneous organocatalyst: from photochemistry to multipurpose catalysis to sustainable chemistry. Angew. Chem. Int. Ed. **51**, 68–89 (2012). https://doi.org/10.1002/anie.201101182

93. G. Liu, P. Niu, L. Yin, H.-M. Cheng, α-Sulfur crystals as a visible-light-active photocatalyst. J. Am. Chem. Soc. **134**, 9070–9073 (2012). https://doi.org/10.1021/ja302897b

94. T. Xiong, W. Cen, Y. Zhang, F. Dong, Bridging the g-C_3N_4 interlayers for enhanced photocatalysis. ACS Catal. **6**, 2462–2472 (2016). https://doi.org/10.1021/acscatal.5b02922

95. Q. Xu, L. Zhang, J. Yu, S. Wageh, A.A. Al-Ghamdi et al., Direct Z-scheme photocatalysts: principles, synthesis, and applications. Mater. Today **21**, 1042–1063 (2018). https://doi.org/10.1016/j.mattod.2018.04.008

96. Q. Chen, J. Li, L. Cheng, H. Liu, Construction of CdLa$_2$S$_4$/MIL-88A(Fe) heterojunctions for enhanced photocatalytic H_2 evolution activity via a direct Z-scheme electron transfer. Chem. Eng. J. **379**, 122389 (2020). https://doi.org/10.1016/j.cej.2019.122389

97. L. Yang, G. Dong, D.L. Jacobs, Y. Wang, L. Zang et al., Two-channel photocatalytic production of H_2O_2 over g-C_3N_4 nanosheets modified with perylene imides. J. Catal. **352**, 274–281 (2017). https://doi.org/10.1016/j.jcat.2017.05.010

98. Z. Li, N. Xiong, G. Gu, Fabrication of a full-spectrum-response Cu$_2$(OH)$_2$CO$_3$/g-C_3N_4 heterojunction catalyst with outstanding photocatalytic H_2O_2 production performance via a self-sacrificial method. Dalton Trans. **48**, 182–189 (2019). https://doi.org/10.1039/c8dt04081h

99. X. Zhao, Y. You, S. Huang, Y. Wu, Y. Ma et al., Z-scheme photocatalytic production of hydrogen peroxide over Bi$_4$O$_5$Br$_2$/g-C_3N_4 heterostructure under visible light. Appl. Catal. B **278**, 119251 (2020). https://doi.org/10.1016/j.apcatb.2020.119251

100. D.-L. Long, E. Burkholder, L. Cronin, Polyoxometalate clusters, nanostructures and materials: from self-assembly to designer materials and devices. Chem. Soc. Rev. **36**, 105–121 (2007). https://doi.org/10.1039/b502666k

101. H. Lv, Y.V. Geletii, C. Zhao, J.W. Vickers, G. Zhu et al., Polyoxometalate water oxidation catalysts and the production of green fuel. Chem. Soc. Rev. **41**, 7572–7589 (2012). https://doi.org/10.1039/c2cs35292c

102. S.-S. Wang, G.-Y. Yang, Recent advances in polyoxometalate-catalyzed reactions. Chem. Rev. **115**, 4893–4962 (2015). https://doi.org/10.1021/cr500390v

103. J. Ettedgui, Y. Diskin-Posner, L. Weiner, R. Neumann, Photoreduction of carbon dioxide to carbon monoxide with hydrogen catalyzed by a rhenium(I) phenanthroline-polyoxometalate hybrid complex. J. Am. Chem. Soc. **133**, 188–190 (2011). https://doi.org/10.1021/ja1078199

104. B. Rausch, M.D. Symes, G. Chisholm, L. Cronin, Decoupled catalytic hydrogen evolution from a molecular metal oxide redox mediator in water splitting. Science **345**, 1326–1330 (2014). https://doi.org/10.1126/science.1257443

105. S. Zhao, X. Zhao, H. Zhang, J. Li, Y. Zhu, Covalent combination of polyoxometalate and graphitic carbon nitride for light-driven hydrogen peroxide production. Nano Energy **35**, 405–414 (2017). https://doi.org/10.1016/j.nanoen.2017.04.017

106. S. Zhao, X. Zhao, S. Ouyang, Y. Zhu, Polyoxometalates covalently combined with graphitic carbon nitride for photocatalytic hydrogen peroxide production. Catal. Sci. Technol. **8**, 1686–1695 (2018). https://doi.org/10.1039/c8cy00043c

107. S. Zhao, X. Zhao, Polyoxometalates-derived metal oxides incorporated into graphitic carbon nitride framework for

photocatalytic hydrogen peroxide production under visible light. J. Catal. **366**, 98–106 (2018). https://doi.org/10.1016/j.jcat.2018.08.003

108. S. Zhao, X. Zhao, Insights into the role of singlet oxygen in the photocatalytic hydrogen peroxide production over polyoxometalates-derived metal oxides incorporated into graphitic carbon nitride framework. Appl. Catal. B **250**, 408–418 (2019). https://doi.org/10.1016/j.apcatb.2019.02.031

109. S. Hu, X. Qu, P. Li, F. Wang, Q. Li et al., Photocatalytic oxygen reduction to hydrogen peroxide over copper doped graphitic carbon nitride hollow microsphere: the effect of Cu(I)-N active sites. Chem. Eng. J. **334**, 410–418 (2018). https://doi.org/10.1016/j.cej.2017.10.016

110. X. Qu, S. Hu, J. Bai, P. Li, G. Lu et al., Synthesis of band gap-tunable alkali metal modified graphitic carbon nitride with outstanding photocatalytic H_2O_2 production ability via molten salt method. J. Mater. Sci. Technol. **34**, 1932–1938 (2018). https://doi.org/10.1016/j.jmst.2018.04.019

111. Y. Chen, X. Yan, J. Xu, L. Wang, K^+, Ni and carbon co-modification promoted two-electron O_2 reduction for photocatalytic H_2O_2 production by crystalline carbon nitride. J. Mater. Chem. A **9**, 24056–24063 (2021). https://doi.org/10.1039/d1ta06960h

112. G. Zhang, M. Zhang, X. Ye, X. Qiu, S. Lin et al., Iodine modified carbon nitride semiconductors as visible light photocatalysts for hydrogen evolution. Adv. Mater. **26**, 805–809 (2014). https://doi.org/10.1002/adma.201303611

113. Z.-A. Lan, G. Zhang, X. Wang, A facile synthesis of Br-modified g-C_3N_4 semiconductors for photoredox water splitting. Appl. Catal. B **192**, 116–125 (2016). https://doi.org/10.1016/j.apcatb.2016.03.062

114. C. Zhang, J. Bai, L. Ma, Y. Lv, F. Wang et al., Synthesis of halogen doped graphite carbon nitride nanorods with outstanding photocatalytic H_2O_2 production ability via saturated NH_4X (X = Cl, Br) solution-hydrothermal post-treatment. Diamond Relat. Mater. **87**, 215–222 (2018). https://doi.org/10.1016/j.diamond.2018.06.013

115. S. Kim, G.-H. Moon, H. Kim, Y. Mun, P. Zhang et al., Selective charge transfer to dioxygen on KPF_6-modified carbon nitride for photocatalytic synthesis of H_2O_2 under visible light. J. Catal. **357**, 51–58 (2018). https://doi.org/10.1016/j.jcat.2017.10.002

116. L. Zhou, J. Lei, F. Wang, L. Wang, M.R. Hoffmann et al., Carbon nitride nanotubes with in-situ grafted hydroxyl groups for highly efficient spontaneous H_2O_2 production. Appl. Catal. B **288**, 119993 (2021). https://doi.org/10.1016/j.apcatb.2021.119993

117. Y. Zheng, Y. Luo, Q. Ruan, J. Yu, X. Guo et al., Plasma-Tuned nitrogen vacancy graphitic carbon nitride sphere for efficient photocatalytic H_2O_2 production. J. Colloid Interface Sci. **609**, 75–85 (2022). https://doi.org/10.1016/j.jcis.2021.12.006

118. Y. Shao, J. Hu, T. Yang, X. Yang, J. Qu et al., Significantly enhanced photocatalytic in-situ H_2O_2 production and consumption activities for efficient sterilization by

119. ZnIn$_2$S$_4$/g-C$_3$N$_4$ heterojunction. Carbon **190**, 337–347 (2022). https://doi.org/10.1016/j.carbon.2022.01.019

119. J. Xiong, X. Li, J. Huang, X. Gao, Z. Chen et al., CN/rGO@BPQDs high-low junctions with stretching spatial charge separation ability for photocatalytic degradation and H_2O_2 production. Appl. Catal. B **266**, 118602 (2020). https://doi.org/10.1016/j.apcatb.2020.118602

120. Y. Kofuji, S. Ohkita, Y. Shiraishi, H. Sakamoto, S. Tanaka et al., Graphitic carbon nitride doped with biphenyl diimide: efficient photocatalyst for hydrogen peroxide production from water and molecular oxygen by sunlight. ACS Catal. **6**, 7021–7029 (2016). https://doi.org/10.1021/acscatal.6b02367

121. Z. Wei, M. Liu, Z. Zhang, W. Yao, H. Tan et al., Efficient visible-light-driven selective oxygen reduction to hydrogen peroxide by oxygen-enriched graphitic carbon nitride polymers. Energy Environ. Sci. **11**, 2581–2589 (2018). https://doi.org/10.1039/c8ee01316k

122. H.-I. Kim, Y. Choi, S. Hu, W. Choi, J.-H. Kim, Photocatalytic hydrogen peroxide production by anthraquinone-augmented polymeric carbon nitride. Appl. Catal. B **229**, 121–129 (2018). https://doi.org/10.1016/j.apcatb.2018.01.060

123. S. Zhao, T. Guo, X. Li, T. Xu, B. Yang et al., Carbon nanotubes covalent combined with graphitic carbon nitride for photocatalytic hydrogen peroxide production under visible light. Appl. Catal. B **224**, 725–732 (2018). https://doi.org/10.1016/j.apcatb.2017.11.005

124. C. Feng, L. Tang, Y. Deng, J. Wang, Y. Liu et al., A novel sulfur-assisted annealing method of g-C_3N_4 nanosheet compensates for the loss of light absorption with further promoted charge transfer for photocatalytic production of H_2 and H_2O_2. Appl. Catal. B **281**, 119539 (2021). https://doi.org/10.1016/j.apcatb.2020.119539

125. N. Lu, N. Liu, Y. Hui, K. Shang, N. Jiang et al., Characterization of highly effective plasma-treated g-C_3N_4 and application to the photocatalytic H_2O_2 production. Chemosphere **241**, 124927 (2020). https://doi.org/10.1016/j.chemosphere.2019.124927

126. Y. Li, W. Ho, K. Lv, B. Zhu, S.C. Lee, Carbon vacancy-induced enhancement of the visible light-driven photocatalytic oxidation of NO over g-C_3N_4 nanosheets. Appl. Surf. Sci. **430**, 380–389 (2018). https://doi.org/10.1016/j.apsusc.2017.06.054

127. Y. Zhao, Y. Liu, Z. Wang, Y. Ma, Y. Zhou et al., Carbon nitride assisted 2D conductive metal-organic frameworks composite photocatalyst for efficient visible light-driven H_2O_2 production. Appl. Catal. B **289**, 120035 (2021). https://doi.org/10.1016/j.apcatb.2021.120035

128. A. Fujishima, K. Honda, Electrochemical photolysis of water at a semiconductor electrode. Nature **238**, 37 (1972). https://doi.org/10.1038/238037a0

129. A. Fujishima, T.N. Rao, D.A. Tryk, Titanium dioxide photocatalysis. J. Photochem. Photobiol. C **1**, 1–21 (2000). https://doi.org/10.1016/S1389-5567(00)00002-2

130. H. Goto, Y. Hanada, T. Ohno, M. Matsumura, Quantitative analysis of superoxide ion and hydrogen peroxide produced from molecular oxygen on photoirradiated TiO$_2$ particles. J.

Catal. **225**, 223–229 (2004). https://doi.org/10.1016/j.jcat.2004.04.001

131. T. Baran, S. Wojtyla, A. Minguzzi, S. Rondinini, A. Vertova, Achieving efficient H_2O_2 production by a visible-light absorbing, highly stable photosensitized TiO_2. Appl. Catal. B **244**, 303–312 (2019). https://doi.org/10.1016/j.apcatb.2018.11.044

132. B.O. Burek, D.W. Bahnemann, J.Z. Bloh, Modeling and optimization of the photocatalytic reduction of molecular oxygen to hydrogen peroxide over titanium dioxide. ACS Catal. **9**, 25–37 (2019). https://doi.org/10.1021/acscatal.8b03638

133. M. Teranishi, S.-I. Naya, H. Tada, In-situ liquid phase synthesis of hydrogen peroxide from molecular oxygen using gold nanoparticle-loaded titanium(IV) dioxide photocatalyst. J. Am. Chem. Soc. **132**, 7850 (2010). https://doi.org/10.1021/ja102651g

134. X.Z. Li, C.C. Chen, J.C. Zhao, Mechanism of photodecomposition of H_2O_2 on TiO_2 surfaces under visible light irradiation. Langmuir **17**, 4118–4122 (2001). https://doi.org/10.1021/la010035s

135. M. Teranishi, R. Hoshino, S.-I. Naya, H. Tada, Gold-nanoparticle-loaded carbonate-modified titanium(IV) oxide surface: visible-light-driven formation of hydrogen peroxide from oxygen. Angew. Chem. Int. Ed. **55**, 12773–12777 (2016). https://doi.org/10.1002/anie.201606734

136. M. Teranishi, S.-I. Naya, H. Tada, Temperature- and pH-dependence of hydrogen peroxide formation from molecular oxygen by gold nanoparticle-loaded titanium(IV) oxide photocatalyst. J. Phys. Chem. C **120**, 1083–1088 (2016). https://doi.org/10.1021/acs.jpcc.5b10626

137. R. Miah, T. Ohsaka, Cathodic detection of H_2O_2 using iodide-modified gold electrode in alkaline media. Anal. Chem. **78**, 1200–1205 (2006). https://doi.org/10.1021/ac0515935

138. T. Hirakawa, K. Yawata, Y. Nosaka, Photocatalytic reactivity for $O_2^{·-}$ and OH· radical formation in anatase and rutile TiO_2 suspension as the effect of H_2O_2 addition. Appl. Catal. A **325**, 105–111 (2007). https://doi.org/10.1016/j.apcata.2007.03.015

139. D. Tsukamoto, A. Shiro, Y. Shiraishi, Y. Sugano, S. Ichikawa et al., Photocatalytic H_2O_2 production from ethanol/O_2 system using TiO_2 loaded with Au-Ag bimetallic alloy nanoparticles. ACS Catal. **2**, 599–603 (2012). https://doi.org/10.1021/cs2006873

140. E.M. Goliaei, N. Seriani, Structure and electronic properties of small silver-gold clusters on titania photocatalysts for H_2O_2 production: an investigation with density functional theory. J. Phys. Chem. C **123**, 2855–2863 (2019). https://doi.org/10.1021/acs.jpcc.8b09300

141. X.T. Zheng, A. Ananthanarayanan, K.Q. Luo, P. Chen, Glowing graphene quantum dots and carbon dots: properties, syntheses, and biological applications. Small **11**, 1620–1636 (2015). https://doi.org/10.1002/smll.201402648

142. Q. Mei, K. Zhang, G. Guan, B. Liu, S. Wang et al., Highly efficient photoluminescent graphene oxide with tunable surface properties. Chem. Commun. **46**, 7319–7321 (2010). https://doi.org/10.1039/c0cc02374d

143. L. Zheng, H. Su, J. Zhang, L.S. Walekar, H.V. Molamahmood et al., Highly selective photocatalytic production of H_2O_2 on sulfur and nitrogen for co-doped graphene quantum dots tuned TiO_2. Appl. Catal. B **239**, 475–484 (2018). https://doi.org/10.1016/j.apcatb.2018.08.031

144. L. Zheng, J. Zhang, Y.H. Hu, M. Long, Enhanced photocatalytic production of H_2O_2 by nafion coatings on S, N-codoped graphene-quantum-dots-modified TiO_2. J. Phys. Chem. C **123**, 13693–13701 (2019). https://doi.org/10.1021/acs.jpcc.9b02311

145. R.X. Cai, Y. Kubota, A. Fujishima, Effect of copper ions on the formation of hydrogen peroxide from photocatalytic titanium dioxide particles. J. Catal. **219**, 214–218 (2003). https://doi.org/10.1016/S0021-9517(03)00197-0

146. V. Maurino, C. Minero, E. Pelizzetti, G. Mariella, A. Arbezzano et al., Influence of Zn (II) adsorption on the photocatalytic activity and the production of H_2O_2 over irradiated TiO_2. Res. Chem. Intermed. **33**, 319–332 (2007). https://doi.org/10.1163/156856707779238711

147. V. Maurino, C. Minero, G. Mariella, E. Pelizzetti, Sustained production of H_2O_2 on irradiated TiO_2 - fluoride systems. Chem. Commun. (2005). https://doi.org/10.1039/b418789j

148. Y. Shiraishi, S. Kanazawa, D. Tsukamoto, A. Shiro, Y. Sugano et al., Selective hydrogen peroxide formation by titanium dioxide photocatalysis with benzylic alcohols and molecular oxygen in water. ACS Catal. **3**, 2222–2227 (2013). https://doi.org/10.1021/cs400511q

149. G. Zuo, B. Li, Z. Guo, L. Wang, F. Yang et al., Efficient photocatalytic hydrogen peroxide production over TiO_2 passivated by SnO_2. Catalysts **9**, 623 (2019). https://doi.org/10.3390/catal9070623

150. K. Awa, S.-I. Naya, M. Fujishima, H. Tada, A three-component plasmonic photocatalyst consisting of gold nanoparticle and TiO_2-SnO_2 nanohybrid with heteroepitaxial junction: hydrogen peroxide synthesis. J. Phys. Chem. C **124**, 7797–7802 (2020). https://doi.org/10.1021/acs.jpcc.9b11875

151. M. Nagamitsu, K. Awa, H. Tada, Hydrogen peroxide synthesis from water and oxygen using a three-component nanohybrid photocatalyst consisting of Au particle-loaded rutile TiO_2 and RuO_2 with a heteroepitaxial junction. Chem. Commun. **56**, 8190–8193 (2020). https://doi.org/10.1039/d0cc03327h

152. C. Chu, D. Huang, Q. Zhu, E. Stavitski, J.A. Spies et al., Electronic tuning of metal nanoparticles for highly efficient photocatalytic hydrogen peroxide production. ACS Catal. **9**, 626–631 (2019). https://doi.org/10.1021/acscatal.8b03738

153. R. Ma, L. Wang, H. Wang, Z. Liu, M. Xing et al., Solid acids accelerate the photocatalytic hydrogen peroxide synthesis over a hybrid catalyst of Titania nanotube with carbon dot. Appl. Catal. B **244**, 594–603 (2019). https://doi.org/10.1016/j.apcatb.2018.11.087

154. X. Wu, X. Zhang, S. Zhao, Y. Gong, R. Djellabi et al., Highly-efficient photocatalytic hydrogen peroxide production

over polyoxometalates covalently immobilized onto titanium dioxide. Appl. Catal. A **591**, 117271 (2020). https://doi.org/10.1016/j.apcata.2019.117271

155. G.-H. Moon, W. Kim, A.D. Bokare, N.-E. Sung, W. Choi, Solar production of H_2O_2 on reduced graphene oxide-TiO$_2$ hybrid photocatalysts consisting of earth-abundant elements only. Energy Environ. Sci. **7**, 4023–4028 (2014). https://doi.org/10.1039/c4ee02757d

156. R. He, D. Xu, B. Cheng, J. Yu, W. Ho, Review on nanoscale Bi-based photocatalysts. Nanoscale Horiz. **3**, 464–504 (2018). https://doi.org/10.1039/c8nh00062j

157. L. Huang, Z. Duan, Y. Song, Q. Li, L. Chen, $BiVO_4$ microplates with oxygen vacancies decorated with metallic Cu and Bi nanoparticles for CO_2 photoreduction. ACS Appl. Nano Mater. **4**, 3576–3585 (2021). https://doi.org/10.1021/acsanm.1c00115

158. J.H. Kim, J.S. Lee, Elaborately modified $BiVO_4$ photoanodes for solar water splitting. Adv. Mater. **31**, 1806938 (2019). https://doi.org/10.1002/adma.201806938

159. W. Zhao, Y. Feng, H. Huang, P. Zhou, J. Li et al., A novel Z-scheme Ag_3VO_4/$BiVO_4$ heterojunction photocatalyst: study on the excellent photocatalytic performance and photocatalytic mechanism. Appl. Catal. B **245**, 448–458 (2019). https://doi.org/10.1016/j.apcatb.2019.01.001

160. T. Hirakawa, Y. Nosaka, Selective production of superoxide ions and hydrogen peroxide over nitrogen- and sulfur-doped TiO_2 photocatalysts with visible light in aqueous suspension systems. J. Phys. Chem. C **112**, 15818–15823 (2008). https://doi.org/10.1021/jp8055015

161. M.A. Henderson, A surface science perspective on TiO_2 photocatalysis. Surf. Sci. Rep. **66**, 185–297 (2011). https://doi.org/10.1016/j.surfrep.2011.01.001

162. A. Kudo, K. Omori, H. Kato, A novel aqueous process for preparation of crystal form-controlled and highly crystalline $BiVO_4$ powder from layered vanadates at room temperature and its photocatalytic and photophysical properties. J. Am. Chem. Soc. **121**, 11459–11467 (1999). https://doi.org/10.1021/ja992541y

163. H. Hirakawa, S. Shiota, Y. Shiraishi, H. Sakamoto, S. Ichikawa et al., Au nanoparticles supported on $BiVO_4$: effective inorganic photocatalysts for H_2O_2 production from water and O_2 under visible light. ACS Catal. **6**, 4976–4982 (2016). https://doi.org/10.1021/acscatal.6b01187

164. V. Kumar, S. O'Donnell, B. Zoellner, J. Martinez, G. Wang et al., Interfacing plasmonic nanoparticles with ferroelectrics for hot-carrier-driven photocatalysis: impact of schottky barrier height. ACS Appl. Energy Mater. **2**, 7690–7699 (2019). https://doi.org/10.1021/acsaem.9b01682

165. X. Chen, R.T. Pekarek, J. Gu, A. Zakutayev, K.E. Hurst et al., Transient evolution of the built-in field at junctions of GaAs. ACS Appl. Mater. Interfaces **12**, 40339–40346 (2020). https://doi.org/10.1021/acsami.0c11474

166. K. Wang, M. Wang, J. Yu, D. Liao, H. Shi et al., $BiVO_4$ microparticles decorated with Cu @Au core-shell nanostructures for photocatalytic H_2O_2 production. ACS Appl.

Nano Mater. **4**, 13158–13166 (2021). https://doi.org/10.1021/acsanm.1c02688

167. M. Teranishi, T. Kunimoto, S.-I. Naya, H. Kobayashi, H. Tada, Visible-light-driven hydrogen peroxide synthesis by a hybrid photocatalyst consisting of bismuth vanadate and bis(hexafluoroacetylacetonato)copper (II) complex. J. Phys. Chem. C **124**, 3715–3721 (2020). https://doi.org/10.1021/acs.jpcc.9b11568

168. Q. Li, X. Li, S. Wageh, A.A. Al-Ghamdi, J. Yu, CdS/graphene nanocomposite photocatalysts. Adv. Energy Mater. **5**, 1500010 (2015). https://doi.org/10.1002/aenm.201500010

169. A. Kudo, Y. Miseki, Heterogeneous photocatalyst materials for water splitting. Chem. Soc. Rev. **38**, 253–278 (2009). https://doi.org/10.1039/b800489g

170. Y. Xu, M.A.A. Schoonen, The absolute energy positions of conduction and valence bands of selected semiconducting minerals. Am. Mineral. **85**, 543–556 (2000). https://doi.org/10.2138/am-2000-0416

171. Q. Li, B. Guo, J. Yu, J. Ran, B. Zhang et al., Highly efficient visible-light-driven photocatalytic hydrogen production of CdS-cluster-decorated graphene nanosheets. J. Am. Chem. Soc. **133**, 10878–10884 (2011). https://doi.org/10.1021/ja2025454

172. S. Thakur, T. Kshetri, N.H. Kim, J.H. Lee, Sunlight-driven sustainable production of hydrogen peroxide using a CdS-graphene hybrid photocatalyst. J. Catal. **345**, 78–86 (2017). https://doi.org/10.1016/j.jcat.2016.10.028

173. D. Stone, Y. Ben-Shahar, N. Waiskopf, U. Banin, The metal type governs photocatalytic reactive oxygen species formation by semiconductor-metal hybrid nanoparticles. ChemCatChem **10**, 5119–5123 (2018). https://doi.org/10.1002/cctc.201801306

174. J.H. Lee, H. Cho, S.O. Park, J.M. Hwang, Y. Hong et al., High performance H_2O_2 production achieved by sulfur-doped carbon on CdS photocatalyst via inhibiting reverse H_2O_2 decomposition. Appl. Catal. B **284**, 119690 (2021). https://doi.org/10.1016/j.apcatb.2020.119690

175. J. Lee, O.K. Farha, J. Roberts, K.A. Scheidt, S.T. Nguyen et al., Metal-organic framework materials as catalysts. Chem. Soc. Rev. **38**, 1450–1459 (2009). https://doi.org/10.1039/b807080f

176. H. Wang, X. Yuan, Y. Wu, G. Zeng, X. Chen et al., Synthesis and applications of novel graphitic carbon nitride/metal-organic frameworks mesoporous photocatalyst for dyes removal. Appl. Catal. B **174**, 445–454 (2015). https://doi.org/10.1016/j.apcatb.2015.03.037

177. R. Li, W. Zhang, K. Zhou, Metal-organic-framework-based catalysts for photoreduction of CO_2. Adv. Mater. **30**, 1705512 (2018). https://doi.org/10.1002/adma.201705512

178. J. Qiu, X. Zhang, Y. Feng, X. Zhang, H. Wang et al., Modified metal-organic frameworks as photocatalysts. Appl. Catal. B **231**, 317–342 (2018). https://doi.org/10.1016/j.apcatb.2018.03.039

179. J. Guo, Y. Wan, Y. Zhu, M. Zhao, Z. Tang et al., Advanced photocatalysts based on metal nanoparticle/metal-organic

framework composites. Nano Res. **14**, 2037–2052 (2021). https://doi.org/10.1007/s12274-020-3182-1

180. Y. Isaka, Y. Kondo, Y. Kawase, Y. Kuwahara, K. Mori et al., Photocatalytic production of hydrogen peroxide through selective two-electron reduction of dioxygen utilizing amine-functionalized MIL-125 deposited with nickel oxide nanoparticles. Chem. Commun. **54**, 9270–9273 (2018). https://doi.org/10.1039/c8cc02679c

181. Y. Isaka, Y. Kawase, Y. Kuwahara, K. Mori, H. Yamashita et al., Two-phase system utilizing hydrophobic metal-organic frameworks (MOFs) for photocatalytic synthesis of hydrogen peroxide. Angew. Chem. Int. Ed. **58**, 5402–5406 (2019). https://doi.org/10.1002/anie.201901961

182. Y. Kawase, Y. Isaka, Y. Kuwahara, K. Mori, H. Yamashita et al., Ti cluster-alkylated hydrophobic MOFs for photocatalytic production of hydrogen peroxide in two-phase systems. Chem. Commun. **55**, 6743–6746 (2019). https://doi.org/10.1039/c9cc02380a

183. X. Chen, Y. Kuwahara, K. Mori, C. Louis, H. Yamashita, A hydrophobic titanium doped zirconium-based metal organic framework for photocatalytic hydrogen peroxide production in a two-phase system. J. Mater. Chem. A **8**, 1904–1910 (2020). https://doi.org/10.1039/c9ta11120d

184. J.-D. Xiao, L. Han, J. Luo, S.-H. Yu, H.-L. Jiang et al., Integration of plasmonic effects and schottky junctions into metal-organic framework composites: steering charge flow for enhanced visible-light photocatalysis. Angew. Chem. Int. Ed. **57**, 1103–1107 (2018). https://doi.org/10.1002/anie.201711725

185. C. Liu, Q. Sun, L. Lin, J. Wang, C. Zhang et al., Ternary MOF-on-MOF heterostructures with controllable architectural and compositional complexity via multiple selective assembly. Nat. Commun. **11**, 4971 (2020). https://doi.org/10.1038/s41467-020-18776-z

186. J. Ran, J. Qu, H. Zhang, T. Wen, H. Wang et al., 2D metal organic framework nanosheet: a universal platform promoting highly efficient visible-light-induced hydrogen production. Adv. Energy Mater. **9**, 1803402 (2019). https://doi.org/10.1002/aenm.201803402

187. C. Liu, T. Bao, L. Yuan, C. Zhang, J. Wang et al., Semiconducting MOF@ZnS heterostructures for photocatalytic hydrogen peroxide production: heterojunction coverage matters. Adv. Funct. Mater. **32**, 2111404 (2022). https://doi.org/10.1002/adfm.202111404

188. S. Chen, T. Luo, X. Li, K. Chen, J. Fu et al., Identification of the highly active Co-N$_4$ coordination motif for selective oxygen reduction to hydrogen peroxide. J. Am. Chem. Soc. **144**, 14505–14516 (2022). https://doi.org/10.1021/jacs.2c019414505

189. X. Li, S. Tang, S. Dou, H.J. Fan, T.S. Choksi et al., Molecule confined isolated metal sites enable the electrocatalytic synthesis of hydrogen peroxide. Adv. Mater. **34**, 2104891 (2022). https://doi.org/10.1002/adma.202104891

190. J. Wu, M. Hou, Z. Chen, W. Hao, X. Pan et al., Composition engineering of amorphous nickel boride nanoarchitectures enabling highly efficient electrosynthesis of hydrogen

191. peroxide. Adv. Mater. **34**, 2202995 (2022). https://doi.org/10.1002/adma.202202995

191. P.T. Smith, Y. Kim, B.P. Benke, K. Kim, C.J. Chang, Supramolecular tuning enables selective oxygen reduction catalyzed by cobalt porphyrins for direct electrosynthesis of hydrogen peroxide. Angew. Chem. Int. Ed. **59**, 4902–4907 (2020). https://doi.org/10.1002/anie.201916131

192. J.Y. Zhang, C.A. Xia, H.F. Wang, C. Tang, Recent advances in electrocatalytic oxygen reduction for on-site hydrogen peroxide synthesis in acidic media. J. Energy Chem. **67**, 432–450 (2022). https://doi.org/10.1016/j.jechem.2021.10.013

193. S. Yang, A. Verdaguer-Casadevall, L. Arnarson, L. Silvio, V. Colic et al., Toward the decentralized electrochemical production of H$_2$O$_2$: a focus on the catalysis. ACS Catal. **8**, 4064–4081 (2018). https://doi.org/10.1021/acscatal.8b00217

194. A.W.E. Chan, R. Hoffmann, W. Ho, Theoretical aspects of photoinitiated chemisorption, dissociation, and desorption of oxygen on platinum (111). Langmuir **8**, 1111–1119 (1992). https://doi.org/10.1021/la00040a017

195. X. Song, N. Li, H. Zhang, H. Wang, L. Wang et al., Promotion of hydrogen peroxide production on graphene-supported atomically dispersed platinum: effects of size on oxygen reduction reaction pathway. J. Power Sources **435**, 226771 (2019). https://doi.org/10.1016/j.jpowsour.2019.226771

196. S. Yang, J. Kim, Y.J. Tak, A. Soon, H. Lee, Single-atom catalyst of platinum supported on titanium nitride for selective electrochemical reactions. Angew. Chem. Int. Ed. **55**, 2058–2062 (2016). https://doi.org/10.1002/anie.201509241

197. C.H. Choi, M. Kim, H.C. Kwon, S.J. Cho, S. Yun et al., Tuning selectivity of electrochemical reactions by atomically dispersed platinum catalyst. Nat. Commun. **7**, 10922 (2016). https://doi.org/10.1038/ncomms10922

198. S. Yang, Y.J. Tak, J. Kim, A. Soon, H. Lee, Support effects in single-atom platinum catalysts for electrochemical oxygen reduction. ACS Catal. **7**, 1301–1307 (2017). https://doi.org/10.1021/acscatal.6b02899

199. R.-Q. Zhang, T.-H. Lee, B.-D. Yu, C. Stampfl, A. Soon, The role of titanium nitride supports for single-atom platinum-based catalysts in fuel cell technology. Phys. Chem. Chem. Phys. **14**, 16552–16557 (2012). https://doi.org/10.1039/c2cp41392b

200. C.H. Choi, H.C. Kwon, S. Yook, H. Shin, H. Kim et al., Hydrogen peroxide synthesis via enhanced two-electron oxygen reduction pathway on carbon-coated Pt surface. J. Phys. Chem. C **118**, 30063–30070 (2014). https://doi.org/10.1021/jp5113894

201. Q. Chang, P. Zhang, A.H.B. Mostaghimi, X. Zhao, S.R. Denny et al., Promoting H$_2$O$_2$ production via 2-electron oxygen reduction by coordinating partially oxidized Pd with defect carbon. Nat. Commun. **11**, 2178 (2020). https://doi.org/10.1038/s41467-020-15843-3

202. M. Ledendecker, E. Pizzutilo, G. Malta, G.V. Fortunato, K.J.J. Mayrhofer et al., Isolated Pd sites as selective catalysts for electrochemical and direct hydrogen peroxide synthesis.

ACS Catal. **10**, 5928–5938 (2020). https://doi.org/10.1021/acscatal.0c01305

203. Y.L. Wang, S. Gurses, N. Felyey, A. Boubnov, S.S. Mao et al., In-situ deposition of Pd during oxygen reduction yields highly selective and active electrocatalysts for direct H_2O_2 production. ACS Catal. **9**, 8453–8463 (2019). https://doi.org/10.1021/acscatal.9b01758

204. D. Mei, Z.D. He, Y.L. Zheng, D.C. Jiang, Y.-X. Chen et al., Mechanistic and kinetic implications on the ORR on an Au (100) electrode: pH, temperature and H-D kinetic isotope effects. Phys. Chem. Chem. Phys. **16**, 13762–13773 (2014). https://doi.org/10.1039/c4cp00257a

205. Y. Lu, Y. Jiang, X. Gao, W. Chen, Charge state-dependent catalytic activity of $[Au_{25}(SC_{12}H_{25})_{18}]$ nanoclusters for the two-electron reduction of dioxygen to hydrogen peroxide. Chem. Commun. **50**, 8464–8467 (2014). https://doi.org/10.1039/c4cc01841a

206. H. Tsunoyama, N. Ichikuni, H. Sakurai, T. Tsukuda, Effect of electronic structures of Au clusters stabilized by poly (N-vinyl-2-pyrrolidone) on aerobic oxidation catalysis. J. Am. Chem. Soc. **131**, 7086–7093 (2009). https://doi.org/10.1021/ja810045y

207. S. Siahrostami, A. Verdaguer-Casdevall, M. Karamad, I. Chorkendorff, I. Stephens et al., Activity and selectivity for O_2 Reduction to H_2O_2 on transition metal surfaces. ECS Trans. **58**, 53–62 (2013). https://doi.org/10.1149/05802.0053ecst

208. J.S. Jirkovsky, I. Panas, E. Ahlberg, M. Halasa, S. Romani et al., Single atom hot-spots at Au-Pd nanoalloys for electrocatalytic H_2O_2 production. J. Am. Chem. Soc. **133**, 19432–19441 (2011). https://doi.org/10.1021/ja206477z

209. A. Verdaguer-Casadevall, D. Deiana, M. Karamad, S. Siahrostami, P. Malacrida et al., Trends in the electrochemical synthesis of H_2O_2: enhancing activity and selectivity by electrocatalytic site engineering. Nano Lett. **14**, 1603–1608 (2014). https://doi.org/10.1021/nl500037x

210. E. Pizzutilo, O. Kasian, C.H. Choi, S. Cherevko, G.J. Hutchings et al., Electrocatalytic synthesis of hydrogen peroxide on Au-Pd nanoparticles: from fundamentals to continuous production. Chem. Phys. Lett. **683**, 436–442 (2017). https://doi.org/10.1016/j.cplett.2017.01.071

211. Y. Dong, J. Su, S. Zhou, M. Wang, S. Huang et al., Carbon-based dots for the electrochemical production of hydrogen peroxide. Chem. Commun. **56**, 7609–7612 (2020). https://doi.org/10.1039/c9cc09987e

212. Y.-L. Wang, S.-S. Li, X.-H. Yang, G.-Y. Xu, Z.-C. Zhu et al., One minute from pristine carbon to an electrocatalyst for hydrogen peroxide production. J. Mater. Chem. A **7**, 21329–21337 (2019). https://doi.org/10.1039/c9ta04788c

213. V. Colic, S. Yang, Z. Revay, I.E.L. Stephens, I. Chorkendorff, Carbon catalysts for electrochemical hydrogen peroxide production in acidic media. Electrochim. Acta **272**, 192–202 (2018). https://doi.org/10.1016/j.electacta.2018.03.170

214. Y. Bu, Y. Wang, G.-F. Han, Y. Zhao, X. Ge et al., Carbon-based electrocatalysts for efficient hydrogen peroxide

215. Y. Liu, X. Quan, X. Fan, H. Wang, S. Chen, High-yield electrosynthesis of hydrogen peroxide from oxygen reduction by hierarchically porous carbon. Angew. Chem. Int. Ed. **54**, 6837–6841 (2015). https://doi.org/10.1002/anie.201502396

216. L. Tao, Q. Wang, S. Dou, Z. Ma, J. Huo et al., Edge-rich and dopant-free graphene as a highly efficient metal-free electrocatalyst for the oxygen reduction reaction. Chem. Commun. **52**, 2764–2767 (2016). https://doi.org/10.1039/c5cc09173j

217. S. Chen, Z. Chen, S. Siahrostami, T.R. Kim, D. Nordlund et al., Defective carbon-based materials for the electrochemical synthesis of hydrogen peroxide. ACS Sustainable Chem. Eng. **6**, 311–317 (2018). https://doi.org/10.1021/acssuschemeng.7b02517

218. Y.J. Sa, J.H. Kim, S.H. Joo, Active edge-site-rich carbon nanocatalysts with enhanced electron transfer for efficient electrochemical hydrogen peroxide production. Angew. Chem. Int. Ed. **58**, 1100–1105 (2019). https://doi.org/10.1002/anie.201812435

219. M. Yeddala, P. Thakur, A. Anugraha, T.N. Narayanan, Electrochemically derived functionalized graphene for bulk production of hydrogen peroxide. Beilstein J. Nanotechnol. **11**, 432–442 (2020). https://doi.org/10.3762/bjnano.11.34

220. X. Xu, D. Kong, J. Liang, Y. Gao, Q. Yang et al., Bottom-up construction of microporous catalyst with identical active sites for efficient hydrogen peroxide production. Carbon **171**, 931–937 (2021). https://doi.org/10.1016/j.carbon.2020.09.080

221. H.W. Kim, M.B. Ross, N. Kornienko, L. Zhang, J.H. Guo et al., Efficient hydrogen peroxide generation using reduced graphene oxide-based oxygen reduction electrocatalysts. Nat. Catal. **1**, 282–290 (2018). https://doi.org/10.1038/s41929-018-0044-2

222. W. Wang, Y. Hu, Y. Liu, Z. Zheng, S. Chen, Self-powered and highly efficient production of H_2O_2 through a Zn-air battery with oxygenated carbon electrocatalyst. ACS Appl. Mater. Interfaces **10**, 31855–31859 (2018). https://doi.org/10.1021/acsami.8b11703

223. H. Zhang, Y. Li, Y. Zhao, G. Li, F. Zhang, Carbon black oxidized by air calcination for enhanced H_2O_2 generation and effective organics degradation. ACS Appl. Mater. Interfaces **11**, 27846–27853 (2019). https://doi.org/10.1021/acsami.9b07765

224. J. Zhu, X. Xiao, K. Zheng, F. Li, G. Ma et al., KOH-treated reduced graphene oxide: 100% selectivity for H_2O_2 electroproduction. Carbon **153**, 6–11 (2019). https://doi.org/10.1016/j.carbon.2019.07.009

225. G.-F. Han, F. Li, W. Zou, M. Karamad, J.-P. Jeon et al., Building and identifying highly active oxygenated groups in carbon materials for oxygen reduction to H_2O_2. Nat. Commun. **11**, 2209 (2020). https://doi.org/10.1038/s41467-020-15782-z

226. Y. Xue, X. Du, W. Cai, Z. Sun, Y. Zhang et al., Ramie biomass derived nitrogen-doped activated carbon for efficient electrocatalytic production of hydrogen peroxide. J.

Electrochem. Soc. **165**, E171–E176 (2018). https://doi.org/10.1149/2.0681805jes

227. Y.-H. Lee, F. Li, K.-H. Chang, C.-C. Hu, T. Ohsaka, Novel synthesis of N-doped porous carbons from collagen for electrocatalytic production of H_2O_2. Appl. Catal. B **126**, 208–214 (2012). https://doi.org/10.1016/j.apcatb.2012.06.031

228. J. Zhang, G. Zhang, S. Jin, Y. Zhou, Q. Ji et al., Graphitic N in nitrogen-doped carbon promotes hydrogen peroxide synthesis from electrocatalytic oxygen reduction. Carbon **163**, 154–161 (2020). https://doi.org/10.1016/j.carbon.2020.02.084

229. L. Han, Y. Sun, S. Li, C. Cheng, C.E. Halbig et al., In-plane carbon lattice-defect regulating electrochemical oxygen reduction to hydrogen peroxide production over nitrogen-doped graphene. ACS Catal. **9**, 1283–1288 (2019). https://doi.org/10.1021/acscatal.8b03734

230. V. Perazzolo, C. Durante, R. Pilot, A. Paduano, J. Zheng et al., Nitrogen and sulfur doped mesoporous carbon as metal-free electrocatalysts for the in-situ production of hydrogen peroxide. Carbon **95**, 949–963 (2015). https://doi.org/10.1016/j.carbon.2015.09.002

231. D.-W. Wang, D. Su, Heterogeneous nanocarbon materials for oxygen reduction reaction. Energy Environ. Sci. **7**, 576–591 (2014). https://doi.org/10.1039/c3ee43463j

232. D. Iglesias, A. Giuliani, M. Melchionna, S. Marchesan, A. Criado et al., N-doped graphitized carbon nanohorns as a forefront electrocatalyst in highly selective O_2 reduction to H_2O_2. Chem **4**, 106–123 (2018). https://doi.org/10.1016/j.chempr.2017.10.013

233. K. Gong, F. Du, Z. Xia, M. Durstock, L. Dai, Nitrogen-doped carbon nanotube arrays with high electrocatalytic activity for oxygen reduction. Science **323**, 760–764 (2009). https://doi.org/10.1126/science.1168049

234. X. Liu, L. Dai, Carbon-based metal-free catalysts. Nat. Rev. Mater. **1**, 16064 (2016). https://doi.org/10.1038/natrevmats.2016.64

235. L. Dai, Y. Xue, L. Qu, H.-J. Choi, J.-B. Baek, Metal-free catalysts for oxygen reduction reaction. Chem. Rev. **115**, 4823–4892 (2015). https://doi.org/10.1021/cr5003563

236. T.-P. Fellinger, F. Hasche, P. Strasser, M. Antonietti, Mesoporous nitrogen-doped carbon for the electrocatalytic synthesis of hydrogen peroxide. J. Am. Chem. Soc. **134**, 4072–4075 (2012). https://doi.org/10.1021/ja300038p

237. J. Park, Y. Nabae, T. Hayakawa, M.-A. Kakimoto, Highly selective two-electron oxygen reduction catalyzed by mesoporous nitrogen-doped carbon. ACS Catal. **4**, 3749–3754 (2014). https://doi.org/10.1021/cs5008206

238. Y. Sun, I. Sinev, W. Ju, A. Bergmann, S. Dresp et al., Efficient electrochemical hydrogen peroxide production from molecular oxygen on nitrogen-doped mesoporous carbon catalysts. ACS Catal. **8**, 2844–2856 (2018). https://doi.org/10.1021/acscatal.7b03464

239. J. Li, C. Shi, A. Bao, J. Jia, Development of boron-doped mesoporous carbon materials for use in CO_2 capture and electrochemical generation of H_2O_2. ACS Omega **6**, 8438–8446 (2021). https://doi.org/10.1021/acsomega.1c00197

240. G. Chen, J. Liu, Q. Li, P. Guan, X. Yu et al., A direct H_2O_2 production based on hollow porous carbon sphere-sulfur nanocrystal composites by confinement effect as oxygen reduction electrocatalysts. Nano Res. **12**, 2614–2622 (2019). https://doi.org/10.1007/s12274-019-2496-3

241. S. Chen, Z. Chen, S. Siahrostami, D. Higgins, D. Nordlund et al., Designing boron nitride islands in carbon materials for efficient electrochemical synthesis of hydrogen peroxide. J. Am. Chem. Soc. **140**, 7851–7859 (2018). https://doi.org/10.1021/jacs.8b02798

242. X.-H. Yan, Z. Meng, J. Liu, T. Xue, Sodium ferric EDTA-derived Fe-N-C material for selectively electrocatalytic synthesis of hydrogen peroxide. Mater. Lett. **217**, 171–173 (2018). https://doi.org/10.1016/j.matlet.2018.01.044

243. A. Byeon, J. Cho, J.G.M. Kim, K.H. Chae, H.-Y. Park et al., High-yield electrochemical hydrogen peroxide production from an enhanced two-electron oxygen reduction pathway by mesoporous nitrogen-doped carbon and manganese hybrid electrocatalysts. Nanoscale Horiz. **5**, 832–838 (2020). https://doi.org/10.1039/c9nh00783k

244. M. Suk, M.W. Chung, M.H. Han, H.-S. Oh, C.H. Choi et al., Selective H_2O_2 production on surface-oxidized metal-nitrogen-carbon electrocatalysts. Catal. Today **359**, 99–105 (2021). https://doi.org/10.1016/j.cattod.2019.05.034

245. B. You, N. Jiang, M. Sheng, W.S. Drisdell, J. Yano et al., Bimetal-organic framework self-adjusted synthesis of support-free nonprecious electrocatalysts for efficient oxygen reduction. ACS Catal. **5**, 7068–7076 (2015). https://doi.org/10.1021/acscatal.5b02325

246. J. Gao, H.B. Yang, X. Huang, S.-F. Hung, W. Cai et al., Enabling direct H_2O_2 production in acidic media through rational design of transition metal single atom catalyst. Chem **6**, 658–674 (2020). https://doi.org/10.1016/j.chempr.2019.12.008

247. Y. Sun, L. Silvioli, N.R. Sahraie, W. Ju, J. Li et al., Activity-selectivity trends in the electrochemical production of hydrogen peroxide over single-site metal-nitrogen-carbon catalysts. J. Am. Chem. Soc. **141**, 12372–12381 (2019). https://doi.org/10.1021/jacs.9b05576

248. E. Jung, H. Shin, B.-H. Lee, V. Efremov, S. Lee et al., Atomic-level tuning of Co-N-C catalyst for high-performance electrochemical H_2O_2 production. Nat. Mater. (2020). https://doi.org/10.1038/s41563-019-0571-5

249. M. Jin, W. Liu, J. Sun, X. Wang, S. Zhang et al., Highly dispersed Ag clusters for active and stable hydrogen peroxide production. Nano Res. **15**, 5842–5847 (2022). https://doi.org/10.1007/s12274-022-4208-7

250. Z. Zheng, Y.H. Ng, D.-W. Wang, R. Amal, Epitaxial growth of Au-Pt-Ni nanorods for direct high selectivity H_2O_2 production. Adv. Mater. **28**, 9949–9955 (2016). https://doi.org/10.1002/adma.201603662

251. S. Chen, T. Luo, K. Chen, Y. Lin, J. Fu et al., Chemical identification of catalytically active sites on oxygen-doped carbon nanosheet to decipher the high activity for electro-synthesis hydrogen peroxide. Angew. Chem. Int. Ed. **60**, 16607–16614 (2021). https://doi.org/10.1002/anie.202104480

252. Z. Deng, X. Wang, Mechanism investigation of enhanced electrochemical H_2O_2 production performance on oxygen-rich hollow porous carbon spheres. Nano Res. **15**, 4599–4605 (2022). https://doi.org/10.1007/s12274-022-4095-y

253. Y. Sun, S. Li, Z.P. Jovanov, D. Bernsmeier, P. Strasser et al., structure, activity, and faradaic efficiency of nitrogen-doped porous carbon catalysts for direct electrochemical hydrogen peroxide production. Chemsuschem **11**, 3388–3395 (2018). https://doi.org/10.1002/cssc.201801583

254. Y. Hu, J. Zhang, T. Shen, Z. Li, K. Chen et al., Efficient electrochemical production of H_2O_2 on hollow N-doped carbon nanospheres with abundant micropores. ACS Appl. Mater. Interfaces **13**, 29551–29557 (2021). https://doi.org/10.1021/acsami.1c05353

255. H. Gong, Z. Wei, Z. Gong, J. Liu, G. Ye et al., Low-coordinated Co-N-C on oxygenated graphene for efficient electrocatalytic H_2O_2 production. Adv. Funct. Mater. **32**, 2106886 (2022). https://doi.org/10.1002/adfm.202106886

256. P.-T. Thuan-Nguyen, T. Petenzi, C. Ranjan, H.N. Randriamahazaka, J. Ghilane, Microwave assisted synthesis of carbon dots in ionic liquid as metal free catalyst for highly selective production of hydrogen peroxide. Carbon **130**, 544–552 (2018). https://doi.org/10.1016/j.carbon.2018.01.070

257. L. Wang, L. Duan, L. Tong, L. Sun, Visible light-driven water oxidation catalyzed by mononuclear ruthenium complexes. J. Catal. **306**, 129–132 (2013). https://doi.org/10.1016/j.jcat.2013.06.023

258. I. Katsounaros, S. Cherevko, A.R. Zeradjanin, K.J.J. Mayrhofer, Oxygen electrochemistry as a cornerstone for sustainable energy conversion. Angew. Chem. Int. Ed. **53**, 102–121 (2014). https://doi.org/10.1002/anie.201306588

259. Z.-P. Wu, X.F. Lu, S.-Q. Zang, X.W. Lou, Non-noble-metal-based electrocatalysts toward the oxygen evolution reaction. Adv. Funct. Mater. **30**, 1910274 (2020). https://doi.org/10.1002/adfm.201910274

260. V. Viswanathan, H.A. Hansen, J.K. Norskov, Selective electrochemical generation of hydrogen peroxide from water oxidation. J. Phys. Chem. Lett. **6**, 4224–4228 (2015). https://doi.org/10.1021/acs.jpclett.5b02178

261. S. Siahrostami, G.-L. Li, V. Viswanathan, J.K. Norskov, One- or two-electron water oxidation, hydroxyl radical, or H_2O_2 evolution. J. Phys. Chem. Lett. **8**, 1157–1160 (2017). https://doi.org/10.1021/acs.jpclett.6b02924

262. X. Shi, S. Siahrostami, G.-L. Li, Y. Zhang, P. Chakthranont et al., Understanding activity trends in electrochemical water oxidation to form hydrogen peroxide. Nat. Commun. **8**, 701 (2017). https://doi.org/10.1038/s41467-017-00585-6

263. A. Nadar, S.S. Gupta, Y. Kar, S. Shetty, A.P. van Bavel et al., Evaluating the reactivity of $BiVO_4$ surfaces for efficient electrocatalytic H_2O_2 production: a combined experimental and computational study. J. Phys. Chem. C **124**, 4152–4161 (2020). https://doi.org/10.1021/acs.jpcc.9b11418

264. J.H. Baek, T.M. Gill, H. Abroshan, S. Park, X. Shi et al., Selective and efficient Gd-doped $BiVO_4$ photoanode for two-electron water oxidation to H_2O_2. ACS Energy Lett. **4**, 720–728 (2019). https://doi.org/10.1021/acsenergylett.9b00277

265. L. Li, Z. Hu, J.C. Yu, On-demand synthesis of H_2O_2 by water oxidation for sustainable resource production and organic pollutant degradation. Angew. Chem. Int. Ed. **59**, 20538–20544 (2020). https://doi.org/10.1002/anie.202008031

266. T. Kang, B. Li, Q. Hao, W. Gao, F. Bin et al., Efficient hydrogen peroxide (H_2O_2) synthesis by $CaSnO_3$ via two-electron water oxidation reaction. ACS Sustainable Chem. Eng. **8**, 15005–15012 (2020). https://doi.org/10.1021/acssuschemeng.0c05449

267. S.Y. Park, H. Abroshan, X. Shi, H.S. Jung, S. Siahrostami et al., $CaSnO_3$: an electrocatalyst for two-electron water oxidation reaction to form H_2O_2. ACS Energy Lett. **4**, 352–357 (2019). https://doi.org/10.1021/acsenergylett.8b02303

268. S.R. Kelly, X. Shi, S. Back, L. Vallez, S.Y. Park et al., ZnO as an active and selective catalyst for electrochemical water oxidation to hydrogen peroxide. ACS Catal. **9**, 4593–4599 (2019). https://doi.org/10.1021/acscatal.8b04873

269. J. Li, D. Solanki, Q. Zhu, X. Shen, G. Callander et al., Microstructural origin of selective water oxidation to hydrogen peroxide at low overpotentials: a study on Mn-alloyed TiO_2. J. Mater. Chem. A **9**, 18498–18505 (2021). https://doi.org/10.1039/d1ta05451a

270. S.-G. Xue, L. Tang, Y.-K. Tang, C.-X. Li, M.-L. Li et al., Selective electrocatalytic water oxidation to produce H_2O_2 using a C, N codoped $Ti_{O}2$ electrode in an acidic electrolyte. ACS Appl. Mater. Interfaces **12**, 4423–4431 (2020). https://doi.org/10.1021/acsami.9b16937

271. K. Fuku, Y. Miyase, Y. Miseki, T. Gunji, K. Sayama, Enhanced oxidative hydrogen peroxide production on conducting glass anodes modified with metal oxides. ChemistrySelect **1**, 5721–5726 (2016). https://doi.org/10.1002/slct.201601469

272. Y. Miyase, S. Iguchi, Y. Miseki, T. Gunji, K. Sayama, Electrochemical H_2O_2 production and accumulation from H_2O by composite effect of Al_2O_3 and $BiVO_4$. J. Electrochem. Soc. **166**, H644–H649 (2019). https://doi.org/10.1149/2.0561913jes

273. F. Kuttassery, S. Mathew, S. Sagawa, S.N. Remello, A. Thomas et al., One electron-initiated two-electron oxidation of water by aluminum porphyrins with earth's most abundant metal. Chemsuschem **10**, 1909–1915 (2017). https://doi.org/10.1002/cssc.201700322

274. S.N. Remello, F. Kuttassery, S. Mathew, A. Thomas, D. Yamamoto et al., Two-electron oxidation of water to form hydrogen peroxide catalysed by silicon-porphyrins. Sustainable Energy Fuels **2**, 1966–1973 (2018). https://doi.org/10.1039/c8se00102b

275. A. Sebastian, S.N. Remello, F. Kuttassery, S. Mathew, Y. Ohsaki et al., Protolytic behavior of water-soluble zinc (II) porphyrin and the electrocatalytic two-electron water oxidation to form hydrogen peroxide. J. Photochem. Photobiol. A **400**, 112619 (2020). https://doi.org/10.1016/j.jphotochem.2020.112619

276. Y. Ohsaki, A. Thomas, F. Kuttassery, S. Mathew, S.N. Remello et al., Two-electron oxidation of water to form hydrogen peroxide initiated by one-electron oxidation of Tin (IV)-porphyrins. J. Photochem. Photobiol. A **401**, 112732 (2020). https://doi.org/10.1016/j.jphotochem.2020.112732

277. Y. Ando, T. Tanaka, Proposal for a new system for simultaneous production of hydrogen and hydrogen peroxide by water electrolysis. Int. J. Hydrogen Energy **29**, 1349–1354 (2004). https://doi.org/10.1016/j.ijhydene.2004.02.001

278. J.V. Macpherson, A practical guide to using boron doped diamond in electrochemical research. Phys. Chem. Chem. Phys. **17**, 2935–2949 (2015). https://doi.org/10.1039/c4cp04022h

279. B. Marselli, J. Garcia-Gomez, P.A. Michaud, M.A. Rodrigo, C. Comninellis et al., Electrogeneration of hydroxyl radicals on boron-doped diamond electrodes. J. Electrochem. Soc. **150**, D79–D83 (2003). https://doi.org/10.1149/1.1553790

280. P.A. Michaud, M. Panizza, L. Ouattara, T. Diaco, G. Foti et al., Electrochemical oxidation of water on synthetic boron-doped diamond thin film anodes. J. Appl. Electrochem. **33**, 151–154 (2003). https://doi.org/10.1023/A:1024084924058

281. S. Mavrikis, M. Goeltz, S. Rosiwal, L. Wang, C. Ponce de Leon, Boron-doped diamond electrocatalyst for enhanced anodic H_2O_2 production. ACS Appl. Energy Mater. **3**, 3169–3173 (2020). https://doi.org/10.1021/acsaem.0c00093

282. S. Mavrikis, M. Goeltz, S.C. Perry, F. Bogdan, P.K. Leung et al., Effective hydrogen peroxide production from electrochemical water oxidation. ACS Energy Lett. **6**, 2369–2377 (2021). https://doi.org/10.1021/acsenergylett.1c00904

283. Irkham, A. Fiorani, G. Valenti, N. Kamoshida, F. Paolucci et al., Electrogenerated chemiluminescence by in-situ production of coreactant hydrogen peroxide in carbonate aqueous solution at a boron-doped diamond electrode. J. Am. Chem. Soc. **142**, 1518–1525 https://doi.org/10.1021/jacs.9b11842

284. K. Wenderich, B.A.M. Nieuweweme, G. Mul, B.T. Mei, Selective electrochemical oxidation of H_2O to H_2O_2 using boron-doped diamond: an experimental and techno-economic evaluation. ACS Sustainable Chem. Eng. **9**, 7803–7812 (2021). https://doi.org/10.1021/acssuschemeng.1c01244

285. I. Salmeron, K.V. Plakas, I. Sires, I. Oller, M.I. Maldonado et al., Optimization of electrocatalytic H_2O_2 production at pilot plant scale for solar-assisted water treatment. Appl. Catal. B **242**, 327–336 (2019). https://doi.org/10.1016/j.apcatb.2018.09.045

286. J. Casado, Towards industrial implementation of Electro-Fenton and derived technologies for wastewater treatment: a review. J. Environ. Chem. Eng. **7**, 102823 (2019). https://doi.org/10.1016/j.jece.2018.102823

287. I. Salmeron, I. Oller, K.V. Plakas, S. Malato, Carbon-based cathodes degradation during electro-Fenton treatment at pilot scale: changes in H_2O_2 electrogeneration. Chemosphere **275**, 129962 (2021). https://doi.org/10.1016/j.chemosphere.2021.129962

288. Z. Ye, D.R.V. Guelfi, G. Alvarez, F. Alcaide, E. Brillas et al., Enhanced electrocatalytic production of H_2O_2 at Co-based air-diffusion cathodes for the photoelectro-Fenton treatment of bronopol. Appl. Catal. B **247**, 191–199 (2019). https://doi.org/10.1016/j.apcatb.2019.01.029